A Numerical Interpretation Model for the Dipole Flow and Reactive Tracer Test

by

Blythe Reiha

A thesis
presented to the University of Waterloo
in fulfillment of the
thesis requirement for the degree of
Master of Applied Science
in
Civil Engineering

Waterloo, Ontario, Canada, 2006

I hereby declare that I am the sole author of this thesis. This is a true copy of this thesis, including any required final revisions, as accepted by my examiners.

I understand that my thesis may be made electronically available to the public.

ABSTRACT

In order to protect public health and the natural environment, regulatory agencies such as the U.S. Environmental Protection Agency (USEPA) and the Ontario Ministry of the Environment (MOE) have developed a variety of clean-up programs to remediate contaminated sites. Before a remedial strategy can be implemented, physical, chemical and biological information of the site must be characterized so that an appropriate remedial approach can be selected. Problems exist with common characterization applications such as non-representative sample collection, time-consuming and costly testing, and loss of sample integrity due to transport. The success of the dipole flow test (DFT) and dipole flow tracer test (DFTT) indicate the potential for identifying a wide range of physical aquifer characteristics through *in situ* techniques; this has led to the development of the dipole flow reactive tracer test (DFRTT), which can be used to identify sorption and degradation characteristics in addition to those characteristics already identifiable by the DFT and DFTT. The DFRTT contains numerous advantages including the ability to inject a variety of reactive tracers using pulse or continuous injection, it can be used at multiple locations and depths across a site, and it is cost-effective.

The focus of this thesis was to develop and validate an efficient numerical framework for the reactive-transport component of the DFRTT interpretation model so that it could be used to simulate a variety of reactive tracers. The model will then be calibrated to match the resulting DFRTT field breakthrough curves (BTCs) so that certain aquifer property values can be obtained.

The comprehensive-reactive transport model (CRTM) was developed to solve the advective-dispersive-reactive equation (ADRE) using a streamline-oriented control volume (CV) mesh, to minimize the introduction of numerical dispersion (due to the dipole's rapidly converging and diverging flow field). In order to reduce computational effort, the ADRE was decoupled using operator-splitting techniques (OS) and the resulting partial differential equation for the transport component was solved using a finite volume approach, while the fourth-order form of Runge-Kutta was used to solve the resulting ordinary differential equation of the reactive component. Four OS techniques were implemented to decouple the ADRE; two of the techniques were iterative, while the other two were non-iterative. The use of iterative OS techniques enabled the introduction of a flux corrected transport (FCT) scheme (in addition to the commonly used

central differencing scheme (CDS) and upwind differencing scheme (UDS)), for solving the transport portion of the ADRE.

The CRTM was validated against a current "off-the-shelf" model, MODFLOW/MT3DMS. The resulting simulations indicated that the CRTM and MODFLOW/MT3DMS BTCs compared well for a conservative, decaying (first-order), and sorbing (linear sorption isotherm) tracer under specific conditions. However, MODFLOW/MT3DMS illustrated signs of failure when a large flow rate or a small longitudinal dispersivity coefficient was employed. It was concluded that MODFLOW/MT3DMS was unable to handle the rapidly converging and diverging dipole flow field, and that it was necessary to develop/utilize a dipole specific model for modelling the DFRTT application.

Analysis of the three advective schemes indicated that CDS was an inappropriate method for the dipole configuration used in the investigation (due its non-monotone solutions), and that the UDS, although unconditionally monotone, produced excessive numerical dispersion. The FCT scheme had the benefits of both CDS and UDS; however, it was computationally slower than the UDS due to its iterative nature.

Examination of the OS techniques indicated that in most cases there were no significant differences between any of the OS methods; however if a prominent sink term was utilized, the iterative techniques were deemed superior over the non-iterative techniques because of their ability to correct mass depletion. It was also determined that because of FCTs second-order accuracy, the OS techniques employing FCT had lower errors than those which did not.

The CRTM was used to design a DFRTT biodegradation experiment under Canadian Forces Base (CFB) Borden conditions. Dipole parameters were altered so that a dipole configuration could be recommended for field testing. It was determined that a decent zone of influence aquifer volume (~ 65 m^3) with a detectable BTC tail occuring between 2 and 3 days required a dipole length = 0.8 m, and a half-chamber length = 0.15 to 0.30 m. The oxidation of toluene by aerobic bacteria present within the Borden aquifer was also simulated. The purpose of these simulations was to obtain a detectable substrate BTC so that experimental parameters could be recommended for conducting a field experiment. To achieve a detectable substrate BTC the following recommendations were made: (i) sampling events should occur once every 1 to 2 hours (if possible) so that the changes in effluent concentration can be documented accurately; (ii) dipole parameters from Section 5.1 with a standard 2" well should be employed; (iii) a large

substrate concentration should be utilized (> 4.0 mg/L); (iv) a flow rate of $1x10^{-4}$ m^3/s should be used; and (v) an injection duration of 2 hours should be applied. As long as the field substrate BTC is measurable then Monod kinetics parameters can be estimated after a field and CRTM BTC comparison; this enables us to understand the aquifer's biodegradation potential (for remedial design purposes).

ACKNOWLEDGEMENTS

First and foremost I would like to thank Dr. Neil R. Thomson for accepting me into his research program. Neil has provided me with immeasurable challenges that I am absolutely grateful for. His dedication and relentless hard work is certainly an inspiration. Thank you Neil for all the support you have provided me during my graduate degree.

Endless thanks to my parents and family!

I would like to acknowledge the graduate students from the Water Resources group, whom provided a fun and light-hearted working atmosphere, specifically Quinn Crosina, Jeff DeLoyde, Laura Jones, and Erika Klyszejko. You all certainly made work very enjoyable.

Technical discussions with Laura Jones, Chris Hadlock and Nathan Kotey were pivotal in enabling me to finish my thesis. I am grateful for all of the technical help I received, and certainly couldn't have made it this far without any of you.

I am also grateful to Dr. Gordon Stubley for providing me with necessary technical information regarding flux corrected transport – a major part of my thesis.

Finally, I would like to acknowledge my fabulous husband Chris Hadlock. Your intelligence and witty humour has been essential to keeping me happy and sane. Every day has been fun and full of laughter, thank you. I look forward to our non-academic life together.

Funding for this research was provided by a Natural Sciences and Engineering Research Council (NSERC) of Canada Collaborative Research and Development (CRD) Grant (J.F. Barker, PI), a NSERC Discovery Grant (N.R. Thomson), a Ontario Graduate Scholarship in Science and Technology (OGSST) Scholarship, and the D.G. Mumford Graduate Scholarship.

TABLE OF CONTENTS

LIST OF TABLES

LIST OF FIGURES

CHAPTER 1 INTRODUCTION

During the last three decades there has been a growing concern over the use and disposal of toxic chemicals (petroleum hydrocarbons, solvents, metals, etc.) and their effect upon soil and groundwater quality. In order to protect public health and the natural environment, regulatory agencies such as the U.S. Environmental Protection Agency (USEPA) and the Ontario Ministry of the Environment (MOE), have developed a variety of clean-up programs to remediate contaminated sites. Currently, there exists a wide variety of unique clean-up technologies including, bioremediation, permeable reactive barriers, *in situ* chemical oxidation, soil excavation, and monitored natural attenuation (USEPA, 2006); however, the remedial options diminish significantly once cost, time constraints, and hydrogeologic conditions are considered.

When selecting a remedial strategy it is imperative that physical, chemical and biological information (e.g., hydraulic conductivity, porosity, ion exchange capacity, redox capacity, and microbiological identification) of the site be characterized so that an appropriate remedial approach can be selected (USEPA, 2006). Determining aquifer material characteristics has proven to be difficult due to the inherent simplifications that arise from using literature values, or from *ex situ* measurement techniques such as constant head tests, permeameter tests, microcosm studies, and oxidation-reduction measurements. For acceptable results, these tests would have to be performed multiple times using samples from varying locations and depths resulting in a costly and time-consuming approach. As well, these techniques sometimes result in simplifications and/or assumptions of the site conditions (due to insufficient or poor quality data), which may ultimately lead to uncertain risk assessment and costly remediation strategies (Nielsen *et al.*, 2006).

Over the last decade, newly developed *in situ* measurement techniques such as the push-pull test and the dipole flow test have significantly improved aquifer property estimation. The push-pull test originates from work done in the petroleum industry for determining residual oil saturations (Tomich *et al.*, 1973) and consists of an injection (reactive and non-reactive species), reaction and extraction phase. This test is used predominantly for identifying aquifer characteristics such as effective porosity (Hall *et al.*, 1991), and microbial processes (rates of aeorbic respiration, denitrification, and sulphate reduction) (Istok et al., 1997). The dipole flow test is similar to Burns' (1969) single-well test, except three inflatable packers are used within a borehole to isolate two chambers. These chambers are used to circulate groundwater within the subsurface, creating a dipole effect (Kabala, 1993). Horizontal and vertical hydraulic conductivities can be estimated using observed hydraulic pressure changes in each flow chamber in conjunction with a mathematical model. Although the dipole flow test is relatively new to the field of site characterization, it has been used successfully to identify heterogeneous hydraulic properties in highly permeable aquifers (Zlotnik *et al.*, 2001).

Recently it has been proposed to extend the dipole flow test to include the identification of sorption, microbial, and other characteristics by injecting reactive tracers into the subsurface and analyzing the resulting breakthrough curves (BTCs) (McKnight *et al.*, 2003); this new *in situ* technique has been called the dipole flow reactive tracer test (DFRTT). The purpose for developing this aquifer testing methodology is to create an additional site characterization tool to aid in the remedial design process by providing a simple, reliable and cost-effective technique. The physical DFRTT tool contains three inflatable packers (used to isolate two chambers) within a single borehole. A series of pumps, situated at the ground surface, inject water into the isolated

injection (source) chamber, while simultaneously extracting water from the extraction (sink) chamber, under a constant flow rate. Once the pressure within the injection and extraction chambers has stabilized (assumed to indicate the establishment of a steady-state dipole flow field), a suite of reactive and non-reactive tracers (e.g., sorbing and biodegrading tracers) are introduced to the injection solution. The reactive tracers can be added over a finite period (pulse mode), or for an extended period of time (continuous mode) depending on the aquifer characteristics of interest. Samples collected from the extraction chamber are analysed for the injected tracer concentrations and reaction product concentrations. Although we expect that BTCs produced by the DFRTT tool are indicative of certain subsurface conditions, they will not yield parametric values that are essential for making informed decisions regarding remedial applications without the use of a suitable interpretation model. To obtain these aquifer property values, the DFRTT BTCs must be used as part of a parameter-fitting or calibration exercise with an interpretation model (Figure 1.1).

This interpretation model must be capable of capturing the essence of the dipole flow field and have the ability to quickly and economically interpret the response of the aquifer to various reactive tracers. Unfortunately, a standard "off-the-shelf" model will not sufficiently meet these requirements due to the dipole's highly converging and diverging flow field; therefore, it is desirable that a model specific to the DFRTT application be developed.

1.1 THESIS OBJECTIVES

The objectives of this thesis are to:

1) develop and validate an efficient numerical framework for the reactive-transport component of a DFRTT interpretation model so that it can be used to accurately simulate a variety of reactive tracers;
2) improve the current aquifer property estimation capabilities so that rates of biodegradation can be determined;
3) examine the design and operational parameters for initial field testing of the DFRTT at Canadian Forces Base (CFB) Borden.

1.2 SCOPE OF THESIS

The overall goal of this thesis involves the development and improvement of a mathematical model that can be used to interpret breakthrough curves generated by the DFRTT. Background information regarding conventional site characterization techniques, as well as details on the dipole flow test (DFT), dipole flow tracer test (DFTT), and DFRTT are incorporated into Chapter 2. Chapter 3 provides details of the DFRTT model flow component and describes aspects of the developed comprehensive reactive transport component. DFRTT model validation and sensitivity is discussed in Chapter 4. Chapter 5 provides an analysis of a dipole design and operational parameters for field-testing conditions at CFB Borden. Finally, Chapter 6 presents major findings and outlines recommendations for future work.

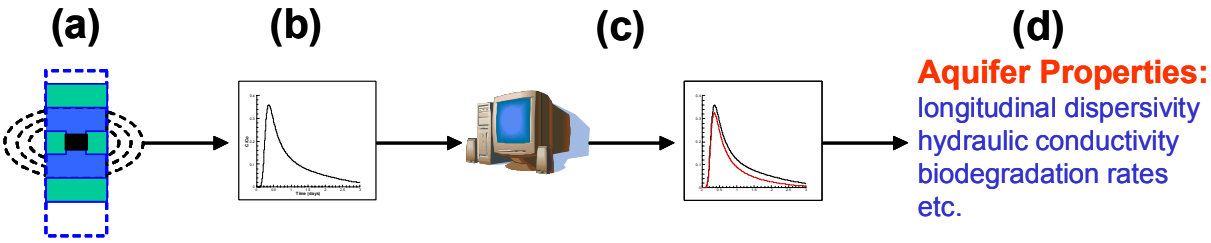

Figure 1.1: Illustrative example as to how the DFRTT can be used to identify aquifer properties; (a) test performed in the field is used to generate (b) a breakthrough curve which is used in conjunction with a mathematical model (c) and a parameter estimation scheme to yield (d) the aquifer properties of interest.

CHAPTER 2 BACKGROUND

Site characterization has been around since the early 1900's when geotechnical engineers began the construction of dams, buildings and roadways (Sara, 2003). Identification of geotechnical soil characteristics (soil moisture, soil density, elastic modulus, and internal resistance) aid in the design of a sound structure specific to the site-of-interest (Feld, 1965). In the 1970's, site characterization was expanded to include environmental assessment when several site investigations uncovered a multitude of environmental problems attributed to the poor handling, storage and disposal of hazardous products (Nielsen *et al.*, 2006). The purpose of environmental site characterization is to assess the extent of subsurface contamination, and to identify contaminant pathways, locations of possible receptors, and routes of exposure (Barcelona and Jaglowski, 1999; and Nielsen *et al.*, 2006). The various novel characterization tools that can be used to determine the required site information are divided into two general categores: *ex situ* techniques and *in situ* techniques; the information gained from these tools aid in the remedial design and planning processes.

2.1 EX SITU TECHNIQUES

Ex situ techniques refer to procedures that require the removal of aquifer material from the area-of-interest so that it may be transported and analyzed at another location (e.g., in a laboratory). Subsurface material can be removed from the site by borehole samples, grab samples or continuous tube samplers with a hollow-stem auger (Sevee, 2006). Once the material has been collected, the sample is run through various tests (permeameter tests, grain-size analysis, leaching/extraction tests, microcosm studies, and others) to identify physical, chemical and biological properties of the aquifer such as hydraulic conductivity, porosity, microbial identification, and biodegradation potential (Nielsen *et al.*, 2006; Sevee, 2006).

The shortcomings that exist with choosing *ex situ* approaches include 1) unidentified variability of the subsurface due to a non-representative sample collection; 2) time-consuming and costly testing; and 3) reduction of sample integrity during transport and experimental setup (Nielsen *et al.*, 2006; Thomson *et al.*, 2005). Potential problems could arise if the sampler fails to adhere to sampling protocols for soil and groundwater handling methods; this non-performance could greatly affect both the biological and chemical constituents of the sample.

2.2 IN SITU TECHNIQUES

In situ techniques refer to procedures that are performed in place. Hydraulic conductivity, transmissivity, storativity, and porosity are physical aquifer characteristics that can be identified using *in situ* procedures such as pump tests, flowmeter tests, slug tests, and multiple-well tests (ASTM, 1998). The main disadvantage to using these tests is that they induce predominantly horizontal flow patterns in which only horizontal hydraulic conductivity can be determined. Also, the majority of these tests are affected by well skin (Sutton *et al.*, 2000; Kabala, 1993). It should be noted that the importance of determining vertical hydraulic conductivity is significant as this yields the anisotropy ratio, which can be used to estimate the zone of influence for vertical wells in remediation applications (Sutton *et al.*, 2000; Zlotnik and Ledder, 1996).

Geophysical methods such as ground-penetrating radar and electromagnetics can be used to obtain geologic formation properties by non-intrusive methods which radiate high frequency electromagnetic waves into the subsurface (Benson, 2006). These methods are exceptional *in situ* techniques because they can determine hydrogeologic conditions such as fracture zones and clay

lenses, and they also have the ability to detect and map contaminant plumes by measuring changes in bulk soil conductivities caused by the contaminant (USEPA, 2000). The benefits of this approach are that it limits field investigation time and improves the accuracy of the overall investigation through continuous data collection (Benson, 2006). However, there are several limitations to the implementation of this technology: 1) time-consuming data manipulation; 2) complex data records require experienced analysts for interpretation (Hempen and Hatheway, 1992; USEPA, 2000; Sara, 2003); and 3) most methods produce qualitative results, making it difficult to estimate the parameter-of-interest.

Although there are *in situ* techniques that allow for the determination of physical and geologic characteristics (hydraulic conductivity, fracture zones, etc.) of the subsurface, there are currently few existing techniques that allow for the determination of biological and chemical properties without requiring sample analysis in a laboratory setting. Recently, Istok *et al.* (1999), and Schroth and Istok (2006) have used the push-pull test to quantify rates of microbial processes in petroleum hydrocarbon-contaminated aquifers (e.g., denitrification, sulphate reduction, and aerobic respiration); these findings are important since this information aids in predicting degradation rates of contaminants. However, there are currently no *in situ* approaches for determining redox capacity, or contaminant constituents; therefore lab analysis is still sometimes required.

The main advantage to choosing *in situ* over *ex situ* is the ability to perform *in situ* techniques over multiple locations and depths across the area-of-interest with minimal sample disturbance. Studies conducted using single-well tests, two-well tracer tests, partitioning interwell tracer tests

(PITT), re-circulatory flow tests, and more recently, push-pull tests, indicate that these practices may represent an opportunity to improve the identification of aquifer properties.

2.2.1 Two-Well Tracer Tests

The two-well tracer test has been used primarily to identify longitudinal dispersivity and effective porosity, but has also been used to identify aquifer sorption characteristics and biodegradation rates (Pickens and Griask, 1981; Güven *et al.*, 1986; Welty and Gelhar, 1994; Ptak and Schmid, 1996; Clement *et al.*, 1997; Huang *et al.*, 2003; and Tiedeman and Hsieh, 2004). This test requires a pulse or step input (of a tracer) into a recharge well; the BTC is monitored at a pumping well down-gradient from the recharge well. The resulting tracer BTC is used in conjunction with a suitable mathematical model to estimate effective porosity and longitudinal dispersivity. The advantages and disadvantages to using these tracer tests are outlined in Welty and Gelhar (1994).

Welty and Gelhar (1994) and Tiedeman and Hsieh (2004) concluded that to achieve a longitudinal dispersivity estimate from a forced-gradient test which corresponds to natural-gradient longitudinal dispersion, the aquifer sample area must be very large to ensure that the longitudinal dispersion estimate is not influenced by non-Fickian effects such as local heterogeneities. The unavoidable problem with increasing the sample area is that the test length increases and consequently, so does the cost. However, many applications such as the partitioning interwell tracer test and the dipole flow test are derivatives of the two-well tracer test because of its reported successes (Welty and Gelhar, 1994; and Tiedeman and Hsieh, 2004).

2.2.2 Partitioning Interwell Tracer Tests

The partitioning interwell tracer test (PITT) has been used to characterize the composition of non-aqueous phase liquid (NAPL) contamination, as well as its location and volume; this information is used for remediation operations (Jin *et al.*, 1995; Dwarakanath *et al.*, 1999; Istok *et al.*, 2002; and Imhoff and Pirestani, 2004). Similar to the two-well tracer test, the PITT requires injection and extraction wells that are strategically placed across the NAPL contaminated zone. Partitioning and non-partitioning tracers are added to the injection solution and monitored continuously in the extracted solution (Dwarakanath *et al.*, 1999). The non-partitioning tracers remain in the water phase while the partitioning tracers exchange between the water and NAPL phases depending on the partition coefficient. If the NAPL is at residual saturation, then the partitioning tracers are transported only in the water phase (Jin *et al.*, 1995) and the resulting tracer BTCs should show the partitioning tracers lagging behind the non-partitioning tracers. The differences between the partitioning tracer and the non-partitioning tracer BTCs are attributed to the amount of time the partitioning tracer spends in the NAPL phase and its partition coefficient. The quantity of NAPL saturation is dependent on the chromatographic separation of the tracers and can be appropriately characterized when the tracer breakthrough curves are used in conjunction with a suitable mathematical model and column experiments (Jin *et al.*, 1995; and Imhoff and Pirestani, 2004). It has been reported that a PITT is an effective technique for estimating the volume of NAPL and useful for evaluating the effectiveness of remediation applications (Jin *et al.*, 1995).

2.2.3 Push-Pull Tests

The push-pull test is a relatively new single-well *in situ* aquifer characterization technique that was originally developed by the oil industry. The push-pull test has been used to characterize

various properties including residual oil saturations (Tomich *et al.* 1973), effective porosity (Hall *et al.* 1991), rates of microbial processes (Istok *et al.* 1997; Struse *et al.* 2002; Schroth and Istok, 2006), and equilibrium sorption of surfactants (Istok *et al.* 1999). More recently, Mumford *et al.* (2004) successfully applied the push-pull test to determine the permanganate natural oxidant demand (NOD) of an aquifer; an estimate of the reduction capacity.

The test consists of three phases: the injection phase, the reaction phase, and the extraction phase. During the injection phase, a solution of reactive and non-reactive species is injected into the saturated zone. The reaction phase, which proceeds after the injection phase, allows the injected solution to react with the aquifer material. The allotted period of time for reaction is dependent upon the reactions of interest; for example, to assess microbial activity Istok *et al.* (1997) did not allow reaction time, while Tomich *et al.* (1973) allowed a reaction period of one to two weeks for the hydrolysis of ethyl acetate. When assessing NOD, a suitable reaction period should be allotted so that the reaction can occur fully without too much time for aquifer material contact (Mumford *et al.*, 2004). Finally, the extraction phase is the last phase of the push-pull test where the injected solution (and groundwater) is pumped from the well, sampled, and then analyzed; the data obtained are used to develop a BTC. Transport and sorption characteristics, as well as reaction kinetics of the injected species, can be determined once the BTC is used in conjunction with a suitable model (Istok, 1997; and Mumford *et al.*, 2004).

The study performed by Mumford *et al*. (2004) concluded that there are several advantages to using a push-pull test over current bench-scale testing methods for determining NOD; these benefits include 1) possible identification of NOD spatial variability in a homogeneous aquifer;

and 2) the utilization of an already existing monitoring well, making the push-pull test versatile and cost-effective. The major drawback to using the push-pull method, to assess NOD, is the need to monitor groundwater velocity direction and magnitude (before and during the test) since they are responsible for transporting the injected solution down-gradient of the injection point (called drifting); constant monitoring would be very time-consuming.

2.3 DIPOLE FLOW TEST

Kabala (1993) was the first to propose an extension to the vertical re-circulatory system using an approach similar to Burns' (1969) single-well test to estimate vertical permeability of bedrock. The design includes a cased well with two chambers separated by a packer (Kabala, 1993). Fluid is pumped at a constant rate from one chamber, while changes in pressure are observed in the second chamber. According to Kabala (1993), the limitation of the Burns test was the predominantly horizontal flow pattern. Kabala believes a test with a vertically dominated flow pattern could be used to estimate vertical hydraulic conductivity better than a test based on a horizontally dominated flow pattern.

Kabala's test setup is similar to Herrling's vertical circulation well application. Herrling and Buermann (1990), and Herrling and Stamm (1992) were the first to propose vertical circulatory flow for remediation purposes. The vertical circulation well consists of two screened chambers, separated by an impermeable casing. Once steady vertical flow is achieved, a pump located at the ground surface extracts water from one chamber and brings it to the surface where it is treated to remove contaminants. The treated water is then returned to the aquifer (at the same rate it was extracted) through the second chamber (Van Peursem, 1999; and Miller and Elmore,

2005). For Kabala' setup, a pump, situated between the two chambers, pumps water from the aquifer to one chamber (sink) at a constant rate. The water is then transferred to the other chamber (source), via tubing, where it is returned back to the aquifer; this circulation creates the dipole flow pattern (Figure 2.1). Drawdown measurements are used with an appropriate mathematical expression to estimate vertical and horizontal hydraulic conductivities as well as specific storativity (Kabala, 1993; and Sutton *et al.* 2000).

The mathematical model developed by Kabala (1993) to interpret hydraulic conductivity based on the observed pressure changes in the two chambers assumed (i) a fully penetrating well in a confined aquifer of infinite extent, (ii) no well bore storage, (iii) no skin effect, (iv) no well losses, (v) no storage in the confining layer, and (vi) a homogeneous radially symmetric anisotropic aquifer. With these assumptions he used the principle of superposition and the Hantush (1961) solution describing the drawdown in a partially penetrating observation well. The model's ability to emulate the physical system makes it quite useful and flexible. Although the model is quite beneficial, it contains certain limitations that may affect its representation of a DFT.

Although Kabala's DFT was at the forefront of a new *in situ* characterization techniques era, Zlotnik and Ledder (1996) expressed concern over Kabala's lack of drawdown analysis near the borehole and kinematic structure of the dipole flow field. In order to appease their concerns, Zlotnik and Ledder (1996) applied Stokes' stream function formulation to describe the kinematic structure of the dipole flow field. To determine the stream function, Zlotnik and Ledder (1996) used the steady-state groundwater flow equation subject to the following boundary conditions,

$$\lim_{r\to 0} \; r\frac{\partial s}{\partial r} = \frac{Q}{4\pi K_r \Delta} F(z) \tag{2.1}$$

$$F(z) = -1 \qquad |z - L| < \Delta \tag{2.2}$$

$$F(z) = 1 \qquad |z + L| < \Delta \tag{2.3}$$

$$F(z) = 0 \qquad otherwise \tag{2.4}$$

along with $s = 0$ as $r \to \infty$, $z \to \infty$, and $t = 0$, where K_r is radial hydraulic conductivity (L/T), Q is the flow rate (L^3/T), L is the half distance between the chamber centers (L), and Δ is the half chamber length (L). Therefore, Stokes' stream function for steady-state axisymmetric flow (assuming ambient flow is negligible) is given by (Bear, 1972),

$$\frac{\partial \psi}{\partial r} \equiv K_z r \frac{\partial s}{\partial z} = r V_{z,\infty}, \tag{2.5}$$

$$\frac{\partial \psi}{\partial z} \equiv -K_r r \frac{\partial s}{\partial r} = -r V_{r,\infty}, \text{ and} \tag{2.6}$$

$$\psi(0,0) = 0 \tag{2.7}$$

where K_z is vertical hydraulic conductivity (L/T), r and z are radial and vertical locations, respectively (L), s is the dipole-induced drawdown (L), $V_{z,\infty}$ and $V_{z,\infty}$ are steady-state local velocities (L/T), and the stream function, $\psi(0,0)$, is located in the centre of a circle ($r = 0$) in the $z = 0$ plane. Using the steady-state groundwater flow equation (subject to the given boundary conditions) and properties of the Hantush solution (1964), the following steady-state local velocity equations were determined (Zlotnik and Ledder, 1996),

$$V_{z,\infty} = \frac{K_z q}{2}\left[\frac{1}{R_{-+}} - \frac{1}{R_{--}} + \frac{1}{R_{+-}} - \frac{1}{R_{--}}\right] \tag{2.8}$$

$$V_{r,\infty} = \frac{K_r q}{2}\left[\frac{z_{--}}{R_{-+}} - \frac{z_{-+}}{R_{--}} + \frac{z_{++}}{R_{+-}} - \frac{z_{+-}}{R_{--}}\right] \tag{2.9}$$

$$R_{\pm\pm}^{\;2} = \left(\frac{r}{a}\right)^2 + (z \pm L \pm \Delta)^2 \tag{2.10}$$

$$z_{\pm\pm} = z \pm L \pm \Delta \tag{2.11}$$

where a^2 is the anisotropy ratio (K_r/K_z). By integrating Eq. (2.5) and (2.6), and applying the steady-state local velocity equations, an analytical expression for Stokes' stream function, as a function of (r, z), was determined; this function is applicable to dipole flow analysis in subsurface flow (Zlotnik and Ledder, 1996),

$$\psi(r,z) = \frac{Q}{8\pi\Delta}[4\Delta + R_{-+} - R_{--} + R_{+-} - R_{++}] \tag{2.12}$$

where Q is flow (m^3/s).

Using several variations of this model (applicable to different aquifer boundary conditions including infinite, semi-infinite confined, semi-infinite unconfined, finite confined and finite unconfined) they determined that the region of hydraulic influence for dipole flow is approximately *10aL* in the radial direction and *4L* in the vertical direction. The extent of this region is controlled by the distance between chamber centres and the chamber length. For example, assuming a sand and gravel aquifer with a horizontal hydraulic conductivity of 100 m/day, an anisotropy ratio of 1 and a packer length of 1.0 m, the horizontal extent of the dipole flow field is approximately $10aL \approx 10(1)(1.0) \approx 10$ m, and the vertical extent of the dipole flow field is approximately $4L \approx 4(1.0) \approx 4$ m. Zlotnik and Ledder (1996) also indicated that when using Stokes' stream function for estimating the region of influence, the dipole chamber length can be neglected; however, the chamber length is critical for determining flow in the vicinity of the dipole chambers. In fact, in their model development they ignored the well diameter and well skin, and assumed a symmetric dipole system within a homogeneous aquifer.

To validate the DFT approach, Zlotnik *et al.* (2001) conducted a comparison of hydraulic conductivity estimates from the DFT, at a field site in Germany, to a variety of *in situ* (pump tests) and *ex situ* test results (sieve analysis, and constant head tests). They determined that the DFT was successful in delineating heterogeneous hydraulic properties in highly permeable aquifers.

To improve the DFT versatility, Halihan and Zlotnik (2002) modified it to be asymmetric so that the injection and extraction chambers would be different lengths. The physical test setup is similar to the DFT, except only one packer is used to separate the lower from the upper chamber. The asymmetric DFT was tested at a field site in Wisconsin, USA (within a fractured rock aquifer) and the results were compared to double packer slug extraction (DPSE) tests. Both techniques yielded similar values of radial hydraulic conductivities suggesting that the asymmetric DFT can be used to delineate hydraulic properties in a fractured rock aquifer.

2.4 DIPOLE FLOW TRACER TEST

Sutton *et al.* (2000) developed and applied an extenstion to the DFT by combining it with a conservative tracer to create the dipole flow tracer test (DFTT). The DFTT works in a similar fashion to the DFT, except when a steady-state flow field has been established, a conservative or instantaneously sorbing tracer is released into the injection chamber and allowed to move through the dipole flow field. The tracer concentration is monitored in the extraction chamber and the resulting BTCs are used in conjunction with a suitable model to identify aquifer characteristics (dispersivity, and porosity). Although the DFTT performs similarly to the two-

well tracer test, it is also comparable to aspects of the push-pull test since it has the ability to identify aquifer processes such as sorption.

The dipole flow interpretation model developed by Sutton *et al.* (2000) uses the principal of superposition for two partially-penetrating wells (representing the injection and extraction chambers) in a confined aquifer, assuming no well skin. Using the steady-state solution for this dipole flow problem, radial and vertical components of groundwater velocity were determined and pathlines (streamlines) were calculated. For comparison purposes, the dipole flow model developed by Zlotnik and Ledder (1994) uses a Stokes' stream function expression to directly calculate pathlines in the dipole flow field. The transformed one-dimensional advection-dispersion equation for an impulse initial condition and zero concentration boundary conditions, developed by Gelhar and Collins (1971), was used along streamtubes to determine tracer transport.

The study performed by Sutton *et al.* (2000) suggest that the ratio of the front arrival time (t_f, the time in which concentration is 5% of the peak value) to the peak concentration arrival time (t_p, the time in which concentration is at its peak value) is affected by dispersivity and not the anisotropy ratio. However, the study results suggest that the anisotropy ratio is linearly related to the dimensionless time to peak for a given longitudinal dispersivity (α_L). Vertical hydraulic conductivity can be determined from the following steps i) estimate the ratio of longitudinal dispersivity to the characteristic length of the dipole system (l_c, the distance between the inner edges of the injection and extraction chambers) from t_f/t_p given by the BTC and type curves, ii) determine α_L given that l_c is known, iii) estimate the anisotropy ratio from the α_L and

dimensionless time to peak, iv) use the radial hydraulic conductivity versus chamber drawdown expression and the anisotropy ratio to estimate radial hydraulic conductivity, and v) calculate vertical hydraulic conductivity.

It should be noted that there are two main benefits that the DFTT has over the DFT. The first benefit has already been mentioned, the DFTTs ability to yield longitudinal dispersivity from the dimensionless peak concentration arrival time and the DFTT length. The second benefit is that the DFTT is able to detect skin effects, which are exhibited as extra peaks in the BTC. The identification of skin zones allow for a better estimate of hydrodynamic parameters without the bias of skin effects.

The collective work of Kabala (1993) and Sutton *et al.* (2000), as well as the push-pull test utility and ability, have inspired the development of a new characterization technique that combines the DFTT with a reactive tracer test to create the dipole flow reactive tracer test (DFRTT).

2.5 DIPOLE FLOW REACTIVE TRACER TEST

Similar in structure to the DFT, the DFRTT circulates water between an isolated injection (source) and extraction (sink) chamber within a single borehole under a constant flow rate. The dipole tool, which is placed in a test well (Figure 2.2), is characterized by the shoulder length L, which represents the distance between the middle of the central packer to the middle of either the extraction or injection chamber ($2L$ is the separation length or the distance between chamber centers); and 2Δ, which is the extraction or injection chamber length. Once the pressures within the injection and extraction chambers have stabilized (assumed to indicate the establishment of a

steady-state dipole flow field) a suite of conservative reactive tracers (e.g. sorbing and biodegrading tracers) are introduced into the injection solution. The reactive tracers can be added over a finite period (pulse mode, for sorption processes), or for an extended period of time (continuous mode, for biological processes) depending on the aquifer parameters of interest. Samples collected from the extraction chamber are analysed for the injected tracer and reaction product concentrations. These concentration BTCs are interpreted by a suitable mathematical model to estimate the required aquifer properties.

Due to its design, the DFRTT has the ability to estimate a wider range of aquifer characteristics than the DFTT, DFT, push-pull test, PITT, and two-well tracer test (Table 2.1). The benefits of using only the DFRTT as opposed to multiple site characterization tests include reduction in equipment, cost, and setup time. Figure 2.3 illustrates how the PITT and DFRTT are applied for source zone characterization, respectively. As demonstrated, from Table 2.1 and Figure 2.3, the DFRTT has the ability to characterize a wide range of NAPL and source zone properties, and can be easily moved from location to location, quickly and efficiently.

Currently there are no "off-the-shelf" models capable of interpreting BTCs produced by the DFRTT tool, in a timely fashion. If this dipole flow tool is to be applicable for real-world situations, a model that is computationally efficient, easy-to-use, robust, and easily expandable, should be used to aid in interpreting BTCs quickly. Unfortunately, current "off-the-shelf" models such as MODFLOW/MT3D (Zheng and Wang, 1998), and BIO3D (Molson, 1988), do not have the ability to handle the dipole's highly converging and diverging flow without difficultly.

Therefore, we envision a stand-alone model for the DFRTT; this model is discussed in Chapter 3.

Table 2.1: Summary of aquifer identification capabilities for site characterization techniques (adapted from McKnight *et al.*, 2003).

Test	Hydraulic/Transport Properties	Sorption/Ion Exchange Properties & Kinetics	Biodegradation Properties	NAPL Source Zone Properties
Two-Well Tests	Longitudinal Dispersivity Effective Porosity Dispersion Coefficient	Sorption Characteristics	Biodegradation Rates	
Push-Pull Tests	Effective Porosity	Equilibrium Sorption of Surfactants Permanganate Natural Oxidant Demand Oxidation Reaction Kinetics	Biodegradation Rates	
PITT				NAPL Volume Extent of Smear Zones NAPL Composition
DFT	Horizontal Hydraulic Conductivity Vertical Hydraulic Conductivity Storativity			
DFTT	Horizontal Hydraulic Conductivity Vertical Hydraulic Conductivity Storativity Longitudinal Dispersivity			
DFRTT	Horizontal Hydraulic Conductivity Vertical Hydraulic Conductivity Storativity Longitudinal Dispersivity	Cation Exchange Capacity (CEC) Anion Exchange Capacity (AEC) Exchange Selectivity Coefficients Sorption Characteristics Redox Capacity Reactive Surface Area	Biodegradation Rates and Half-Lives Bioavailable Oxidation Capacity Microbial Biomass Production	Sorption Characteristics Extent of Smear Zones Reactive Surface Area Biodegradation Rates

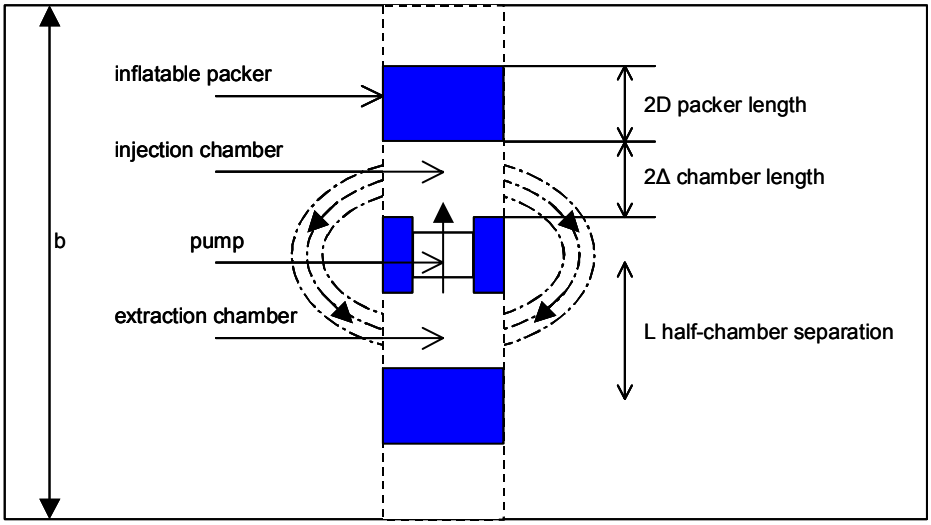

Figure 2.1: Schematic diagram of the dipole setup adapted from Kabala (1993).

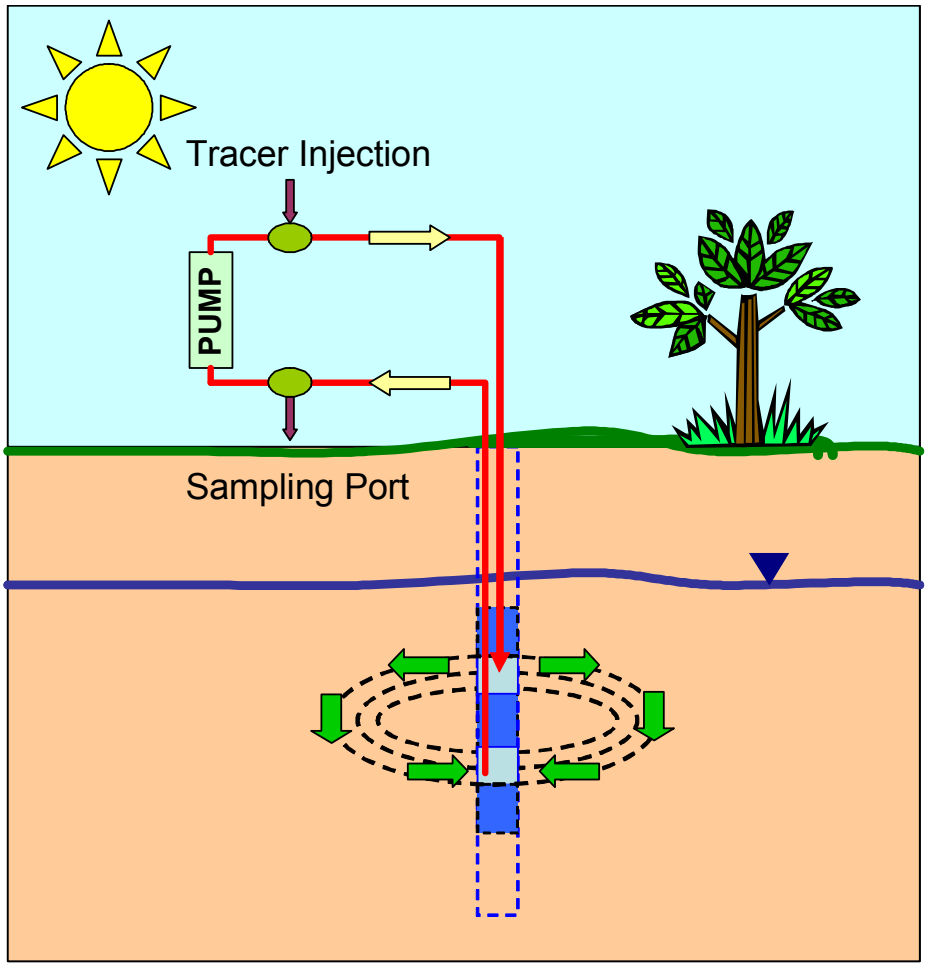

Figure 2.2: Illustrative example of DFRTT configuration.

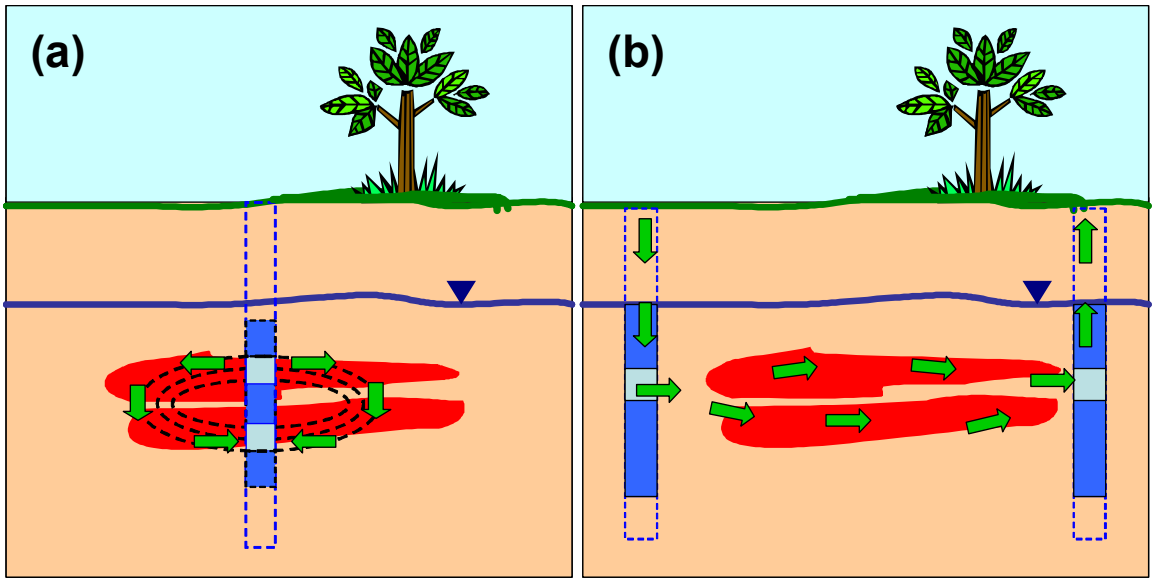

Figure 2.3: Schematic of (a) how the DFRTT can be used to estimate NAPL volume and (b) how the PITT is used.

CHAPTER 3 DFRTT MODEL

A robust DFRTT-specific model has been developed for interpreting breakthrough curves since existing models are incapable of performing dipole flow field calculations with computational efficiency (Thomson, 2003). This model is a mathematical tool that can be used to estimate key aquifer material parameters by matching model breakthrough curves to those obtained from the field. It is envisioned that this curve matching process will involve an automated calibration process, perhaps using a nonlinear parameter estimation package (e.g., PEST; Doherty, 2000), where key parameters are perturbed in order to match critical BTC metrics (center of mass, time to peak, peak concentration, etc.).

The DFRTT model was developed as a high-resolution 2D radially symmetric finite volume model consisting of two major components: a steady-state groundwater flow component, and a reactive transport component. The model was designed so that it could provide an accurate representation of key first-order processes, have the ability to conform to a variety of field configurations and site conditions, be able to handle a range of input parameters, and be extendable so that additional reactions and processes could be added with minimal coding. In order to minimize computational effort, two important assumptions were invoked: (1) that the ambient hydraulic gradient does not affect the dipole flow field, and (2) that aquifer properties (hydraulic, chemical and biological) are symmetric with respect to the testing well (Thomson, 2003).

The model framework was designed and developed by Thomson (2003). This thesis focuses on modifications and extensions to the initial version of the comprehensive reactive transport model (CRTM); however, for completeness, relevant details of the flow component and the simple

streamtube reactive transport models are described before the numerical details pertinent to the comprehensive reactive transport model are discussed.

3.1 FLOW COMPONENT

The backbone of the DFRTT model (developed by Thomson, 2003) is the flow field, which transports the various tracers from the injection to the extraction chamber. The flow component solves the radial saturated symmetric non-homogeneous isotropic groundwater flow equation, and accounts for skin and wellbore effects. It is also capable of modeling an asymmetric dipole system, an upper or lower confining layer (above or below the dipole tool), and a hydrogeologic setting with any number of horizontal layers defined by different hydraulic properties (hydraulic conductivity and porosity). In summary, the present version of this flow model allows for the specification of:

(i) a well skin with a specified thickness, hydraulic conductivity and porosity;
(ii) the location of upper and lower horizontal confining boundaries;
(iii) horizontal feature(s) with a thickness, hydraulic conductivity, and porosity; and
(iv) an asymmetric dipole system.

The primary flow field is obtained from the solution to the stream function equation, while the solution to the hydraulic head governing equation is used as a secondary flow field except when the wellbore model is applied. The stream function field is obtained by solving the axially symmetric non-homogeneous isotropic governing equation given by (Bear, 1972),

$$K_z \frac{\partial^2 \psi}{\partial z^2} + K_r \frac{\partial^2 \psi}{\partial r^2} - \frac{K_z}{K_r} \frac{\partial K_r}{\partial z} \frac{\partial \psi}{\partial z} - \frac{K_r}{r} \frac{\partial \psi}{\partial r} - \frac{K_r}{K_z} \frac{\partial K_z}{\partial r} \frac{\partial \psi}{\partial r} = 0 \qquad (3.1)$$

where K_z is hydraulic conductivity in the vertical direction (L/T), K_r is hydraulic conductivity in the radial direction, and ψ represents the stream function (-). The spatial domain for this system

is defined in cylindrical coordinates (r, z), with $r = 0$ the centre of the wellbore, $r = r_{max}$ the maximum radial extent of the spatial domain, $z = 0$ the midpoint of the symmetric dipole system, $z = z_{max}^{lower}$ the lower extent of the spatial domain, and $z = z_{max}^{upper}$ the upper extent of the spatial domain (Figure 3.1). The associated boundary conditions for Eq. (3.1) are given by,

$$\psi\left(r = r_{max}, z\right) = 0 \quad \textit{(no flow)} \tag{3.2}$$

$$\psi\left(r, z = z_{max}^{upper} \text{ and } z_{max}^{lower}\right) = 0 \quad \textit{(no flow)} \tag{3.3}$$

$$\psi\left(r = r_w, z \geq L^{upper} + \Delta^{upper} \text{ and } z \leq -L^{lower} - \Delta^{lower}\right) = 0 \quad \textit{(no flow)} \tag{3.4}$$

$$\psi\left(r = r_w, -L^{lower} + \Delta^{lower} \leq z \leq L^{upper} - \Delta^{upper}\right) = 1 \tag{3.5}$$

$$\psi\left(r = r_w, L^{upper} - \Delta^{upper} \leq z \leq L^{upper} + \Delta^{upper}\right) = \left(1 - \frac{z - L^{upper} + \Delta^{upper}}{2\Delta^{upper}}\right) \tag{3.6}$$

$$\psi\left(r = r_w, -L^{lower} - \Delta^{lower} \leq z \leq -L^{lower} + \Delta^{lower}\right) = \left(\frac{z + L^{lower} + \Delta^{lower}}{2\Delta^{lower}}\right) \tag{3.7}$$

where L^{upper} is the upper dipole length (distance between the central packer midpoint and injection chamber centre), L^{lower} is the lower dipole length (distance between the central packer midpoint and extraction chamber centre), Δ^{upper} is the half-chamber length of the upper chamber, and Δ^{lower} is the half-chamber length of the lower chamber. Eqs. (3.2), (3.3), and (3.4) force the external spatial domain to have a stream function value of zero, while Eq. (3.5) assigns a stream function value of unity coincident with the wellbore between the injection/extraction chambers. The boundary conditions expressed by Eqs. (3.6) and (3.7) represent a uniform well-face flux boundary condition. Subject to the given boundary conditions, Eq. (3.1) is solved numerically using an adaptive control volume (CV) approach where increased numerical resolution is used in the vicinity of the wellbore and injection/extraction chambers. Inter-CV hydraulic conductivities were calculated using a weighted harmonic mean; other solution details are described by Thomson (2003). The resulting asymmetric system of equations is solved by an iterative process

using an incomplete lower-upper (ILU) factorization reconditioner accelerated by either a general minimal residual (GMRES) scheme, or a bi-accelerated gradient stabilized (Bi-CGSTAB) scheme (Thomson, 2003).

The hydraulic head field is obtained on the same CV grid as the stream function field by solving the axially symmetric flow equation given by,

$$\frac{\partial}{\partial z}\left(K_z \frac{\partial h}{\partial z}\right)+\frac{1}{r}\frac{\partial}{\partial r}\left(rK_r \frac{\partial h}{\partial r}\right)=0 \tag{3.8}$$

The associated boundary conditions for Eq. (3.8) are given by (Figure 3.1),

$$\frac{\partial h}{\partial z}=0 \ \left(r, z=z_{max}^{upper} \text{ and } z_{maz}^{lower}\right) \tag{3.9}$$

$$\frac{\partial h}{\partial r}=0 \ \left(r=r_w, z \geq L^{upper}+\Delta^{upper} \text{ and } z \leq -L^{lower}-\Delta^{lower} \text{ and } -L^{lower}+\Delta^{lower} \leq z \leq L^{upper}-\Delta^{upper}\right) \tag{3.10}$$

$$\frac{\partial h}{\partial r}=0 \ or \ h=\hat{h} \ \left(r=r_{max}, z\right) \tag{3.11}$$

$$q=\hat{q} \ \left(r=r_w, L^{upper}-\Delta^{upper} \leq z \leq L^{upper}+\Delta^{upper} \text{ and } -L^{lower}-\Delta^{lower} \leq z \leq -L^{lower}+\Delta^{lower}\right) \tag{3.12}$$

where h is hydraulic head (L), $\hat{h}$ is a specified hydraulic head (L), and $\hat{q}$ is a specified flux (L/T). Similar to the numerical solution used for the stream function formulation, the resulting asymmetric system of equations is solved by an iterative process using an ILU factorization reconditioner accelerated by either a GMRES scheme, or a Bi-CGSTAB scheme. This hydraulic head formulation allows for either a no-flow boundary condition or a specified head boundary condition on the $r = r_{max}$ boundary (Eq. (3.11)). The no-flow boundary condition is consistent

with the stream function formulation while the specified head boundary condition allows fluid to enter or exit the spatial domain in response to the prescribed dipole flow conditions, system geometry, and hydraulic properties. The flux boundary condition along the injection and extraction chambers is handled as either a uniform or integrated well-face boundary condition (Ruud and Kabala, 1997). For the uniform well-face flux boundary condition, Eq. (3.12), the specified flux for each CV_i along the injection/extraction chamber is assigned a transmissivity weighted fraction of the total flow Q_w as expressed by,

$$q_i = \pm\left(\frac{K_{ri}\Delta z_i}{\sum K_{rj}\Delta z_j}\right)\left(\frac{Q_w}{2\pi r_w}\right)\left(\frac{1}{\Delta z_i}\right) \tag{3.13}$$

where Q_w is total flow (L^3/T), K_r is radial hydraulic conductivity for the CV associated with the injection/extraction chamber, and Δz is the length of the CV in the z-direction. For the integrated well-face condition a non-iterative algorithm is used that consists of a series of one-dimensional finite line elements superimposed along the chamber length (Sudicky *et al.*, 1995; Ruud and Kabala, 1997). A standard one-dimensional finite element formulation was used to generate a typical element matrix equation given by,

$$\frac{A_w K_w}{2\pi r_w L_e}\begin{bmatrix} +1 & -1 \\ -1 & +1 \end{bmatrix}\begin{Bmatrix} h_i \\ h_{i+1} \end{Bmatrix} = \begin{Bmatrix} q_i \\ q_{i+1} \end{Bmatrix} \tag{3.14}$$

$$K_w = \frac{r_w^{\,2}\rho g}{8\mu} \tag{3.15}$$

where h is hydraulic head (L), K_w is the hydraulic conductivity of the well (L/T), i represents the *ith* node along the chamber length, ρ is fluid density (M/L^3), g is gravity (L/T^2), μ is viscosity (M/LT), r_w is the radius of the well (L), A_w is the cross-sectional area of the well (L^2), and L_e is the element length given by the distance between respective CV centroids. After element assembly, the resultant contribution of flow at the top node is,

$$Q_1 = \frac{Q_w}{2\pi r_w} - \frac{K_{r_1}\Delta z_1}{\Delta r_1 / 2}\left(h_i - h_{i^+}\right) \tag{3.16}$$

and for the remaining nodes is,

$$Q_i = -\frac{K_{r_i}\Delta z_i}{\Delta r_i / 2}\left(h_i - h_{i^+}\right) \tag{3.17}$$

where Q is the flow rate at each node (L^3/T), K_{ri} is radial hydraulic conductivity (L/T), Δr is the CV dimension in the r-direction, and, i^+ is the CV centroid associated with the *ith* node. The resulting well-face fluxes from the hydraulic head solution are used to allocate stream function values along the injection and extraction chambers and the resulting stream function field is then determined. For the stream function and hydraulic head flow solutions, the wellbore skin is incorporated by assigning either a positive or negative skin along a user specified distance away from the wellbore.

3.2 STREAMTUBE REACTIVE TRANSPORT MODELS

Two streamtube transport models are available for simplistic simulations where mass transfer between streamtubes (e.g., transverse dispersion/diffusion) is insignificant, and reactions are limited to either linear instantaneous sorption or first-order decay. For situations where advection dominates the transport process, a predictor-corrector particle tracking algorithm is used to generate a travel time distribution from the injection to extraction chambers for selected streamtubes and the resulting BTC can be developed by integrating the contributions of the individual streamtubes at the extraction chamber using,

$$\mathrm{C(t)} = \int_{t=0}^{t=t_{max}} \int_{\psi=0}^{\psi=\psi_{max}} C_s e^{-\lambda t_a(\psi)} \left\{U\left[Rt_a(\psi) - t\right] - U\left[Rt_a(\psi) + t_s - t\right]\right\} d\Psi dt \tag{3.18}$$

where C_s is the source concentration (M/L^3), $t_a(\psi)$ is the travel time along streamtube ψ (T), t_s is the duration of the source slug (T), λ is the first-order reaction rate coefficient (1/T), U is the unit step function and R is the retardation factor defined by $R = (1+\rho_b k_d/\theta)$, ρ_b is bulk density (M/L^3), k_d represents the distribution coefficient (L^3/M) and θ is porosity. For other situations where longitudinal dispersion is important, a modified expression from the work by Gelhar and Collins (1971) is employed as given by,

$$\frac{\partial C}{\partial w} = \alpha_L \frac{\partial^2 C}{\partial \eta^2}, \tag{3.19}$$

$$\eta = x(s) - t, \tag{3.20}$$

$$x(s) = \int_{s_o}^{s} \frac{1}{u(s')} ds', \text{ and} \tag{3.21}$$

$$w(t) = \int_{s_o}^{s} \frac{u(s') + \frac{D_m}{\alpha_L}}{u^3(s')} ds' \tag{3.22}$$

provided that,

$$\left(\frac{\alpha_L}{L_o}\right)^{1/2} << 1 \tag{3.23}$$

where $u(s)$ is velocity along the streamtube (L/T), s is length along the streamtube (L), $x(s)$ is travel time along the streamtube from s_o to s (T), w is a transformation integral, D_m is the effective molecular diffusion coefficient (L^2/T), α_L is longitudinal dispersivity (L), t is time (T), and L_o is a length scale characteristic of the flow field (L) and represents the total streamtube path length for this application. The analytical solution to Eq. (3.19) (for a single streamtube), subject to the following boundary and initial conditions,

$$C = C_o \qquad \text{for } s < s_o \qquad \text{at } t = 0 \tag{3.24}$$

$C = 0$ for $s > s_o$ at $t = 0$ (3.25)

$C \to C_o$ as $s \to -\infty$ for $t > 0$ (3.26)

$C \to 0$ as $s \to \infty$ for $t > 0$ (3.27)

is given by (Gelhar and Collins, 1971),

$$C(s,t) = \frac{1}{2} C_o \left\{ erfc\left(\frac{x(s)R - t}{\sqrt{4\alpha_L R w\left(\frac{t}{R}\right)}} \right) - erfc\left(\frac{x(s)R - (t - t_s)}{\sqrt{4\alpha_L R w\left(\frac{t}{R} - \frac{t_s}{R}\right)}} \right) \right\} \quad (3.28)$$

where t_s is the duration of the source slug (T). The limitation to using Eq. (3.19) is that the condition expressed by Eq. (3.23) must be satisfied; this condition can be satisfied for low dispersion systems or those with a sufficiently long path length. Note that this solution does not account for first-order decay.

3.3 COMPREHENSIVE REACTIVE TRANSPORT MODEL

It is envisioned that in most situations, where a DFRTT will be used to characterize aquifer properties, a comprehensive reactive transport component (developed by the author of this thesis, B. Reiha) that provides a solution to the advective-dispersive-reactive transport governing equation (ADRE) will be required for the interpretation of the observed BTCs. The ADRE in cylindrical coordinates is given by (Istok, 1989),

$$\frac{\partial \theta C}{\partial t} = \frac{1}{r}\frac{\partial}{\partial r}\left(\theta D_{rr} r \frac{\partial C}{\partial r} \right) + \frac{\partial}{\partial z}\left(\theta D_{zz} \frac{\partial C}{\partial z} \right) + \frac{1}{r}\frac{\partial}{\partial r}\left(\theta D_{rz} \frac{\partial C}{\partial z} \right) + \frac{\partial}{\partial z}\left(\theta D_{zr} r \frac{\partial C}{\partial r} \right)$$

$$- \frac{1}{r}\frac{\partial}{\partial r}(r q_r C) - \frac{\partial}{\partial z}(q_z C) \pm \gamma \quad (3.29)$$

where C is concentration (M/L^3), θ is porosity, γ represents source-sink term(s) appropriate for the tracer under consideration and the chosen mathematical representation, q_r and q_z represent Darcy flux or velocity in the r and z directions, respectively (L^2/T), and D_{rr}, D_{zz}, D_{rz}, and D_{zr} are dispersion coefficients (L^2/T). In general, Eq. (3.29) is subject to the initial condition,

$$C(r,z,0) = 0 \tag{3.30}$$

and the following boundary conditions:

i) along the injection chamber a Type 1 or 3 boundary condition may be employed,

$$C(r,z,t) = \hat{C}(r,z,t) \qquad \text{Dirichlet (Type 1)} \tag{3.31}$$

$$\hat{qC} = q_r C - \theta D_{rr} \frac{\partial C}{\partial r} \qquad \text{Robin (Type 3)} \tag{3.32}$$

where $\hat{C}$ is a prescribed concentration (M/L^3), and $\hat{qC}$ represents a specified mass flux (M/L/T);

ii) along the extraction chamber a free-exit boundary condition may be employed (e.g., Frind, 1988); and

iii) along the remaining wellbore and external no-flow boundaries a Type 2 boundary condition is employed.

It is difficult to directly solve Eq. (3.29) in cylindrical coordinates without producing numerical dispersion from the rapidly diverging and converging flow field such as that present in a dipole flow field (Cirpka *et al.*, 1999a). In order to minimize the production of numerical dispersion, Eq. (3.29) was solved using a streamline-oriented CV mesh (SOM) based on streamtubes generated from the flow component (Figure 3.2). Each CV is comprised of four sides and the compass method is used to index the adjacent computational nodes (open circles) and integration points (solid circles). As a result of the SOM construction, advection and longitudinal dispersion

occurs across the north and south faces of the CV, transverse dispersion occurs across the east and west faces, and diffusion occurs across all faces. The use of the SOM allows for an effective computational solution to be employed for reactions with solid-phase species, and for the aqueous transport of the reactive tracers and mobile reaction products (Cirpka *et al.*, 1999a; Crane and Blunt, 2000).

3.3.1 Reactions and Potential Tracers

To identify appropriate model parameters and rate coefficients that capture the processes associated with biodegradation, sorption, ion exchange, and oxidation/reduction capacity, the DFRTT model has been designed to include flexibility for a range of non-reactive and reactive tracers. Examples of these tracers, along with the processes-of-interest, as well as representative mathematical relationships, are listed in Table 3.1.

3.3.1.1 Sorption

The sorption process, encompassing adsorption, and chemisorption can be described by using one of two equilibrium sorption models or a non-equilibrium sorption model depending on the rate of change in concentration (due to sorption) and the flow rate (Fetter, 1993) . The two equilibrium sorption models are described by,

$$\gamma_{sorb} = \rho_b \frac{\partial C_s}{\partial t} = \rho_b \frac{\partial \left(k_d C_w^{\ N} \right)}{\partial t} \tag{3.33}$$

where ρ_b is bulk density (M/L^3), C_s is mass of the solute sorbed per dry unit weight of solid (M/M), and k_d is the distribution coefficient (units are dependent on N). If N is unity then Eq. (3.33) represents a linear sorption isotherm, otherwise it corresponds to a Freundlich isotherm. The Freundlich isotherm is used for varying applications in the wastewater and hydrogeology

fields when the C_s vs. C_w relationship is non-linear. The Freundlich isotherm has been used to describe sorption of various compounds to soil, such as pesticides (Van Benum *et al.*, 2006), cadmium (Moradi *et al.*, 2005), and arsenate (Zhang and Selim, 2005). The problem with using either the linear or Freundlich equilibrium sorption models is the limitless amount of sorption that can occur. Also, the assumption of local sorption equilibrium may be inappropriate for some situations (Ball and Roberts, 1991; Rügner *et al.*, 1999; and Kleineidam *et al.*, 2004) and therefore, a non-equilibrium sorption model has also been included into the DFRTT model.

When the sorptive process is slow and the solute is not in equilibrium with the solid phase, then the process can be described by a non-equilibrium sorption model. The simplest form of non-equilibrium sorption (when the kinetic rate reaction is controlled by diffusion) is given by,

$$\gamma_{sorb} = \rho_b \frac{\partial C_s}{\partial t} = \rho_b \alpha \left(k_d C_w - C_s \right) \tag{3.34}$$

where α is a first-order rate coefficient (1/T), and C_s is mass of the solute sorbed per dry unit weight of solid (M/M). Eq. (3.34) is characteristically a reversible linear kinetic model limited by a first-order diffusion process. There have been reported successes of sorption prediction using the rate model expressed in Eq. (3.34) and other models that are of similar form; however, most of these successes have occurred in a laboratory setting with low pore water velocities (Nielsen *et al.*, 1986). It is believed that there are perhaps better rate models, such as the two-site model, which has the adsorption term consisting of two-components (equilibrium adsorption and first-order kinetics) (Nielsen *et al.*, 1986); however, for simplicity, only Eq. (3.34) was employed to represent non-equilibrium sorption in the DFRTT model at this time.

3.3.1.2 Decaying Tracer

To estimate degradation rates of an aqueous species, the DFRTT model includes a simple decay mass action law given by,

$$\gamma_{decay} = \frac{\partial \theta C_w}{\partial t} = -k\theta C_w^N \tag{3.35}$$

where N represents the reaction order, k is the decay coefficient (units are dependent on the reaction order), and θ represents porosity. Processes which may lead to contaminant degradation may include hydrolysis, or reactions with an electron acceptor or donor resulting in biodegradation (Martian *et al.*, 2003). First-order degradation rates (e.g., denitrification and aerobic respiration) have been successfully determined through the push-pull test by using tracer breakthrough curve data (Istok *et al.*, 1997; Haggerty *et al.*, 1998; Kim *et al.*, 2005; and Pitterle *et al.*, 2003).

3.3.1.3 Biodegradation

According to Kesavan (2005), Monod kinetics have been "widely used in wastewater treatment, bioremediation and in various other environmental applications involving growth of microorganisms." Bioremediation is preferable to other conventional remediation techniques (pump-and-treat) when a contaminated site contains unwanted organic products (petroleum or chlorinated solvents) because many of these contaminants are susceptible to degradation through biological or geochemical conditions in the groundwater (Schirmer *et al.*, 1999). This remediative process has the potential to be more cost-effective when compared to other treatment approaches. In order to degrade an organic contaminant biologically, the contaminant must act as a substrate that is susceptible to microbial degradation. According to MacQuarrie *et al.* (1989), to degrade an organic substrate a microbe must, "mediate an oxygen-reduction reaction that

requires an electron acceptor." The electron acceptor could be oxygen, nitrate, or sulphate, depending on whether the conditions are aerobic or anoxic. Once the microbes have consumed portions of the substrate, their population should increase, thereby resulting in further substrate consumption (MacQuarrie *et al.*, 1989). Detailed overviews of existing and recent advances in biological transport models are given in Baveye and Valocchi (1989). As outlined by Murphy and Ginn (2000), transport and biodegradation phenomena for modelling growth and decay processes in hydrogeologic applications have been incorporated into numerous models through varying forms of Monod-type equations.

In order to estimate microbial processes beyond a simple degradation rate coefficient (e.g., rates of aerobic respiration and denitrification), a biodegradation reaction component in the DFRTT model was developed so that Monod-kinetics could be used to investigate degradation of a substrate (e.g., a petroleum hydrocarbon) due to microbes, electron acceptors (O_2, NO_3^-) and electron donors (methanol/acetate). The Monod equations implemented are (Borden and Bedient, 1986; and MacQuarrie *et al.* 1990),

$$\gamma_{S\beta} = \frac{d\theta S_\beta}{dt} = -k_{max\beta} M_t \theta \frac{S_\beta}{S_\beta + K_{S\beta}} \frac{A}{A + K_A}, \tag{3.36}$$

$$\gamma_A = \frac{d\theta A}{dt} = -k_{max\beta} M_t \theta X_\beta \frac{S_\beta}{S_\beta + K_{S\beta}} \frac{A}{A + K_A}, \text{ and} \tag{3.37}$$

$$\frac{dM}{dt} = k_{max\beta} M_s Y_\beta \frac{S_\beta}{S_\beta + K_{S\beta}} \frac{A}{A + K_A} - bM \tag{3.38}$$

where S_β is concentration of the substrate β (M/L^3), θ is porosity, $k_{max\beta}$ is the maximum utilization rate of the substrate (T^{-1}), M_t is the total active biomass concentration (M/L^3), $K_{S\beta}$ is the half-utilization constant of the substrate (M/L^3), A is the electron acceptor concentration

(M/L^3), K_A is the electron acceptor half-utilization constant (M/L^3), X_β is the mass ratio of the electron acceptor (oxygen, nitrate or sulphate) to substrate consumed, Y_β is microbial yield per unit substrate consumed, M_s is the microbial mass in solution (M/L^3) and b is the first-order decay rate coefficient of the microbial population (T^{-1}). The microbial mass in solution is determined by,

$$M_s = \frac{M_t}{R_m} \tag{3.39}$$

where R_m is the retardation factor of the microbial species. The DFRTT treats the substrate and electron acceptor as mobile species, while the microbes are treated as an immobile species. The Monod kinetics portion of the model has the flexibility to allow multiple substrates to be incorporated into the model, however, at this time only one substrate has been implemented.

3.3.1.4 General: Aqueous – Solid Interaction

To handle general reactions that may involve the interaction between a mobile and an immobile species, a general mass action law was developed to allow for the injection of an aqueous species to interact with an already present solid species (in the subsurface). The mobile species undergoes both transport and reaction, while the immobile species only undergoes reaction; the general mass action law is given by,

$$\gamma_{ij} = \frac{\partial \theta C_i}{\partial t} = -k_i \theta C_i^{\alpha} C_j^{\beta} \qquad \text{mobile phase} \tag{3.40}$$

$$\rho_b \frac{\partial C_j}{\partial t} = -k_j \rho_b C_i^{\alpha} C_j^{\beta} \qquad \text{immobile phase} \tag{3.41}$$

where k_i and k_j represent the reaction rate coefficients for the mobile and immobile species, respectively (units are dependant on the reaction order), C_i is concentration of the injected

(mobile) species (M/L^3), C_j is concentration of the immobile species already present within the subsurface (M/M), ρ_b is bulk density (M/L^3), and α and β represent the reaction order of the mobile and immobile species, respectively. An example of this application may involve the injection of a permanganate solution ("the mobile species") to interact with a sorbed contaminant ("the solid species").

3.4 NUMERICAL FORMULATION

3.4.1 Operator-Splitting

According to Steefel and MacQuarrie (1996), the computational effort required to solve the ADRE is dependant upon the numerical approach and how the reaction and transport terms are coupled. Historically, solving the governing equations using a fully implicit one-step approach has been successful (Oran and Boris, 1987); however, research has demonstrated that the one-step approach is memory intensive and requires excessive computational effort (Yeh and Tripathi, 1989).

A widely accepted standard of practice for numerically solving advection-dispersion-reaction problems, without using the one-step approach, is to apply operator-splitting (OS) techniques that require decoupling of the ADRE (Valocchi and Malmstead, 1992). Choosing OS over the conventional one-step procedure allows different two-step methods to be used to solve a given problem (Barry *et al.*, 1996; Carrayrou *et al.*, 2004). Although employing OS techniques reduces computational effort (Steefel and MacQuarrie, 1996), it does induce some operator-splitting errors (Herzer and Kinzelbach, 1989; Barry *et al.*, 1996; and Carrayrou *et al.*, 2004). The typical approach to OS is to solve the resulting partial differential equation (PDE) for the transport component using a finite volume or finite difference method, and to utilize a numerical method

approach such as Runge-Kutta or Euler's method, to solve the resulting ordinary differential equation (ODE) for the reactive component (Valocchi and Malmstead, 1992).

Essentially, the various two-step methods can be divided into two categories: non-iterative and iterative techniques. The non-iterative approaches include the standard sequential non-iterative (SNI) and Strang-splitting (SS) methods, while the iterative approaches include the sequential iterative (SI) and the symmetric sequential iterative (SSI) methods. In general, these methods reduce the governing PDE given by Eq. (3.29) to a spatial transport (advection and dispersion) operator, and a reaction operator expressed as,

$$\frac{\partial C}{\partial t} = \mathcal{L}_{\mathcal{T}}(C) + \mathcal{L}_{\mathcal{R}}(C) \tag{3.42}$$

where $\mathcal{L}_{\mathcal{T}}(C)$ is the transport operator, and $\mathcal{L}_{\mathcal{R}}(C)$ is the reactive operator.

3.4.1.1 Sequential Non-Iterative Scheme

First proposed by Grove and Wood (1979) and Herzer and Kinzelbach (1989), the SNI scheme includes a single time step computational sequence of one transport step followed by one reaction step. Although the SNI scheme is relatively simple to implement, the major disadvantage to using it is the *O(Δt)* error that it produces when decoupling the transport and reactive terms (Herzer and Kinzelbach, 1989; and Carrayrou *et al.*, 2004). For a given time step, the first phase of the SNI scheme requires the ADE to be solved for each species *i*,

$$\frac{\boldsymbol{C}_i^{n+1} - \boldsymbol{C}_{\boldsymbol{SNI}_i}^{n}}{\Delta t} = \mathcal{L}_{\mathcal{T}}(\boldsymbol{C}_i) \tag{3.43}$$

where $\boldsymbol{C}_{i_i}^{n+1}$ is the concentration vector for species *i* at the new time step (*n+1*) (M/L^3), $\boldsymbol{C}_{\boldsymbol{SNI}_i}^{n}$ is the reactive concentration vector for species *i* produced at the previous time step (M/L^3), $\boldsymbol{C_i}$ is a

concentration vector for species *i* and is dependent on the time discretization scheme, and *n* represents the time step. The second phase of the SNI scheme involves the solution of the reaction component using,

$$\frac{\boldsymbol{C}_{SNI_i}^{n+1} - \boldsymbol{C}_i^{n+1}}{\Delta t} = \mathcal{L}_{\mathcal{R}}\left(\boldsymbol{C}_1, \boldsymbol{C}_2, ..., \boldsymbol{C}_i, ..., \boldsymbol{C}_{NC}\right) \tag{3.44}$$

where $\boldsymbol{C}_{SNI_i}^{n+1}$ is the concentration vector for species *i* after reactive transport has taken place (M/L^3), and *NC* is the number of reactive species. Once $\boldsymbol{C}_{SNI_i}^{n+1}$ has been determined from Eq. (3.44), the calculations are complete for the given time step.

3.4.1.2 Strang-Splitting Scheme

The SS scheme, also known as the alternating two-step method, was first proposed by Strang (1968) and since has been widely used (Kaluarachchi and Morshed, 1995; Hundsdorfer and Verwer, 1995; and Zysset *et al.*, 1994). The SS scheme is similar in principle to the SNI scheme except its computational sequence only induces a $O(\Delta t^2)$ error (Kaluarachchi and Morshed, 1995). The computational sequence of the SS scheme for a single time step is transport over $\Delta t/2$, followed by reaction over Δt, accompanied by another transport over $\Delta t/2$ (Barry *et al.*, 1996). Specifically, the ADE is solved for each species *i* over the first half-time step as denoted by,

$$\frac{\boldsymbol{C}_i^{n+1/2} - \boldsymbol{C}_{SS_i}^{n}}{\Delta t/2} = \mathcal{L}_{\mathcal{T}}\left(\boldsymbol{C}_i\right) \tag{3.45}$$

where $\boldsymbol{C}_{SS_i}^{n}$ is the concentration vector for species *i* produced by the SS scheme at the previous time step (M/L^3) and $\boldsymbol{C_i}$ is the concentration vector for species *i* and is dependent on the time discretization scheme. Next, the reactive operator is solved over the full time step using,

$$\frac{\boldsymbol{C}_i^{n+1} - \boldsymbol{C}_i^{n+1/2}}{\Delta t} = \mathcal{L}_{\mathcal{R}}\left(\boldsymbol{C}_1, \boldsymbol{C}_2, ..., \boldsymbol{C}_i, ..., \boldsymbol{C}_{NC}\right) \tag{3.46}$$

where $\boldsymbol{C}_i^{n+1}$ is the concentration vector for species *i* after reactive transport has taken place (M/L^3). Finally, the ADE is solved for each species *i* over the second half-time step as denoted by,

$$\frac{\boldsymbol{C}_{SS_i}^{n+1} - \boldsymbol{C}_i^{n+1}}{\Delta t/2} = \mathcal{L}_T\left(\boldsymbol{C}_i\right) \tag{3.47}$$

where $\boldsymbol{C}_{SS_i}^{n+1}$ is the concentration vector for species *i* at the end of the full time step (M/L^3).

3.4.1.3 Sequential Iterative Scheme

The SI scheme has been used successfully by Herzer and Kinzelbach (1989), Yeh and Tripathi (1991), and Hundsdorfer and Verwer (1995). According to Herzer and Kinzelbach (1989), the decoupling error produced from using the non-iterative two-step approach can be minimized by including iterations within each time step. To minimize the operating splitting errors further, this iterative approach introduces a reactive source-sink vector ($\boldsymbol{R_i}$) to represent the reactive operator within the solution of the ADE that is updated at each iteration after the reactive operator has been solved. For a given time step, iterations are executed on the transport and reactive components until convergence has been achieved. The first phase of the SI scheme involves the solution of the ADE for each species *i* with the additional reactive source-sink vector as expressed by,

$$\frac{\boldsymbol{C}_i^{n+1,m+1} - \boldsymbol{C}_{SI_i}^{n}}{\Delta t} = \mathcal{L}_T\left(\boldsymbol{C}_i\right) - \boldsymbol{R}_i^{m} \tag{3.48}$$

where $\boldsymbol{C}_i^{n+1,m+1}$ is the concentration vector for species *i* at the current iteration and time step (M/L^3), $\boldsymbol{C}_{SI_i}^{n}$ is the concentration vector for species *i* produced by the SI scheme at the previous time step (M/L^3), $\boldsymbol{R}_i^{m}$ is the reactive source-sink vector (M/L^3/T), $\boldsymbol{C_i}$ is the concentration vector

for species *i* and is dependent on the time discretization scheme, and *m* represents the iteration level. The second phase of the SI scheme involves the solution of the reactive component using,

$$\frac{\boldsymbol{Cc}_i^{n+1,m+1} - \boldsymbol{C}_i^{n+1,m+1}}{\Delta t} = \mathcal{L}_{\mathcal{R}}\left(\boldsymbol{C}_1, \boldsymbol{C}_2, ..., \boldsymbol{C}_i, ..., \boldsymbol{C}_{NC}\right) \tag{3.49}$$

where $\boldsymbol{Cc}_i^{n+1,m+1}$ is the concentration vector for species *i* after reactive transport (M/L^3) and is used to update the reactive source-sink vector,

$$\boldsymbol{R}_i^{m+1} = \frac{\boldsymbol{C}_i^{n+1,m+1} - \boldsymbol{Cc}_i^{n+1,m+1}}{\Delta t} \tag{3.50}$$

Finally convergence can be calculated for each species by using,

$$CV_i^{m+1} = \left|\boldsymbol{C}_i^{n+1,m+1} - \boldsymbol{C}_i^{n+1,m}\right| \leq \xi \tag{3.51}$$

where ξ is some absolute concentration tolerance specified by the user.

3.4.1.4 Symmetric Sequential Iterative Scheme

The SSI approach is similar in principle to the SI scheme, except that the SSI scheme incorporates two source-sink terms to minimize splitting errors; these terms are described by Herzer and Kinzelbach (1989). The first term, a reactive source-sink vector $\boldsymbol{R_i}$, is introduced into the transport solution, and is identical to the reactive source-sink vector used in the SI scheme (Eq. (3.48)). The second term, a transport source-sink vector $\boldsymbol{Rt_i}$, is introduced into the reactive solution. The first step of the SSI scheme is to solve the ADE with the additional reactive source-sink term,

$$\frac{\boldsymbol{C}_i^{n+1,m+1} - \boldsymbol{C}_{SSI_i}^{n}}{\Delta t} = \mathcal{L}_{\mathcal{T}}\left(\boldsymbol{C}_i\right) - \boldsymbol{R}_i^{m} \tag{3.52}$$

where $\boldsymbol{C}_i^{n+1,m+1}$ is the concentration vector for species *i* at the current iteration and time step (M/L^3), $\boldsymbol{C}_{SSI_i}^{n}$ is the concentration vector for species *i* at the previous time step (M/L^3), $\boldsymbol{R}_i^{m}$ is the reactive source-sink vector at the previous iteration ($M/L^3/T$), and $\boldsymbol{C_i}$ is the concentration vector for species *i* and is dependent on the time discretization scheme. In the second step, the transport source-sink vector is calculated from,

$$\boldsymbol{Rt}_i^{m+1} = \frac{\boldsymbol{C}_{SSI_i}^{n} - \boldsymbol{C}_i^{n+1,m+1}}{\Delta t} - \boldsymbol{R}_i^{m} \tag{3.53}$$

where $\boldsymbol{Rt}_i^{m+1}$ is the transport source-sink vector for species *i* ($M/L^3/T$). The third step involves the solution of the reactive component using,

$$\frac{\boldsymbol{Cc}_i^{n+1,m+1} - \boldsymbol{C}_{SSI_i}^{n}}{\Delta t} = \mathcal{L}_{\mathcal{R}}\left(\boldsymbol{C}_1, \boldsymbol{C}_2, ..., \boldsymbol{C}_i, ..., \boldsymbol{C}_{NC}\right) - \boldsymbol{Rt}_i^{m+1} \tag{3.54}$$

where $\boldsymbol{Cc}_i^{n+1,m+1}$ is the reactive vector concentration for species *i* at the current iteration and time step (M/L^3). Finally, the last step updates the reactive source-sink term by using,

$$\boldsymbol{R}_i^{m+1} = \frac{\boldsymbol{C}_{SSI_i}^{n} - \boldsymbol{Cc}_i^{n+1,m+1}}{\Delta t} - \boldsymbol{Rt}_i^{m+1} \tag{3.55}$$

where $\boldsymbol{R}_i^{m+1}$ is the reactive source-sink vector for species *i* at the current iteration ($M/L^3/T$). Finally, convergence can be calculated for each species by using,

$$CV_i^{m+1} = \left|\boldsymbol{C}_i^{n+1,m+1} - \boldsymbol{C}_i^{n+1,m}\right| \leq \xi \tag{3.56}$$

where ξ is some absolute concentration tolerance specified by the user.

As previously mentioned the main attribute to using OS over one-step techniques is the reduction in computational effort; however, error is induced by splitting the transport and reactive terms (Herzer and Kinzelbach, 1989; Yeh and Tripathi, 1991; Zysset *et al.*, 1994; Barry *et al.*, 1996;

Steefel and MacQuarrie, 1996; and Carrayrou *et al.*, 2004). Steefel and MacQuarrie (1996) suggest that for a general problem, the SNI scheme errors are produced because reactions begin only after the transport process is complete, when in reality certain processes such as decay, continually reduce concentration. The SS approach produces less error than the SNI because the reaction process occurs between two transport steps, yielding a solution closer to the analytical expression than the SNI scheme (Steefel and MacQuarrie, 1996). However, some SS error can be induced if a large time step is employed; a small time step reduces this error production but consequently increases computational effort. Barry *et al.* (1996) and Steefel and MacQuarrie (1996) also suggested that the accuracy and computational efficiency of the SS scheme is dependent on the application. When linear equilibrium sorption was considered, Barry *et al.* (1996) and Steefel and MacQuarrie (1996) determined by Taylor series expansion that the linear retardation transport equation is only first-order accurate. Although Barry *et al.* (1996) and Steefel and MacQuarrie (1996) only considered the linear equilibrium case, they stated that the results for non-linear sorption would be the same. According to Herzer and Kinzelbach (1989), Engesgarrd and Kipp (1992), Steefel and MacQuarrie (1996), the problem that exists when using iterative approaches is conditional stability. In general, Herzer and Kinzelbach (1989) concluded that stability and the rate of convergence is dependent on the "numerical approximation of the transport process and the magnitude of the explicitly introduced source/sink term, which couples the two sets of equations".

Carrayrou *et al.* (2004) conducted a study that examined linear irreversible and reversible first-order chemical reactions for the four OS schemes detailed above. Among other things, they performed a computational cost analysis, and determined that in terms of computational

efficiency the OS schemes ranked in the following order (from the most to least efficient): SSI, SS, SNI, and SI. The SI scheme ranked the lowest because of the heavy Δt dependency; computational time increases for a small Δt and conversely for a large Δt since this increases the number of iterations. The SSI scheme ranked the best since its computational time is not dependent on Δt. Carrayrou *et al.* (2004) also applied a Taylor series expansion to each of the schemes, and determined that the SSI scheme does not induce any splitting error, the SS scheme was second-order accurate, and the SNI and SI schemes were first-order accurate. Therefore, due to its poor efficiency and low accuracy, Carrayrou *et al.* (2004) recommended that the SI scheme not be used at all and that SSI scheme was by far the best.

In summary, previous studies indicate that each scheme, with the exception of SSI, have certain limitations depending on the type of problem being examined, and that all schemes are sensitive to Δt; however, the SSI scheme is superior to the other schemes because no splitting errors are induced (Carrayrou *et al.*, 2004). Since all of these four schemes are limited under different conditions, they all were implemented into the DFRTT model to maintain the versatile nature of this model.

3.4.2 Discretization of Transport Operator

As discussed in Section 3.3, a streamline-oriented CV mesh was implemented to solve the ADRE. The adapted OS approach decouples the ADRE into transport and reactive operators. The numerical solution of the transport operator was performed using the finite volume method, which as a starting point, uses the integral form of the mass conservation equation Eq. (3.29) for a single species expressed by,

$$\frac{\partial}{\partial t}\int_V \theta C \; dV = \int_S \boldsymbol{D}\nabla C \cdot \hat{\boldsymbol{n}} \; dS - \int_S C\hat{\boldsymbol{q}} \cdot \hat{\boldsymbol{n}} \; dS \tag{3.57}$$

where $\boldsymbol{D}$ is a dispersion tensor (L^2/T), $\hat{\boldsymbol{q}}$ is the velocity vector, γ is a source-sink term, and $\hat{\boldsymbol{n}}$ is the outward unit normal vector. The integral form of the mass conservation equation (Eq. (3.57)) is applied to each CV of the SOM, and each integral in Eq. (3.57) must be numerically approximated to obtain a control volume algebraic equation. Details of these approximations are described in Appendix A.

Due to the nature of the rapidly diverging and converging flow field, special attention was given to the numerical approximation used to represent the advective integral. Specifically, three schemes were implemented into the DFRTT model to interpolate the nodal values at the CV surfaces: the linear interpolation or central difference scheme (CDS), an upwind interpolation or upwind differencing scheme (UDS), and a bounded second-order upwind differencing approximation (SOU) with linear deferred correction (LDC). The CDS is the most widely used interpolation approach due to its second-order accuracy (in space) for a uniform mesh spacing; however, it is only first-order accurate for a non-uniform mesh and it also produces unwanted oscillations for advective dominated transport situations (cell Peclet number> 2) (Leonard, 1979; Ferziger and Peric, 1999). The UDS never results in oscillatory behaviour, however, it is only first-order accurate in space which gives rise to unwanted numerical dispersion and therefore requires high mesh resolution to generate accurate solutions (Leonard, 1979). The SOU scheme coupled with LDC is second-order accurate but iterations are required to update the deferred correction terms and to ensure the solution is locally bounded (Barth and Jespersen, 1989; Seth et *al.*, 2005). The numerical details associated with these three schemes are presented in Appendix A.

3.4.3 Solution of the Reactive Component

A fourth-order Runge-Kutta numerical method scheme was used to solve the reactive component due to its simplicity (Ferziger and Peric, 1999).

3.4.4 DFRTT Model Input

Currently the model has the ability to simulate the injection and processes of a conservative, sorbing, and decaying tracer for a wide range of aquifer property identification (biodegrdation, sorption, etc.). The computational effort required to simulate all three tracers simultaneously can become quite substantial, and in some cases unnecessary. In order to minimize computational effort, the model was designed so that the user can select which tracer(s) is to be injected by indicating a specific "mode" of model operation. Currently, four modes exist within the model, one of which is used for Monod kinetics (Table 3.2). Mode 1 simulates a conservative tracer, while Mode 2 simulates a conservative, sorbing and decaying tracer (neither of which interacts with the others). Mode 3 simulates a conservative, sorbing, and decaying tracer as well as some other aqueous species, which interacts with a user defined solid species already present within the subsurface. Finally, the fourth mode is for a Monod kinetics type problem, where a conservative tracer is simulated along with an electron acceptor and substrate. The various tracers are subject to the general ADRE, where the reactive component for each tracer is described in Section 3.3.1. A general flow chart of the CRTM operations is shown in Figure 3.3. A sample input data set and model input guide is incorporated into Appendix B.

Table 3.1: Examples of tracers to be examined, the processes to be captured, and their reaction expressions.

Tracer Type	Examples	Purpose	Reaction Expression
Inert	Bromide	to determine dispersion	N/A
Sorbing	Fluorotricloromethane Various CFCs	to capture sorption processes such as adsorption and chemisoption	Equilibrium: $\rho_b \frac{\partial C_s}{\partial t} = \rho_b \frac{\partial \left(k_d C_w^{\ N} \right)}{\partial t}$ Non-equilibrium: $\gamma_{sorb} = \rho_b \frac{\partial C_s}{\partial t} = \rho_b \alpha \left(k_d C_w - C_s \right)$
Decaying	Sulphate	to determine rates of degradation	$\gamma_{decay} = -k \theta C_w^{\ N}$
Biodegrading	Methanol/Acetate (O_2 Reducing)	to determine biodegrdation rates and the extent of the reaction by examining the recovery of the electron donor(s) (methanol/acetate) and electron acceptor(s) (O_2, NO_3^-)	$\gamma_{S\beta} = -k_{max\beta} M \theta \frac{S_\beta}{S_\beta + K_{S\beta} + \frac{S_\beta^{\ 2}}{K_{I\beta}}} \frac{A}{A + K_A}$ $\gamma_A = -k_{max\beta} M \theta X_\beta \frac{S_\beta}{S_\beta + K_{S\beta} + \frac{S_\beta^{\ 2}}{K_{I\beta}}} \frac{A}{A + K_A}$ $\frac{dM}{dt} = k_{max\beta} M Y_\beta \left(1 - \frac{M}{M_{max}} \right) \frac{S_\beta}{S_\beta + K_{S\beta} + \frac{S_\beta^{\ 2}}{K_{I\beta}}} \frac{A}{A + K_A} - bM$

Table 3.2: Summary of different injection modes and simulated tracers.

Injection	Mode 1	Mode 2	Mode 3	Mode 4
Conservative	X	X	X	X
Sorbing		X	X	
Decaying		X	X	
Aqueous Species			X	
Electron Acceptor				X
Substrate				X

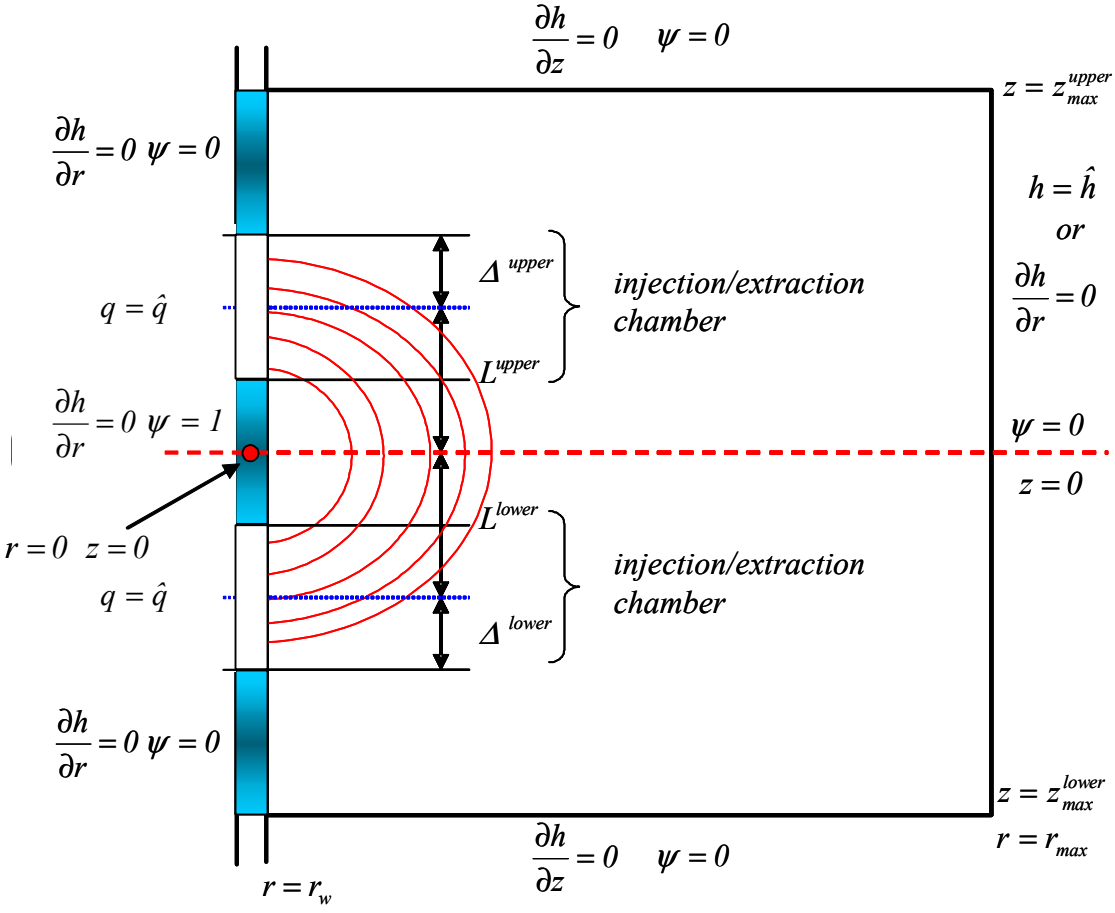

Figure 3.1: Spatial domain, and boundary conditions for stream function and hydraulic head dipole flow field calculations.

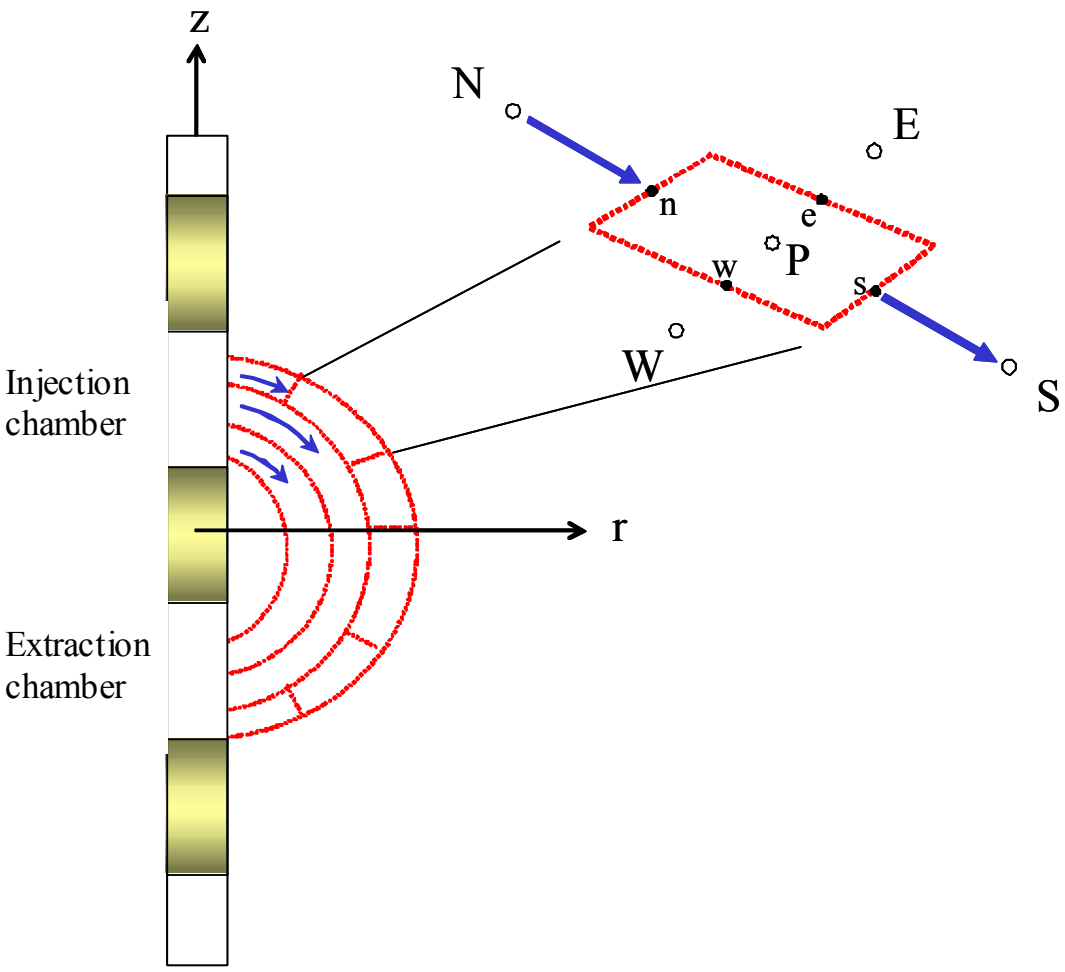

Figure 3.2: Dipole flow field showing typical streamtubes, a portion of the streamline oriented mesh, and a control volume. Neighbouring computational nodes are indicated by the open circles and integration points by the solid circles.

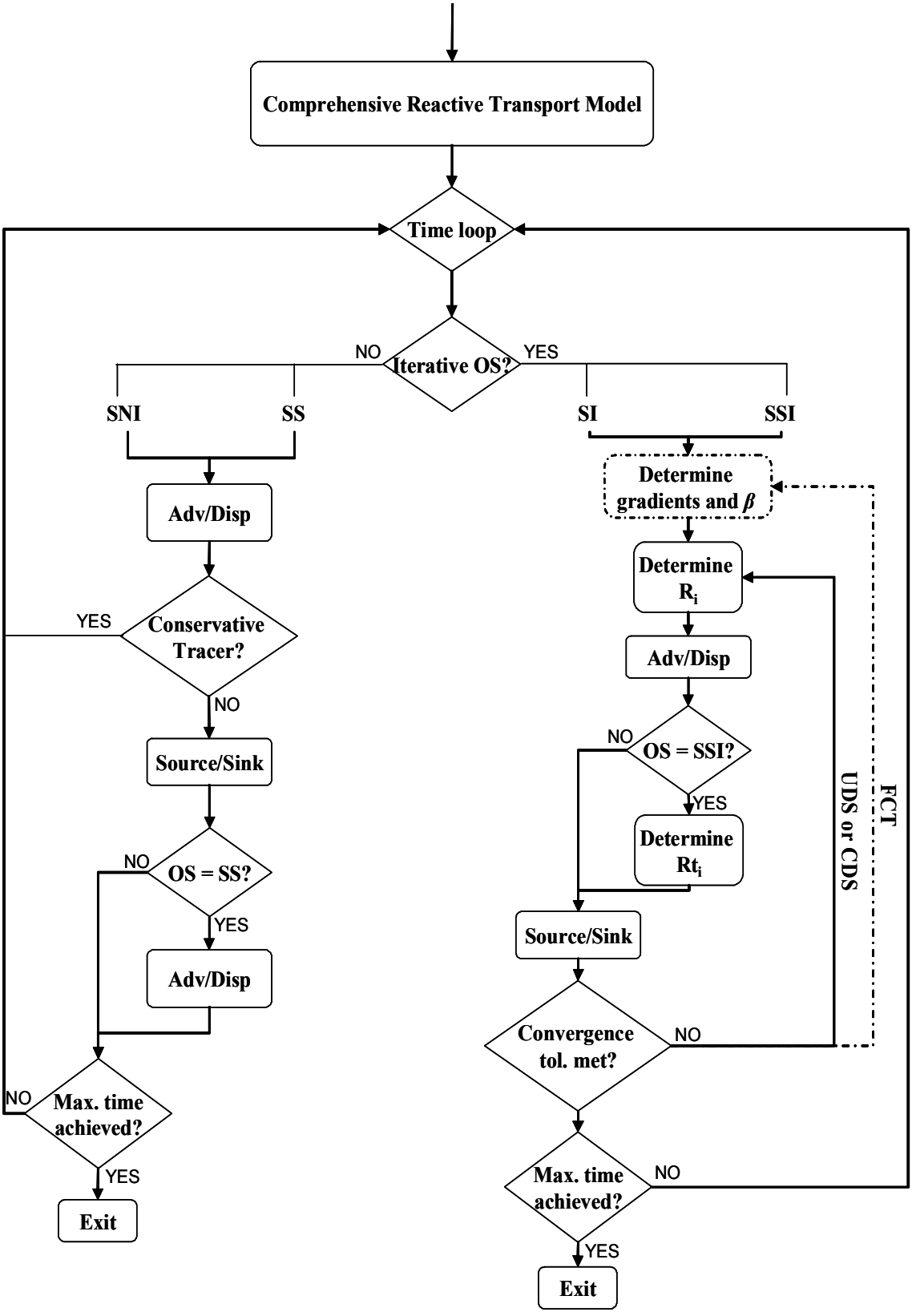

Figure 3.3: Basic structural outline of the comprehensive reactive transport operations for Mode's 1 thru

CHAPTER 4 DFRTT MODEL VALIDATION AND SENSITIVITY

This chapter focuses on validating the transport component of the DFRTT model by comparing simulation results produced by the advective-dispersive streamtube model and MODFLOW/MT3DMS to the CRTM results. The behaviour of the advective and operator-splitting schemes will also be examined.

4.1 VALIDATION

This investigation had two primary objectives. The first objective was to validate the CRTM, by comparing BTCs generated by the existing advective and advective-dispersive streamtube models. The second objective was to compare the CRTM BTCs to those produced by an "off-the-shelf" model so that the CRTM can be validated against a widely accepted hydrogeologic model. In addition, the BTCs generated by an existing hydrogeologic model will illustrate the difficulties an "off-the-shelf" model encounters when it is used to model the dipole's rapidly converging and diverging flow field and thereby justifying the need to utilize a dipole specific model for a DFRTT application.

4.1.1 Base Case Simulation

Since the introduction of the DFT system, there have been several feasibility studies conducted at field sites in Europe and North America (e.g., Zlotnik and Zurbuchen, 1998; Hvilshøj *et al.*, 2000; and Zlotnik *et al.*, 2001) and the dipole (DP) tool dimensions and test flow rates used in these studies vary depending on site characteristics (Δ = 0.25 to 0.30 m, r_w = 0.0125 to 0.075 m, L = 0.39 to 0.55 m, and Q = 2.3×10^{-6} to 1.1×10^{-3} m^3/s). There has been one known successful field application of the DFTT (Sutton *et al.*, 2000) and the DP dimensions used were Δ = 0.43 m, r_w = 0.058 m, L = 0.84 m, and Q = 1.6×10^{-4} m^3/s. Since we are interested in determining aquifer

properties obtained from a reactive tracer test and not from a dipole flow test we have chosen, for base case simulation purposes, to implement DP dimensions and a flow rate similar to those used by Sutton *et al.* (2000) (Table 4.1). A conservative tracer with a 2-hour injection period and a test duration of 1 day were used for the these simulations because (1) they can be used in the field to obtain 100% mass recovery within a few days, and (2) they reduce computation effort. Well skin and wellbore effects were assumed to be negligible, and a homogeneous hydraulic conductivity field with no horizontal confining features or conductive layers was used.

The stream function and hydraulic head fields for this base case simulation are shown in Figure 4.1. The resulting BTC from the advective streamtube model (conservative tracer), using 2000 streamtubes and 50% of the flow field, is shown in Figure 4.2(a). For comparison purposes, the following BTC metrics are used: time-to-peak (t_p); arrival time of the tracer front (t_f) which is defined here as 5% of the peak concentration (C_p); the first arrival time ($t_{0.1}$) which is defined here as 0.1% of the peak concentration; and the centre of mass (t_c) of the BTC which is dependent on the simulation end point. It should be mentioned that the first non-zero point on the advective streamtube model BTC represents the travel time it takes a particle to advect from the injection to the extraction chamber along the innermost streamtube. This travel time is dependent on the dipole length and the aquifer's anisotropy ratio. The shape of the BTC tail is largely dependent on the percent of the flow field used to construct the BTC as well as the travel time along the outermost streamtube. In this case only 50% of the flow field was used; however, if the percent contribution is reduced to a value significantly less than 50%, the tail of the BTC ends prematurely. For example Figure 4.2(b) shows a BTC simulated using only 10% of the flow field. In comparison to Figure 4.2(a) the BTC from the smaller flow field shows a smaller peak

concentration and an early (100%) mass recovery. The arrival time distribution, associated with the BTC shown in Figure 4.2(a), is presented in Figure 4.3 and indicates that by 1 day only 42% of the injected flow associated with the conservative tracer has reached the extraction chamber. The arrival time distribution also indicates that ~ 13% of the flow field is contributing to the C_p in Figure 4.2(a), which occurs at ~ 0.17 days. The inflection point denoted on Figure 4.3 occurs at ~ 0.38 days and corresponds approximately to the BTC centre of mass, which is equivalent to the mean arrival time of ~ 27% of the injection chamber. In theory the inflection point of the advective arrival time distribution should correspond to the BTC centre of mass for an instantaneous source.

As mentioned, the arrival time distribution (Figure 4.3) indicates that only 13% of the flow field contributed to the peak concentration, and that any flow contribution greater than 13% was responsible for the shape of the BTC tail. Ideally it is desirable to examine 100% of the flow field; however, this significantly increases computational effort and does not alter the BTC. Therefore, two SOMs were constructed using only 50% of the flow field contribution. The first SOM, denoted as the "fine SOM" was built using 83 streamtubes; this SOM will be used for the majority of the simulations unless otherwise indicated (Figure 4.4(a)). The second SOM is a less refined mesh and was built using 53 streamtubes; this SOM is referred to as the "coarse SOM" (Figure 4.4(b)).

Figure 4.5(a) shows the BTC results obtained from the advective and advective-dispersive streamtube models, as well as the CRTM using the CDS advective scheme and the "fine SOM". To satisfy the constraint required by the advective-dispersive streamtube model (Eq. 3.23), a

longitudinal dispersivity coefficient of 0.001 m was used. For comparison purposes, the effective diffusion and transverse dispersivity coefficients were set to zero for the CRTM simulation. In general the BTCs correspond well to one another although there were differences between the $t_{0.1}$ and the C_p values (Table 4.2). The differences exhibited in Figure 4.5(a) are a result of the slight dispersion captured by the CRTM and the advective-dispersive streamtube model, which caused a spread in the BTCs, yielding an earlier $t_{0.1}$ and lower C_p. Approximately 41.8% of the conservative tracer was captured by all three models. The CRTM mass balance error (MBE) was $\sim -1.41 \times 10^{-2}$ %. When the longitudinal dispersivity coefficient is increased from 0.001 m to 0.01 m and then 0.1 m, the influence of dispersion is more pronounced (Figure 4.5(b, c), Table 4.2). For a longitudinal dispersivity coefficient of 0.01 m the CRTM and advective-dispersive streamtube model BTCs compare fairly well at the front although there is a slight discrepancy at the peak. The most obvious difference between the advective-dispersive streamtube model and the CRTM BTCs occurred when a longitudinal dispersivity coefficient of 0.1 m was employed (Figure 4.5(c)); this difference is due to a violation of the assumption inherent in the advective-dispersive streamtube model (Eq. 3.23). To yield acceptable results from the advective-dispersive streamtube model, the dispersed zone must travel a distance 100 times the dispersivity coefficient of the aquifer. Therefore, if the dispersivity coefficient was approximately 0.1 m (accepted standard of practice to equate dispersivity to approximately 10% of the spatial scale, 1.6m) then the dispersed zone must travel at least 10 m. Unfortunately, this is not possible with our DP dimensions since the minimum dispersed travel zone distance would be ~ 1 m, which is the distance along the wellbore (between the two chambers). However, for the smaller dispersivity coefficients (α_L = 0.001 and 0.01 m) the advective-dispersive streamtube model solution compares well with the CRTM solution since the criterion has been met. The MBEs for

the 0.01 m and 0.1 m simulations were 1.37×10^{-2}% and 1.28×10^{-2}%, respectively, while approximately 41% of the conservative tracer was captured (for both longitudinal dispersivity coefficients). The similar BTC metrics and shapes indicate that the CRTM has been successfully validated against the advective streamtube model and the advective-dispersive streamtube, for a conservative tracer in a highly advective dipole flow system.

Figure 4.6 illustrates the temporal variation of cumulative mass balance error (CMBE) and the mass entering and exiting the system. The first non-zero point of the CMBE profile (Figure 4.6(c)) occurred at the same time mass began exiting the system (~ 0.08 days, Figure 4.6(b)). The negative CMBE values are likely attributable to CDS over-estimating the amount of mass exiting the system, which would occur if the montonicity condition has been exceeded. Inspection of the SOM yielded that the majority of its CVs exceeded the Péclet condition; the largest local Péclet number was determined to be 363.1. The CMBE, in Figure 4.6(c), continues to increase until the rate of change of mass exiting the system decreases at ~ 0.26 days; at this point, the CMBE decreases at approximately the same rate as the total mass exiting the system because the exiting mass becomes increasingly insignificant (and mass recovery becomes substantial).

4.1.2 MODFLOW/MT3DMS Validation

In order to validate the CRTM with a current off-the-shelf model, the results produced by the CRTM were compared to the results produced by MODFLOW/MT3DMS. The Visual MODFLOW Pro modelling environment (Version 2.83, Waterloo Hydrogeologic Inc., 2002) was chosen for use in this validation investigation with MODFLOW-2000 (Zheng *et al.*, 2001)

as the numeric flow engine, and the Modular 3-Dimensional Multi-Species Transport Model (MT3DMS) (Zheng and Wang, 1998) as the primary mass transport numeric engine. A series of preliminary simulations were conducted to determine the combination of domain size, grid discretization, dipole flow rate and mass transport solver parameters required to produce conservative tracer BTCs with minimal numerical dispersion and oscillations. Numerical issues inherent with the standard finite difference and the hybrid modified method of characteristics (HMOC) mass transport solution techniques could not be overcome, and therefore the third-order total variation diminishing (TVD) mass-conservative scheme (Zheng and Wang, 1998) was used exclusively.

As a result of the extensive preliminary testing a 40 x 40 x 11 m (x, y, z; width/length/depth) spatial domain with the dipole device centrally located was used for all simulations performed in this study. These dimensions were selected to represent a relatively thin shallow unconfined aquifer system with areal limits (x, y) sufficiently removed from the well bore that they would not impact the developed flow field. The central 8 x 8 m zone was discretized into 0.1 x 0.1 x 0.1 cells to ensure high numerical resolution in the vicinity of the well bore where the bulk of mass transport occurs. An increasing discretization scheme was used outside of this central zone. Two wells with a screen length of 1 m and separated by a vertical distance of 1 m were employed to simulate the dipole probe device. The upper screen was used to represent the source or injection chamber, and the lower screen was used to represent the sink or extraction chamber. Cells located above and below each well screen were designated “inactive” with respect to flow and transport thereby representing sections of the well occupied by inflatable packers and inaccessible to groundwater. No flow boundaries were assigned around all external boundaries.

Where possible the symmetric nature of the flow field was exploited to improve computational efficiency. The system BTC was obtained by averaging the concentration at ten observation points placed along the extraction well.

To match the dipole parameters, flow rate and coefficients used in the preliminary testing of MODFLOW/MT3DMS, the parameter values listed in Table 4.1 were used in the CRTM. To reduce computational effort, only 40% of the flow field was considered. As explained in Section 4.1.1, reducing the flow field for transport only impacts the BTC tail and not the BTC front or peak concentration. The resulting SOM and stream function field are contained in Appendix C. The MODFLOW/MT3DMS and CRTM BTCs for a conservative tracer, first-order decaying tracer, and sorbing tracer are shown in Figure 4.7, 4.8 and 4.9. The conservative tracer BTCs (MBE ~ 3.8×10^{-10}%) in Figure 4.7(a), the decaying tracer BTCs (MBE ~ 6.9×10^{-3}%) in Figure 4.8(a) and (b), and the linear sorbing tracer (MBE ~ 3.2×10^{-2}%) in Figure 4.9(a) demonstrate that the two models correspond well (for the respective tracer) since the $t_{0.1}$, peak concentration, and t_p values are almost identical for both models (Table 4.3). As anticipated, deviation between the MODFLOW/MT3DMS and CRTM BTC tails occur (all panels in Figure 4.7) and is attributable to the reduced flow field represented by the transport model, as explained in Section 4.1.1. This issue could easily be rectified by increasing the flow field contribution to a value greater than the 40% that is used in this simulation.

Although the conservative tracer BTCs corresponded well when a longitudinal coefficient of 0.1 m was employed, the inability of MT3DMS to handle the advective dominated problem

manifested itself, as oscillatory behaviour, when the longitudinal dispersivity coefficient was decreased to 0.01 and 0.001 m (Figure 4.7(b) and 4.7 (c)).

Figure 4.9(b) and 4.9 (c) show the resulting BTCs when a Freundlich isotherm with an n value of 1.5 and 0.5 is applied. For both of these cases, the BTCs do not compare well. The CRTM under-predicts the peak concentration (for both n values) and produces a different tail shape when n = 1.5 (attributable to the flow field contribution). It is unclear as to why the two models do not correspond well when $n \neq 1$; however, it can only be presumed that the problems exist within MODFLOW/MT3DMS since the Freundlich and linear sorption isotherms within the CRTM are treated in a similar manner.

The resulting BTCs from this investigation indicate that under certain conditions the CRTM has been validated against MODFLOW/MT3DMS for the conservative, first-order decaying and linear sorbing tracers, despite the fact that the molecular diffusion coefficient for MODFLOW/MT3DMS is active (and inactive for the CRTM). This investigation also indicates the difficulties MODFLOW/MT3DMS has handling the rapidly converging and diverging dipole flow field, and therefore affirms the need for a dipole specific model when modelling a DFRTT application.

4.2 EVALUATION OF ADVECTIVE SCHEMES

The purpose of this section is to evaluate the performance of the various advective schemes (using Crank-Nicholson temporal weighting) implemented in the CRTM (Section 3.4). This evaluation was accomplished by increasing the base case dispersivity and flow rate values, and

by performing simulations using the coarse SOM. These variables were selected because they affect the local Péclet number and in turn, the performance of conditionally stable schemes. The local Péclet number is given by,

$$Pe = \frac{\overline{q}\Delta l_{sn}}{D_{avg}} \tag{4.1}$$

where $\overline{q}$ is the average flux (L/T), Δl_{sn} represents the length from the north CV face to the south CV face (L), and D_{avg} is average dispersion based on the longitudinal dispersivity coefficient, the average flux, porosity and effective molecular diffusion (L^2/T).

Since the BTC is based on a flow-weighted average along the extraction chamber, the impact of CVs that exceed the Péclet condition (Péclet > 2) within the SOM may not be evident in the BTC. An advective scheme can be classified as producing unacceptable results if the normalized temporal concentration field (C/C_o) is unbounded (i.e., indicating osciallatory behaviour) at any point within the computational domain. In this investigation we used a tolerance of $1.0x10^{-3}$ to classify an unbounded solution, which is two orders of magnitude higher than the solver tolerance. When comparing the BTCs produced by the various advective schemes, the UDS is expected to produce the most amount of numerical dispersion, which will manifest as enhanced smearing of the BTC and generate the smallest peak concentration. When the CDS, a conditionally stable scheme, yields a monotone solution it should exhibit the least amount of numerical dispersion and therefore the largest peak concentration. If the Péclet condition is exceeded at any point within the domain then the solution will appear to be non-monotone, which may manifest as oscillatory behaviour of the BTC.

Figure 4.10(a) and 4.10(d) show the BTCs generated by the CDS, UDS and FCT method for the fine and coarse mesh, using base case parameters (Table 4.1), where the largest local Péclet number was determined to be 363.1 (fine SOM) and 410.8 (coarse SOM). As anticipated, the UDS had the earliest $t_{0.1}$ and smallest C_p values for both SOMs (Table 4.4), while the CDS had the latest $t_{0.1}$ and largest C_p values (Table 4.4). The FCT scheme had $t_{0.1}$ and C_p values which fell between the other two BTCs (Table 4.4). The FCT method will never be able to reproduce the same BTCs as the UDS or CDS because its order of accuracy is dependent on the blending factor value, which is spatially variable. Although oscillatory behaviour was absent from the fine SOM CDS BTC (Figure 4.10(a)), it was apparent in the coarse SOM BTC at ~ t = 0.4 days (Figure 4.10(f)) since the majority of the SOM CVs exceeded the Péclet condition. Examination of the temporal concentration fields indicated that the CDS was the only advective scheme to be unbounded, which deems CDS as an unacceptable scheme for both the fine and coarse SOM under the given conditions. It should be noted that the CDS was used to successfully generate the BTCs shown in Figure 4.5 (under these same conditions); however, in that early investigation CDS was chosen based on its second-order accuracy and because it is a widely accepted differencing scheme.

Figure 4.11(a) shows the resulting CDS, UDS and FCT BTCs when the longitudinal dispersivity coefficient was increased from 0.001 to 0.1 m. The increased longitudinal dispersivity coefficient resulted in very few CVs exceeding the Péclet condition, and the largest local Péclet number was 3.6. Once again, the UDS BTC had the earliest $t_{0.1}$ value while the CDS BTC demonstrated the latest (Figure 4.11(b)). Interestingly, the UDS BTC also demonstrated the largest peak concentration even though it was hypothesized to be the smallest of all three advective schemes

(Figure 4.11(c)). It is unclear as to why the UDS scheme produced the largest peak concentration; however, the discrepancy may be related to the fact that the BTC is based on an averaged concentration along the extraction chamber. This should be investigated further. Examination of the temporal concentration fields indicated that CDS, UDS and the FCT method produced bounded solutions.

Figure 4.12(a) and (b) illustrates the BTC for the CDS, UDS and FCT method when the flow rate was increased to 5.0×10^{-4} m^3/s. All of the SOM CVs exceeded the Péclet condition, and the largest local Péclet number was 366. As expected, the CDS oscillatory behaviour (at $t \sim 0.2$ days) resulted in response to the highly advective conditions (Figure 4.12(c)). The CDS was the only scheme to contain unbounded values within the temporal concentration field; under these conditions CDS is deemed unacceptable.

When CDS was determined to contain unbounded values, both UDS and FCT were able to produce acceptable solutions. The computational speed of UDS makes it a desirable approach since it involves a minimum of 2 iterations; however, its first-order accuracy is evident in its production of numerical dispersion and makes it less desirable than higher-order schemes. Although the FCT scheme is second-order accurate (when $\beta \neq 0$), it involves a minimum of three iterations, per time step, making it slower than UDS and/or CDS.

4.3 OPERATOR-SPLITTING SCHEMES

As discussed in Section 3.4.1 the CRTM contains four OS schemes, which include iterative (SSI and SI) and non-iterative techniques (SNI and SS). The purpose of this section is to determine

the best CRTM OS scheme by examining the resulting MBE (BTCs cannot be used in this analysis because they are essentially identical). A conservative, first-order decaying and linear sorbing tracer was simulated for each OS technique and their resulting MBEs were inspected. The UDS was used for both the iterative and non-iterative OS techniques, and for comparison purposes the FCT method was also employed but only for the iterative OS techniques. The MBEs were examined after physical and numerical model parameters were altered; these include a decreased longitudinal dispersivity coefficient (Case 1; α_L = 0.001 m), a coarse SOM (Case 2), an increased and decreased time step size (Case 3 and 4; Δt = 100 and 0.1 sec), increased first-order decay and linear distribution coefficients (Case 5; $\lambda = 5\text{x}10^{-3}$ sec^{-1} and $k_p = 1.8\text{x}10^{-2}$ m^3/kg), and an increased flow rate (Case 6; $Q = 5.0\text{x}10^{-4}$ m^3/s). The base case parametric values for this investigation are included in Table 4.1 (except that a longitudinal dispersivity coefficient of 0.1 m was used).

The resulting MBEs from the base case simulations indicate that the OS techniques which employ UDS are all within the same order of magnitude ($1.0\text{x}10^{-2}$ %), regardless of the tracer, and that SI_{FCT} and SSI_{FCT} generate a MBE that is up to six orders of magnitude smaller than the other OS techniques (Table 4.5). The SSI_{FCT} and SI_{FCT} approaches yielded similar MBEs for both the conservative and linear sorbing tracers ($1.0\text{x}10^{-8}$ % and $1.0\text{x}10^{-9}$ %); however, the SI_{FCT} outperformed the SSI_{FCT} for the decaying tracer, by one order of magnitude. The FCT method goes through more iterations than the UDS (FCT: minimum of three, UDS: minimum of two), which results in better MBEs for SI_{FCT} and SSI_{FCT} in comparison to OS techniques employing UDS. The MBEs for Case 1 (α_L = 0.001 m) and Case 2 (coarse SOM) yielded similar results to the base case simulations.

When the time step size was increased to 100 sec (Case 3) the MBEs for the decaying tracer indicated that the iterative techniques (for both UDS and FCT) conserved more mass than the non-iterative techniques, by a minimum of one order of magnitude (Table 4.5). Since accuracy of the fourth-order Runge-Kutta method (used to solve the sink term) is governed by the time step size (Trench, 2000), the larger time step size resulted in complete mass depletion within a single time step. Unfortunately this mass depletion could not be corrected by the non-iterative techniques. This issue can be rectified by employing a higher-order numerical method and/or using a different time step size to solve the source/sink term. It should be noted that the Strang-Splitting technique also had larger MBEs for the conservative and sorbing tracers. This was not surprising since it has been shown by others (Barry *et al.*, 1996; and Steefel and MacQuarrie, 1996) that the splitting errors induced by this technique increase as the time step also increases. When the time step size was decreased to 0.1 sec (Case 4) the resulting MBEs were similar to those obtained from the the base case simulation (Table 4.5). An increased decay coefficient, 5.0×10^{-3} sec^{-1} (Case 5), resulted in large decaying tracer MBEs for the non-iterative approaches (similar to those shown when the time step size was also increased); this was due to the more prominent sink term. Again, the iterative techniques conserved more mass than the non-iterative OS approaches (by a minimum of six orders of magnitude) for the same reasons explained earlier. When comparing the SSI_{FCT} to SI_{FCT} MBEs, (Cases 3, 4 and 5) it is evident that the SI_{FCT} MBE is smaller (by a minimum of three orders of magnitude) for the decaying tracer; this suggests that SI_{FCT} is better than SSI_{FCT}. However, SI_{FCT} is computationally more expensive (also determined by Carrayrou *et al.*, 2004) since it typically runs up to six iterations, while SSI_{FCT} usually runs three.

More mass was conserved for the conservative and sorbing tracers (all OS techniques) when the flow rate was increased to 5.0×10^{-4} m^3/s. The MBEs for the decaying tracer did not significantly improve the OS techniques employing UDS because the sink term is dependent on the time step size and not the flow rate (as previously explained). Comparisons between the SI_{FCT} and SSI_{FCT} showed that the MBEs were the same for the conservative and sorbing tracers; however, the SI_{FCT} MBE was three orders of magnitude smaller than the SSI_{FCT}. Again, the SI_{FCT} was found to be more computationally expensive than the SSI_{FCT}.

In general, this study demonstrated that there were no significant differences between the non-iterative and iterative techniques using UDS unless the sink term became prominent (large decay coefficient and/or large time step size), in which case the SSI_{UDS} and SI_{UDS} were deemed superior over the SNI_{UDS} and SS_{UDS}. As expected, when a large time step was employed the splitting errors for SS_{UDS} increased and exceeded those produced by SNI_{UDS}. This investigation also repeatedly demonstrated that the MBEs for SI_{FCT} and SSI_{FCT} were better than the OS techniques employing UDS because the FCT method runs through more iterations per time step than the UDS. The extraordinary results produced by the SI technique were surprising since it is only first-order accurate and was previously determined, by Carrayrou *et al.* (2004), to be the worst OS approach. Based on the findings of this investigation, it is recommended that iterative techniques be employed; however, since SI requires significant computational effort, it is recommended that SSI be chosen for subsequent CRTM simulations (with FCT as the recommended advective scheme).

Table 4.1: Summary of parameter values.

Parameter	Base Case	MODFLOW/MT3DMS
Tracer	Conservative	Conservative
Initial Concn. of Tracer (kg/m^3)	1.0	1.0
Injection Length (hr)	2.0	2.0
Δt (sec)	1.0	1.0
Test Period (day)	1.0	10.0
Q (m^3/s)	1.00E-04	1.15E-05
L (m)	0.8	1.0
Δ (m)	0.3	0.5
r_w (m)	0.05	0.05
α_L (m)	0.001	0.1
α_T (m)	0.0	N/A
D_m (m^2/s)	0.0	N/A
ρ_b (kg/m^3)	1850	1750
θ	0.33	0.33
$K_r = K_z$ (m/s)	1.00E-05	1.00E-05
Fraction of Flow	50%	40%

Table 4.2: Summary of the BTC characteristics for the base case simulation.

Model	Dispersivity Coefficient (m)	$t_{0.1}$ (days)	t_p (days)	t_f (days)	Peak Concentration	t_c (days)
Advective Streamtube	-	8.01E-02	1.71E-01	8.91E-02	1.31E-01	3.89E-01
Advective	0.001	7.49E-02	1.71E-01	8.79E-02	1.21E-01	3.89E-01
Dispersive	0.01	5.49E-02	1.71E-01	7.91E-02	1.15E-01	3.89E-01
Streamtube	0.10	2.21E-02	1.75E-01	4.71E-02	8.49E-02	3.84E-01
	0.001	6.11E-02	1.71E-01	8.49E-02	1.21E-01	3.72E-01
CRTM	0.01	5.49E-02	1.72E-01	7.51E-02	1.17E-01	3.89E-01
	0.10	2.21E-02	1.55E-01	4.51E-02	1.01E-01	3.75E-01

Table 4.3: Summary of the BTC characteristics for all three tracers for the CRTM and MODFLOW/MT3DMS simulations.

Model	Parameter	Conservative (α_L=0.1m)	Conservative (α_L=0.01m)	Conservative (α_L=0.001m)	1st Order Decay (λ=5x10^{-5} sec^{-1})	1st Order Decay (λ=2.5x10^{-5} sec^{-1})	Linear Sorption Isotherm	Freundlich Isotherm n=1.5	Freundlich Isotherm n=0.5
CRTM	$t_{0.1}$ (days)	1.81E-01	3.21E-01	3.59E-01	1.02E-01	1.01E-01	2.01E-01	1.01E-01	1.19E+00
	t_p (days)	7.01E-01	7.52E-01	7.01E-01	4.25E-01	5.02E-01	1.41E+00	1.01E+00	3.49E+00
	t_f (days)	2.11E-01	4.21E-01	4.03E-01	2.61E-01	3.03E-01	6.51E-01	3.01E-01	1.42E+00
	Peak Concentration	1.34E-02	1.78E-02	1.81E-01	1.68E-03	4.20E-03	6.70E-03	1.10E-02	9.01E-04
MODFLOW/ MT3D	$t_{0.1}$ (days)	1.81E-01	3.73E-01	4.01E-01	1.02E-01	1.01E-01	2.01E-01	1.01E-01	1.29E+00
	t_p (days)	7.01E-01	8.03E-01	7.01E-01	4.25E-01	5.02E-01	1.41E+00	1.19E+00	3.31E+00
	t_f (days)	2.11E-01	3.81E-01	3.81E-01	2.11E-01	3.03E-01	6.51E-01	2.51E-01	1.41E+00
	Peak Concentration	1.36E-02	1.58E-02	1.60E-02	1.70E-03	4.20E-03	6.70E-03	1.15E-02	1.26E-03

Table 4.4: Summary of BTC characteristics for different advective schemes.

Model	Parameter Altered	BTC Entry Time (days)	Time to Peak (days)	Arrival Time of Tracer Front (days)	Peak Concentration	Boundedness Issues?
SSI_{CDS}	Base Case	6.01E-02	1.71E-01	8.11E-02	1.21E-01	Yes
	Coarse SOM	5.49E-02	1.72E-01	7.81E-02	1.12E-01	Yes
	$\alpha_L = 0.1$ m	1.91E-02	1.59E-01	3.92E-02	9.79E-02	No
	$Q = 5.0 \times 10^{-4}$ m^3/s	3.11E-01	9.99E-02	1.81E-02	1.05E-02	Yes
SSI_{UDS}	Base Case	4.01E-02	1.59E-01	6.12E-02	1.12E-01	No
	Coarse SOM	4.81E-02	1.61E-01	5.92E-02	1.05E-01	No
	$\alpha_L = 0.1$ m	1.49E-02	1.65E-01	3.49E-02	1.01E-01	No
	$Q = 5.0 \times 10^{-4}$ m^3/s	3.15E-01	9.51E-02	1.49E-02	9.99E-03	No
SSI_{FCT}	Base Case	5.91E-02	1.65E-01	6.91E-02	1.15E-01	No
	Coarse SOM	5.39E-02	1.65E-01	6.91E-02	1.07E-01	No
	$\alpha_L = 0.1$ m	1.81E-02	1.65E-01	4.09E-02	9.81E-02	No
	$Q = 5.0 \times 10^{-4}$ m^3/s	3.13E-01	9.89E-02	1.61E-02	1.01E-02	No

Table 4.5: Mass balance errors produced from the various OS techniques.

OS Scheme	Tracer	Base Case	Case 1 (α_L = 0.001 m)	Case 2 (Coarse SOM)	Case 3 (Δt = 100 sec)	Case 4 (Δt = 0.1 sec)	Case 5 ($\lambda = 5x10^{-3}$ sec^{-1} & $k_p = 1.8x10^{-2}$ m^3/kg)	Case 6 ($Q = 5.0x10^{-4}$ m^3/s)
SNI_{UDS}	Conservative	-1.32E-02	-1.78E-02	-1.41E-02	-1.32E-02	-1.32E-02	N/A	-1.68E-05
	1st Order Decay	-2.59E-02	-2.87E-02	-2.92E-02	5.74E-01	-2.52E-02	9.32E-01	-1.53E-02
	Linear Sorbing	-2.88E-02	-3.73E-02	-3.17E-02	-2.88E-02	-2.88E-02	-2.10E-08	-1.04E-03
SS_{UDS}	Conservative	-1.33E-02	-1.79E-02	-1.42E-02	-3.70E-01	-1.01E-02	N/A	-1.73E-05
	1st Order Decay	-2.42E-02	-2.70E-02	-2.74E-02	1.47E-01	-2.57E-02	2.49E-01	-1.61E-02
	Linear Sorbing	-2.89E-02	-3.74E-02	-3.18E-02	-3.87E-01	-2.57E-02	-2.14E-08	-1.05E-03
SI_{UDS}	Conservative	-1.32E-02	-1.78E-02	-1.41E-02	-1.32E-02	-1.32E-02	N/A	-1.68E-05
	1st Order Decay	-2.59E-02	-2.87E-02	-2.92E-02	-2.59E-02	-2.59E-02	-5.48E-08	-1.69E-02
	Linear Sorbing	-2.88E-02	-3.73E-02	-3.17E-02	-2.88E-02	-2.88E-02	-2.10E-08	-1.04E-03
SSI_{UDS}	Conservative	-1.32E-02	-1.78E-02	-1.41E-02	-1.32E-02	-1.32E-02	N/A	-1.68E-05
	1st Order Decay	-2.57E-02	-2.86E-02	-2.89E-02	-2.59E-02	-2.58E-02	-5.49E-08	-1.69E-02
	Linear Sorbing	-2.88E-02	-3.73E-02	-3.17E-02	-2.88E-02	-2.88E-02	-2.10E-08	-1.04E-03
SI_{FCT}	Conservative	1.62E-08	9.33E-09	4.80E-08	2.41E-09	6.14E-09	N/A	1.83E-11
	1st Order Decay	-1.21E-05	-1.22E-05	-1.18E-05	1.34E-09	4.43E-10	8.32E-11	3.37E-09
	Linear Sorbing	8.81E-09	3.88E-10	2.66E-09	2.46E-09	7.04E-10	4.43E-10	2.79E-09
SSI_{FCT}	Conservative	1.62E-08	9.33E-09	4.80E-08	2.41E-09	6.14E-09	N/A	1.86E-11
	1st Order Decay	1.94E-04	8.90E-05	1.96E-04	1.81E-07	9.44E-05	5.92E-07	5.19E-06
	Linear Sorbing	8.81E-09	3.88E-10	2.66E-09	2.46E-09	7.01E-10	4.44E-10	2.79E-09

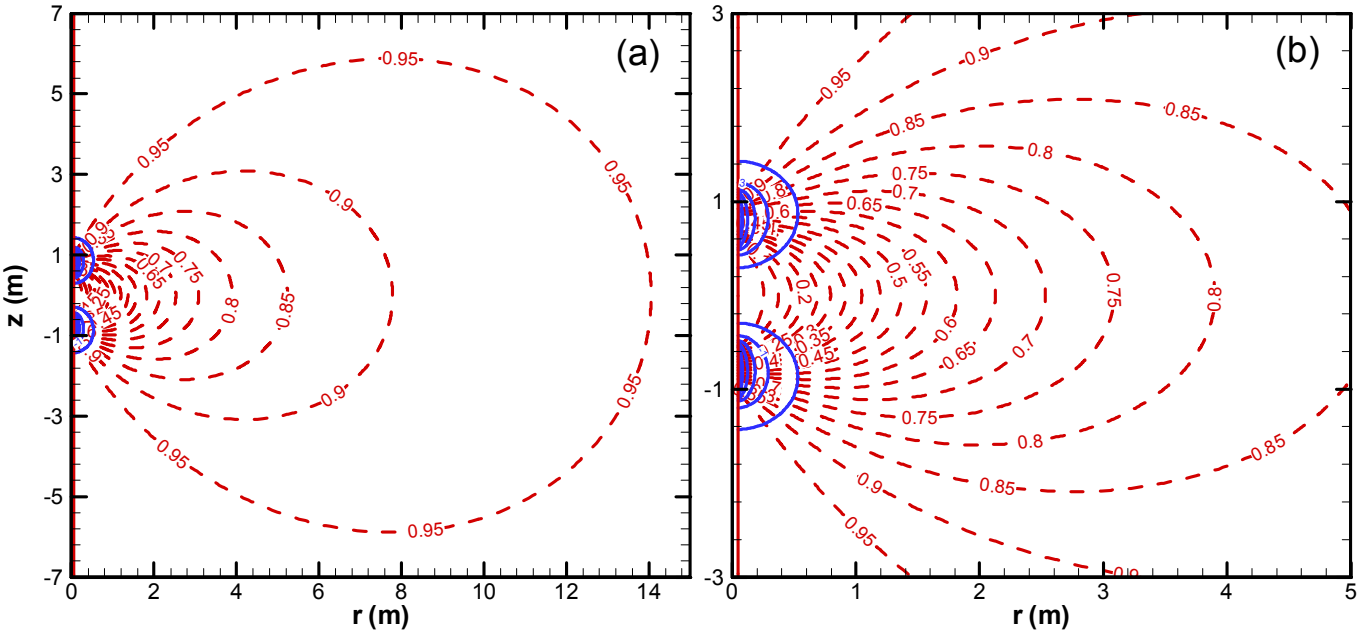

Figure 4.1: Streamfunction field (dashed) and hydraulic head field (solid) for the base case simulation. (a) Entire streamfunction field, (b) closer view of hydraulic head field. The injection chamber spans from 0.5 m ≤ z ≤ 1.1 m and the extraction chamber spans from -1.1 m ≤ z ≤ -0.5 m.

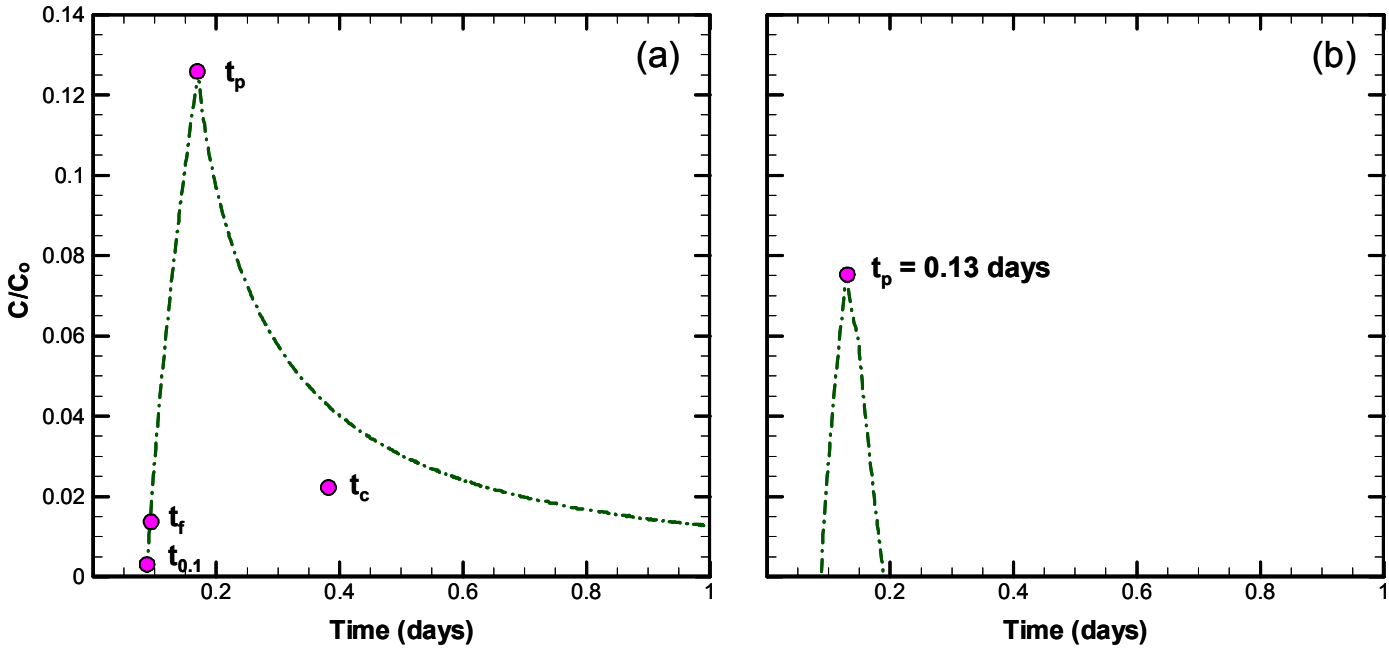

Figure 4.2: BTCs generated by the advective streamtube model using base case parameters and (a) 50% of the flow field, and (b) 10% of the flow field.

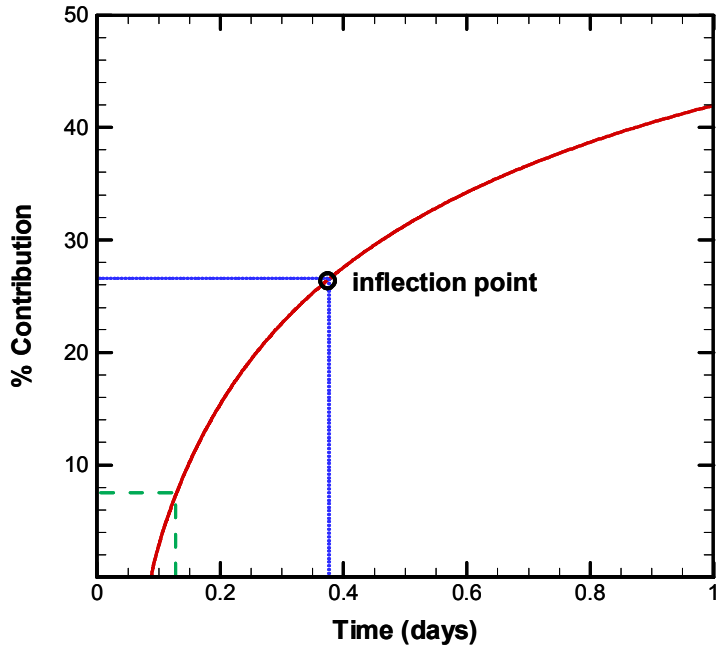

Figure 4.3: Advective arrival time distribution as determined by the advective streamtube model. The y-axis represents the percent of the injection chamber contributing to the extraction chamber by a given time. The dashed line illustrates the percent contribution at the time-to-peak, while the dotted line illustrates the inflection point of the arrival time distribution.

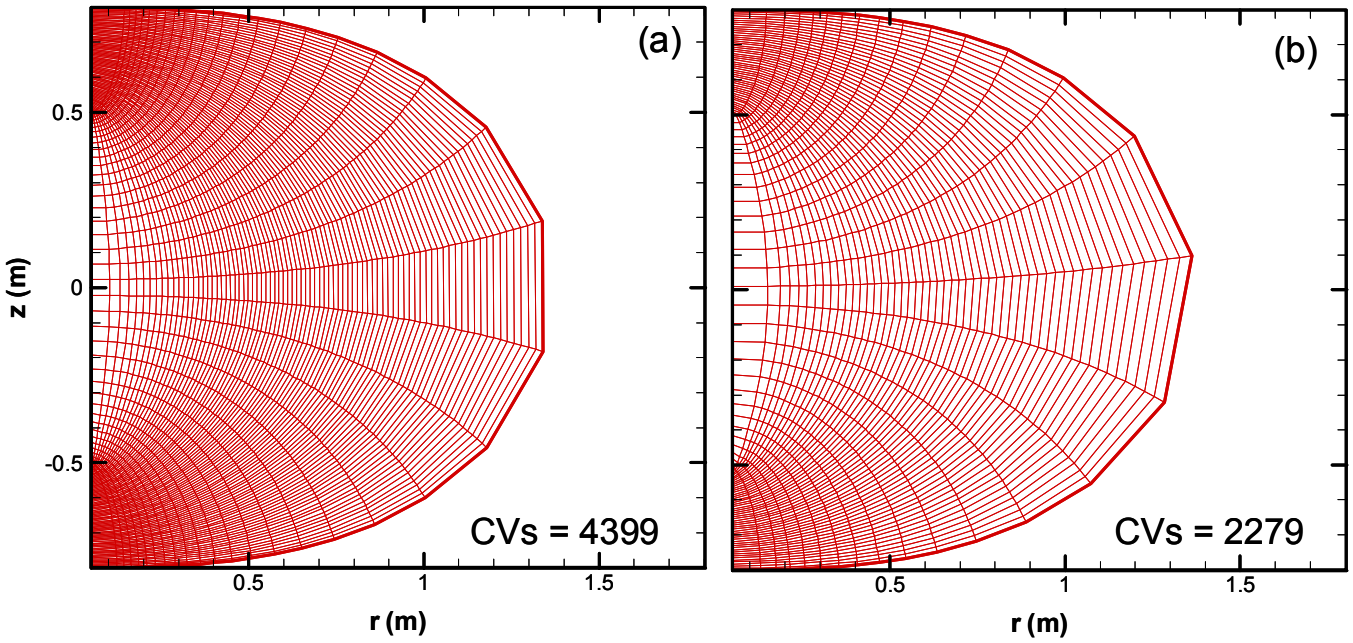

Figure 4.4: (a) Fine SOM, and (b) coarse SOM.

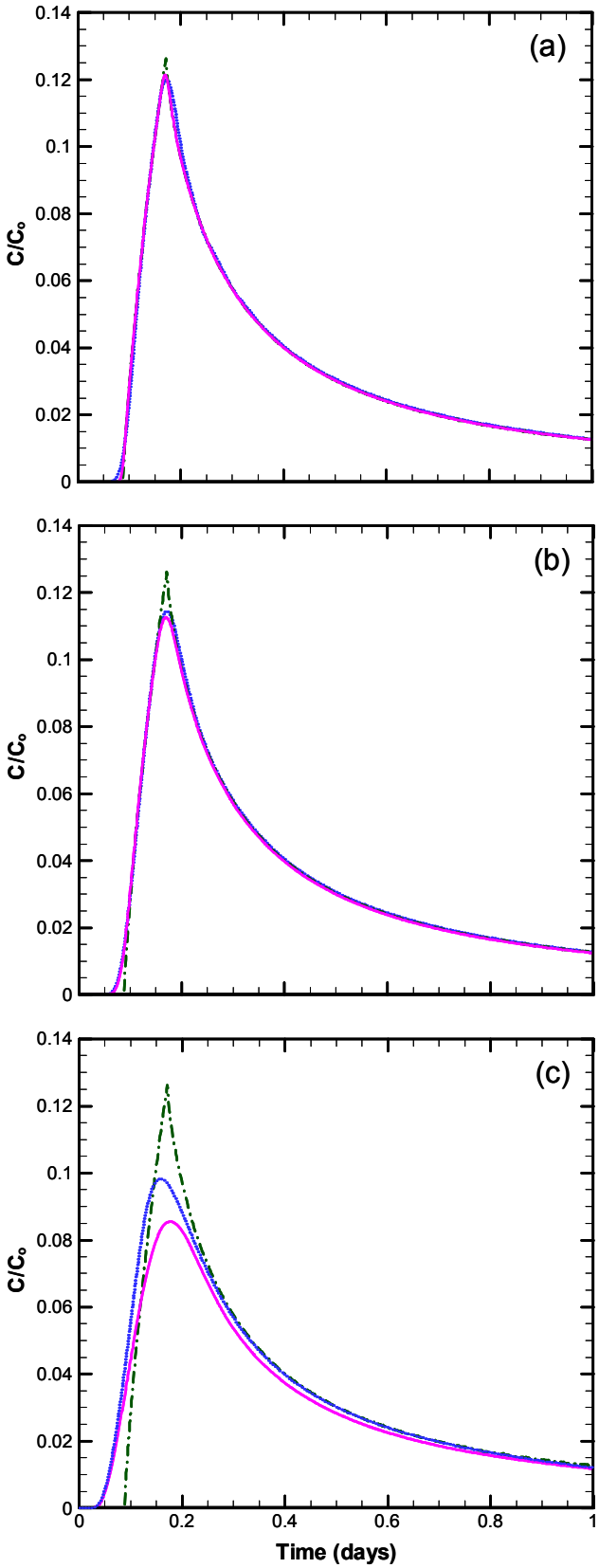

Figure 4.5: BTCs generated by the advective streamtube model (dotted-dash), the advective-dispersive streamtube model (solid), and the CRTM (dotted) using (a) α_L = 0.001 m, (b) α_L = 0.01 m, and (c) α_L = 0.1 m.

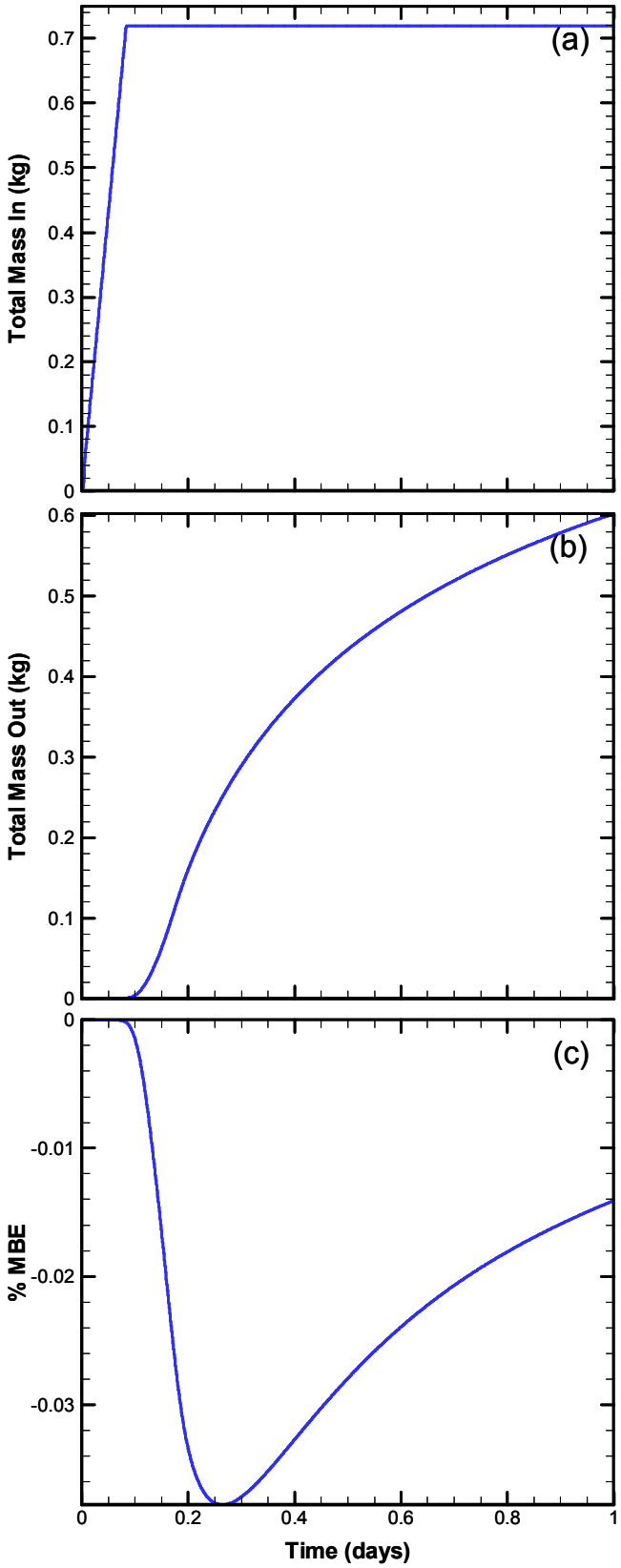

Figure 4.6: Temporal variations of (a) total mass in (kg), (b) total mass out (kg), and (c) % CMBE.

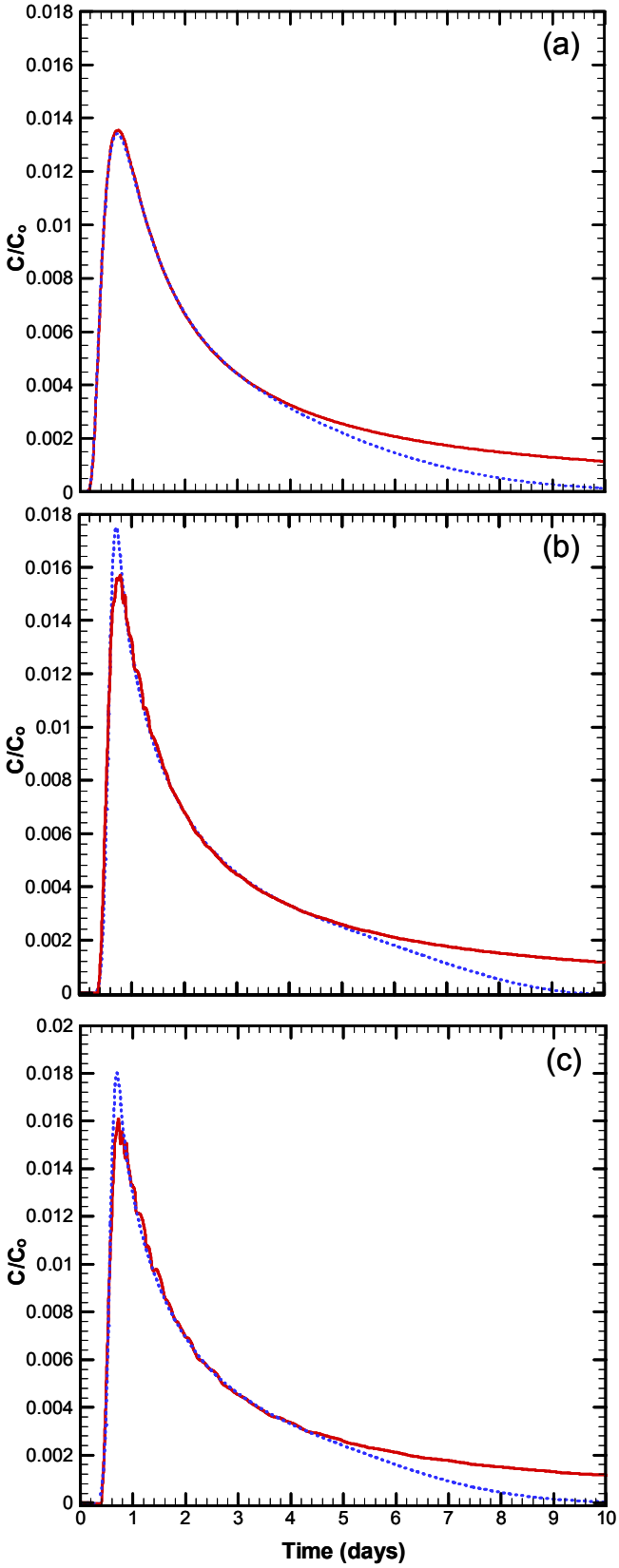

Figure 4.7: Conservative tracer BTCs from the CRTM (dotted) and MODFLOW/MT3DMS (solid) using (a) α_L = 0.1 m, (b) α_L = 0.01 m, and (c) α_L = 0.001 m.

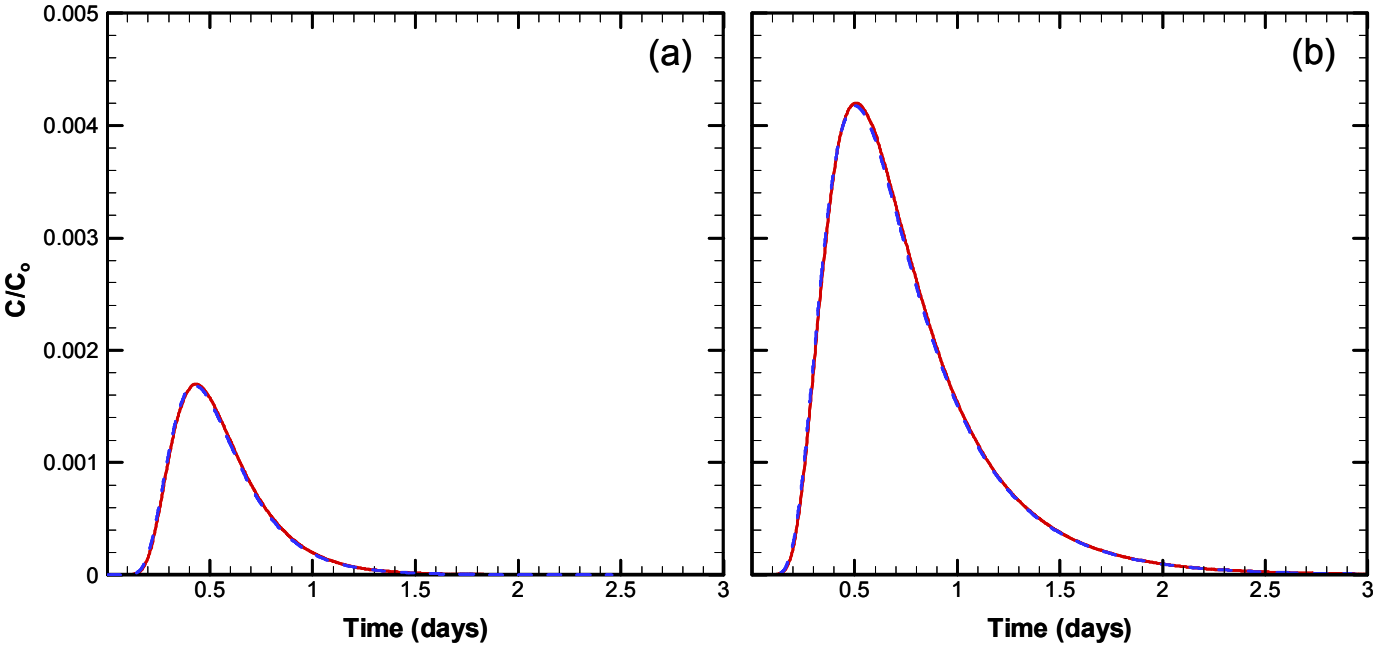

Figure 4.8: Decaying tracer BTC from the CRTM (dotted) and MODFLOW/MT3DMS (solid) using (a) $\lambda = 5x10^{-5}$ sec^{-1}, and (b) $\lambda = 2.5x10^{-5}$ sec^{-1}.

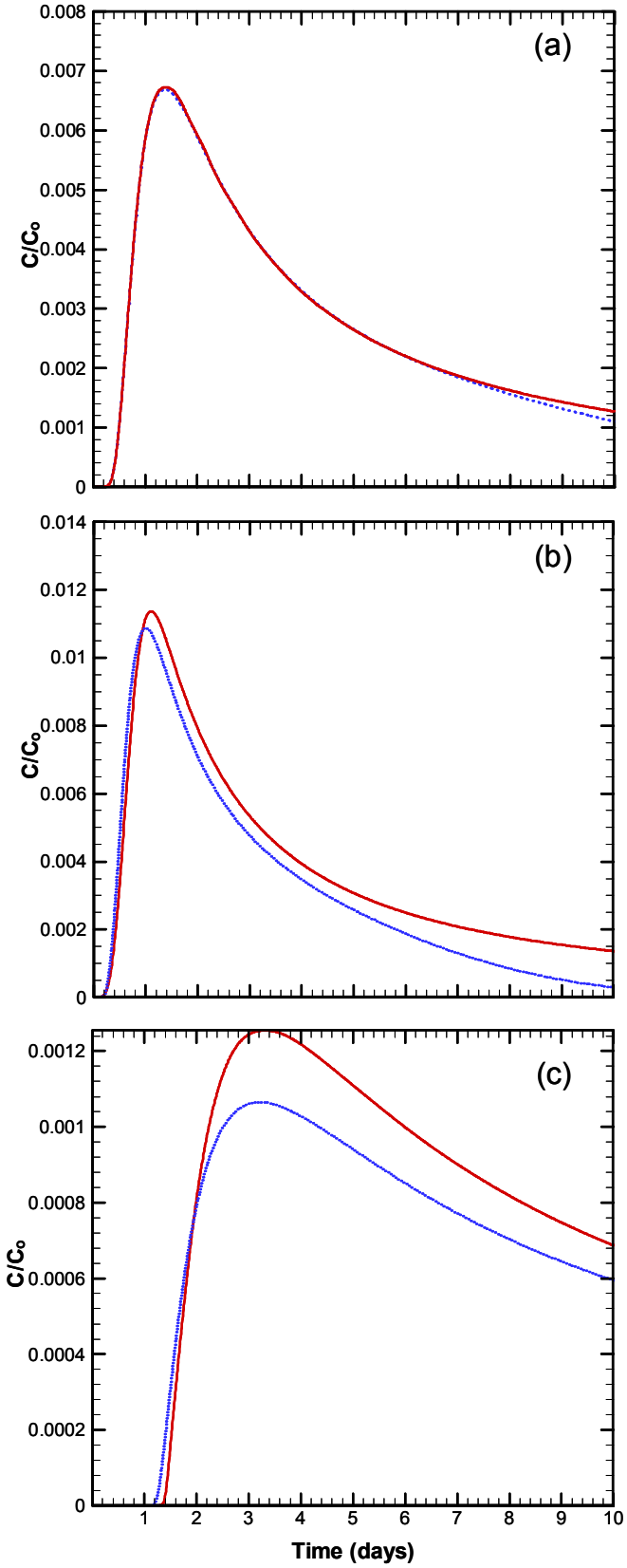

Figure 4.9: Sorbing tracer BTC from the CRTM (dotted) and MODFLOW/MT3DMS (solid) using (a) linear sorption isotherm with k_p = 1.8x10^{-4} m^3/kg, (b) Freundlich sorption isotherm with n = 1.5, and (c) Freundlich sorption isotherm with n = 0.5.

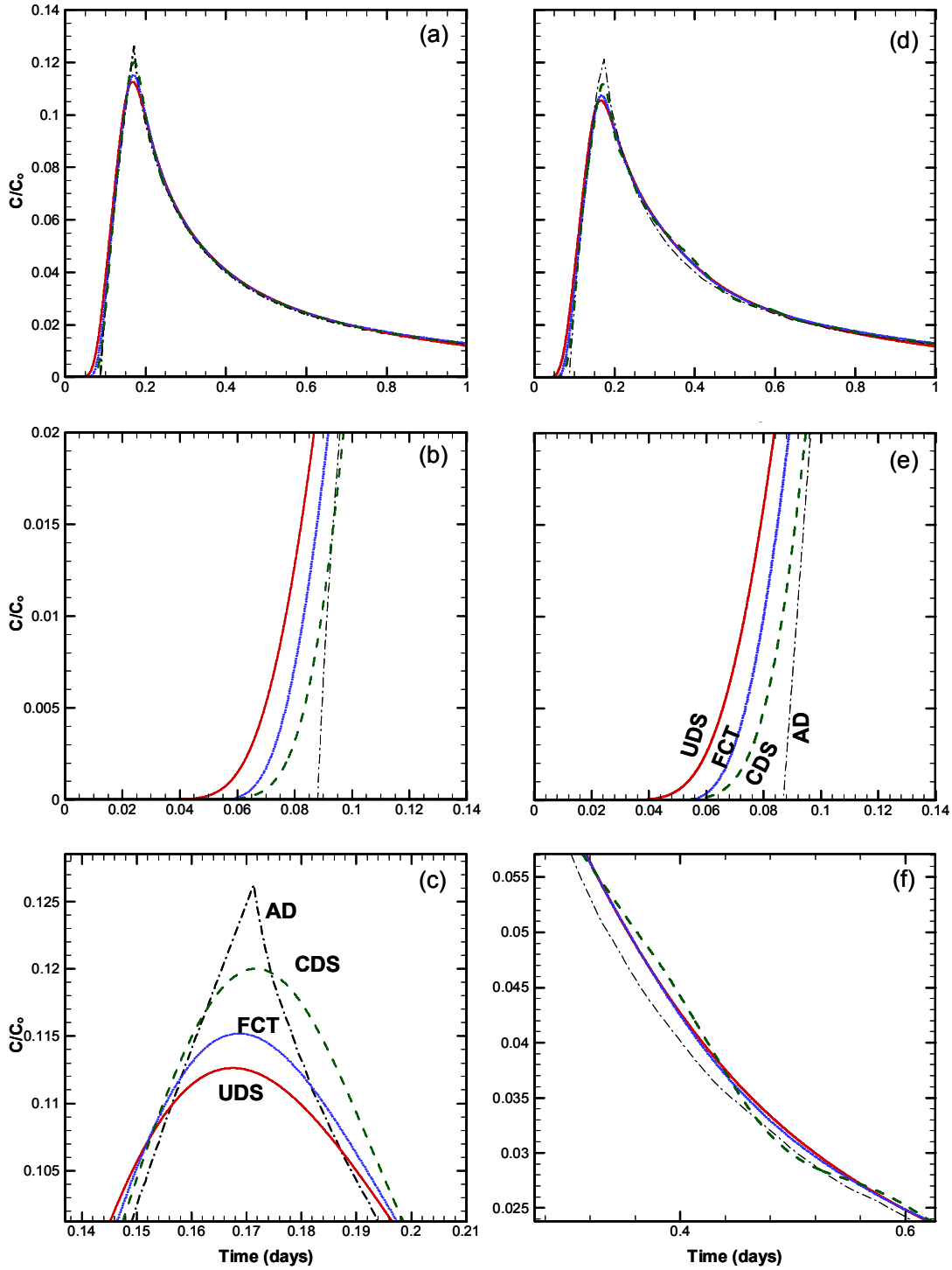

Figure 4.10: (a) BTCs obtained using the CDS (dashed), UDS (solid), FCT method (dotted), and the advective streamtube model (dash-dot) for base case parameters and the "fine mesh". Enlargement of (b) $t_{0.1}$, and (c) peak concentration. (d) BTCs for base case parameters and the "coarse mesh". Enlargement of (e) $t_{0.1}$, and (f) CDS oscillatory behaviour.

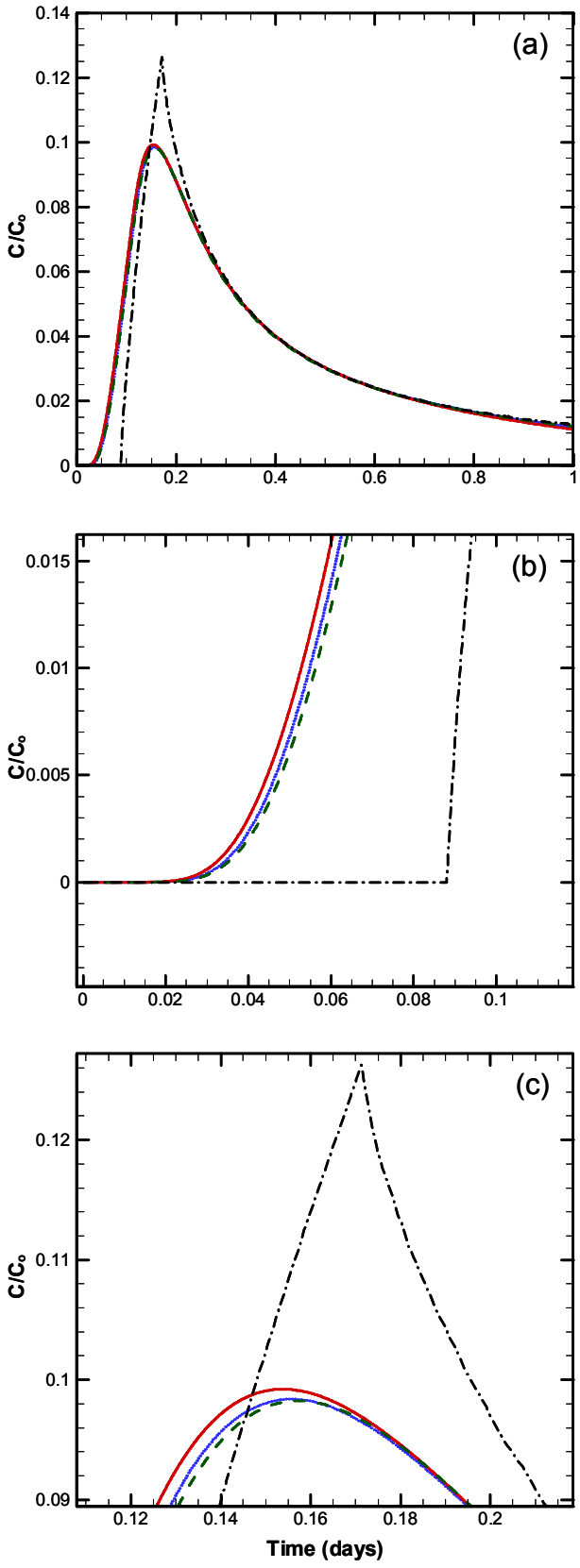

Figure 4.11: BTCs obtained for the CDS (dashed), UDS (solid), FCT method (dotted), and advective streamtube model (dash-dot) using α_L = 0.1 m. Closer view of (b) $t_{0.1}$, and (c) peak concentration.

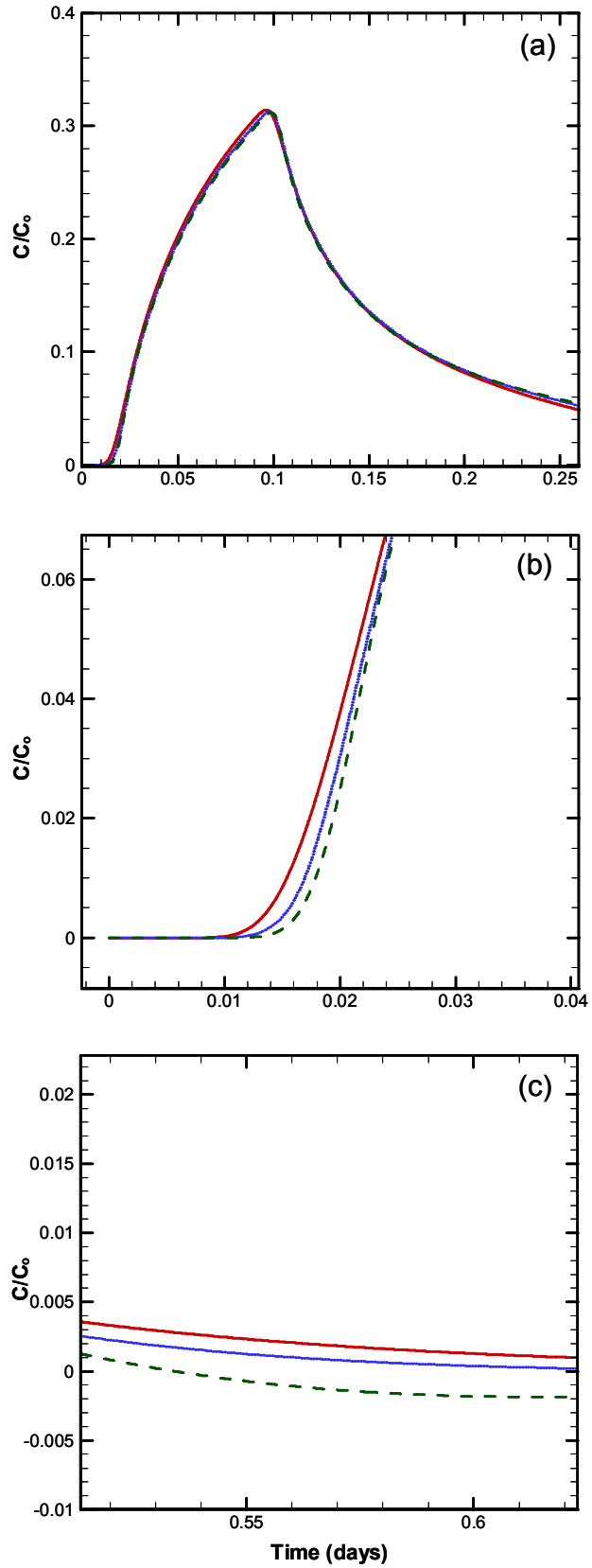

Figure 4.12: (a) BTCs obtained from the CDS (dashed), UDS (solid), and FCT method (dotted) using Q = 5.0x10^{-4} m^3/s. Enlargement of (b) $t_{0.1}$, and (c) CDS oscillatory behaviour.

CHAPTER 5 FIELD DESIGN CONSIDERATIONS

This chapter focuses on using the CRTM to aid in the design of a DFRTT biodegradation experiment applicable to the sandy aquifer at Canadian Forces Base (CFB) Borden. Laboratory and field estimation of organic contaminant biodegradation rates has proven to be a difficult task. Laboratory (microcosm or column) studies involve the removal of a sample (from the field) so that it may be evaluated within a controlled environment. These investigations typically yield useful information including, biodegradation rates, maximum utilization rates, and half-utilization coefficients; however, the sample may not be representative of *in situ* conditions (Bedient *et al.*, 1994). Difficulties arise with field-scale estimates because of a site's misunderstood transport processes (advection, dispersion, and sorption) (Bedient *et al.*, 1994). The DFRTT application at CFB Borden would provide a unique way of estimating degradation properties in a controlled manner at a well-documented location. The CRTM simulations conducted here, which is prior to the field study, will provide insight into the expected behaviour and outcomes and will be used to determine the duration and sampling frequency of the field experiment. Once the field experimentation is complete, the observed BTCs can be used to determine a set of site-specific Monod kinetics parameters using the CRTM.

An initial series of simulations are performed to determine the influence of dipole parameters on the BTC, and the zone of influence (determined by the tracers). The zone of influence is defined here as the volume of aquifer material travelled by the tracers which result in the observed BTC. These simulations were conducted using known hydrogeologic parameters of the Borden aquifer (Table 5.1) so that recommendations can be made for the design of a field experiment. The Borden aquifer is an unconfined, homogeneous sandy aquifer (well-sorted, fine to medium grained sand), approximately 9 m thick, underlain by a thick silty clay deposit (O'Hannesin,

1981; MacFarlane *et al.*, 1983; Sudicky, 1986; and Mackay *et al.*, 1986). The hydraulic conductivity ranges from $5x10^{-5}$ to $2x10^{-4}$ m/s (O'Hannesin, 1981; Sudicky, 1986) and the bulk density and porosity were estimated to be approximately 1810 kg/m^3 and 0.33 (Mackay *et al.*, 1986).

A second series of simulations were conducted to simulate the oxidation of toluene by aerobic bacteria present within the aquifer. The parameters of the substrate (toluene), oxygen (electron acceptor) and microbial population were changed and the simulated BTCs were used for determining the most ideal substrate and electron acceptor concentrations, injection length and flow rate for the field study. Based on the numerical results obtained from Chapter 4, the SSI_{FCT} (MBE ~ $1.0x10^{-5}$ %) will be used for all simulations performed in this chapter.

5.1 SELECTION OF DIPOLE TOOL PARAMETERS

The dipole length and half-chamber lengths were chosen for examination because of the potential impact that they may have on the zone of influence and the BTC tail. For these simulations, Borden was assumed to be a homogeneous aquifer; therefore, the effects of certain aquifer characteristics (anisotropic ratio, horizontal confining and conductive layers) on the zone of influence and BTC will not be examined. The dipole values used for this investigation were based on previous DFT field studies, as discussed in Section 4.1.1. The goal of this investigation was to maximize the zone of influence without generating an experimental duration exceeding 3 days. An experimental length of 3 days was desired to reduce travel time to Borden. The dipole tool base case parameter values, as well as flow rate, injection length, are given in Table 5.2. It should be mentioned that these initial simulations only consider the conservative tracer.

Bromide was used as the conservative tracer for these simulations. According to the American Public Heath Assoc. (1999) it has a method detection limit (MDL) of 0.05 mg/L determined through ion chromatography (IC), standard methods 4110. Since the bromide source concentration was 1.0 kg/m^3 than the BTC must contain a normalized concentration (C/C_o) of at least $5x10^{-5}$ or greater in order to be detected by the IC. Figure 5.1 displays the simulated bromide BTC using base case parametric values, while the advective arrival times and stream function fields are included in Appendix D. The resulting BTC indicates that the last detectable point occurs at approximately 2.6 days (Figure 5.1). The arrival time distribution indicates that approximately 55% of the flow field contributed to the BTC. Upon examination of the stream function field, it was determined that the zone of influence extended ~ 3.0 m radially and 1.65 m vertically. Assuming that this flow field is an ellipsoid, the volume of this zone of influence was estimated to be ~ 62.2 m^3 ($4\pi(3.0)(3.0)(1.65)/3$).

From the base case parameter values, the dipole length was increased to 1.5 m (almost twice the base case length) and decreased to 0.4 m. The resulting BTCs are shown in Figure 5.2, while the advective arrival times and stream function fields are included in Appendix D. Figure 5.2 demonstrates a strong influence that the dipole length has on the bromide BTC tail. When a dipole length of 0.4 m was employed, the last detectable point on the bromide BTC occurred at approximately 0.55 days (Figure 5.2(a)). The arrival time distribution indicates that approximately 60% of the flow field contributed to the BTC. Inspection of the stream function field determined that at 60% (of the flow field) the zone of influence extended ~ 2 m radially and 0.9 m vertically. The volume of this zone of influence was estimated to be ~ 15 m^3 and it should

be noted that ~ 60% of the injected bromide mass was recovered. The dipole length of 1.5 m never reached its last detectable point after 6 days of simulation (Figure 5.2(b)). Since this simulation time exceeds our limited experimental duration (3 days), it was decided that the flow field would be evaluated at 6 days (to reduce computational run-time). Examination of the arrival time distribution determined that 40% of the flow field contributed to the bromide BTC at 6 days. Inspection of the stream function field indicated that the zone of influence extended ~ 4 m radially and 3 m vertically, which estimates the volume of this zone of influence to be ~ 201 m^3. Although the largest dipole length (1.5 m) generated the biggest zone of influence, it never achieved its last detectable BTC point. The smallest dipole length (0.4 m) was able to achieve this BTC point; however, it demonstrated the smallest zone of influence. Since a considerable aquifer volume is preferable but a long BTC tail is undesirable, the resulting analysis indicates that the base case dipole length (0.8 m) is the ideal choice for this field experiment.

Figure 5.3 displays the simulated bromide BTCs when the half-chamber lengths are increased from 0.3 to 0.45 m and then decreased to 0.15 m. The advective arrival time distributions and stream function fields are included in Appendix D. When the half-chamber length is increased, the distance between the injection and extraction chambers decreases, resulting in an early peak arrival time (Table 5.3). The latest detectable point on the bromide BTC tail was achieved in ~ 2.6 days (for all three half-chamber lengths). The arrival time distribution plots for Δ = 0.15 m and 0.45 m indicate that approximately 55% of the flow field (for both half-chamber lengths) contributed to the BTC generation, signifying minimal change from the base case investigation. Inspection of the stream function field for the 0.45 m half-chamber length indicates that the zone of influence (under this flow field contribution) extends ~ 3.0 m radially and 1.6 m vertically; the

aquifer volume of this zone was determined to be ~ 60.3 m^3. The zone of influence for the 0.15 m chamber length was found to extend ~ 3.0 m radially and 1.7 m vertically, yielding an aquifer volume of ~ 64.1 m^3.

As stated previously, the objective of this investigation was to recommend a dipole configuration that would yield a considerable zone of influence (and aquifer volume) within a reasonable timeframe (3 days). It was determined that alterations made to the dipole length had a significant impact on both the detectable bromide BTC tail and the zone of influence, while alterations made to the half-chamber lengths demonstrated minimal change (in comparison to the base case). Since the largest dipole length (1.5 m) never achieved the last detectable BTC point (after a 6 day simulation), and the shortest dipole length (0.4 m) had the smallest zone of influence, then it was recommended that a dipole length of 0.8 m be employed, which is a reasonable medium between the two. Although the varying half-chamber lengths illustrated the same detectable bromide BTC tail, the largest half-chamber length used a smaller volume of aquifer. Based on these considerations, it is recommended that a smaller half-chamber length be used (0.15 or 0.30 m). It should be noted that the recommended dipole configuration is for a conservative tracer test only. Once reactive tracers are considered, the experimental duration will have to be modified in order to accommodate the detection limits of decaying and sorbing tracers (which may reach non-detectable limits before or after the limits of a conservative tracer).

5.2 MONOD KINETICS

The dual-Monod equations (outlined in Section 3.3.1) are used to simulate the oxidation of toluene by aerobic bacteria present within the CFB Borden aquifer. The purpose of generating

these simulations is to determine ideal experimental parametric values that will yield detectable field BTC data for the substrate (toluene) and electron acceptor (dissolved oxygen). This will be established by performing a sensitivity analysis on specific experimental design parameters (substrate and electron acceptor concentration, flow rate, injection length); the results will be used to aid in the design of a field experiment. A sensitivity analysis will also be performed on certain Monod parameters in order to gain perception of their influence over substrate degradation and electron acceptor utilization. After the field experiment has been designed and implemented, the resulting CRTM BTCs will be correlated with those obtained from the field so that Monod parameters (half-utilization constants, and the maximum utilization rate of toluene) can be determined; this is important because it helps us to understand an aquifer's biodegradation potential, which is imperative for designing an appropriate site-specific remedial strategy. The field experiment (and CRTM simulations) will include the injection of toluene and dissolved oxygen (both species are mobile) to interact with aerobic bacteria (an immobile species) present within the aquifer. A conservative tracer (bromide) will also be injected so that the resulting substrate and electron acceptor BTCs can be compared to a non-reactive tracer. The field effluent should be monitored until it is no longer detectable (approximately 3 days or less) and the frequency of sampling events (to observe changes in effluent concentrations) will be recommended once the simulations have been achieved and analyzed. It is recommended that toluene (MDL = 0.12 μg/L) be measured using EPA analytical method 524.2 (gas chromatography/mass spectrometry (GC/MS)) (USEPA, 1991), while dissolved oxygen be measured using a dissolved oxygen probe (measurement range: 0 to 15 mg/L). Although a comparison of the conservative tracer to the substrate and electron acceptor BTCs was not conducted during this sensitivity analysis, it is recommended that the conservative tracer be

measured during the field experiment (Section 5.1) so that the substrate and electron acceptor can be compared to a non-reactive tracer.

The initial parametric values used for these biodegradation simulations were the same values used by MacQuarrie *et al.* (1990) for laboratory column experiments, to describe the behaviour of toluene, dissolved oxygen and an aerobic microbial population. Although aquifer conditions determined from a laboratory column experiment are not entirely representative of *in situ* conditions, it is believed that these values are a good starting point for this investigation. Experimental design parameters to be explored in this investigation are included in Table 5.4, while aquifer parameters that are to be characterized after DFRTT implementation are included in Table 5.5. It is hypothesized that microbial growth will thrive when the substrate concentration and injection length are increased since microbial food becomes more abundant. Consequently, as the microbial population grows electron acceptor utilization should also increase since it is required for oxidation of the substrate. It is believed that the microbial population will flourish when the maximum utilization rate is increased (since the potential for microbial growth increases) and when the substrate half-constant is decreased (since microbial growth becomes independent of the food supply). As the microbial population expands, substrate degradation and electron acceptor utilization should increase. The following simulations were run for a period of 1 day in order to reduce computational effort; this should not affect the overall conclusions of this study.

Figure 5.4 illustrates the resulting BTCs for the electron acceptor (Figure 5.4(a)) and substrate (Figure 5.4(b)) when the substrate concentration is increased from 0.4 to 4.0 mg/L and then

decreased to 0.04 mg/L. When the substrate concentration is increased the abundance of food also increases, providing more nourishment to the microbial concentration. As a greater supply of food becomes available to the microbes, their population grows and requires more electron acceptors for substrate oxidation (i.e., degradation). Figure 5.4(a) also illustrates that when the smaller substrate concentration was employed, the electron acceptor BTC was almost indistinguishable from the base case BTC because the limited food supply did not stimulate microbial growth, which resulted in minimal electron acceptor utilization. Figure 5.4(b) represents the BTCs for the substrate when its concentration was altered. As expected, the BTC peak for the increased substrate concentration was greater than the base case (Figure 5.4(b), Table 5.6), while the BTC peak for the decreased substrate concentration was the smallest of all three BTCs. It should be noted that after the simulations were generated, it became evident that the largest substrate concentration simulation was the only one to produce a detectable BTC. Assuming that the EPA analytical method 524.2 (GC/MS) is used to measure toluene (for the field experiment), then the normalized concentration ratio "cut-off" boundary for an injection concentration of 4 mg/L is approximately $3x10^{-5}$ (Figure 5.4(b)); therefore, any concentration ratio greater than this value is detectable by the GC/MS. No cut-off boundaries were included for the other BTCs because they fell far below detectable levels (this is also the case for dissolved oxygen). As expected, the largest substrate concentration had the largest microbial population growth ~ 3%, followed by the base case ~ 0.6%, while the smallest substrate concentration had a microbe population growth of ~ 0.1%. Figure 5.4(c) and (d) illustrate the resulting electron acceptor and substrate BTCs when the electron acceptor concentration is decreased from 6.0 to 0.6 mg/L. The resulting substrate BTCs (Figure 5.4(d)) illustrated that degradation was essentially the same for both electron acceptor concentrations. Since an aquifer is said to be

aerobic if the dissolved oxygen concentration is greater than 2 mg/L (McAllister and Chiang, 1994), than it was not surprising that the reduced electron acceptor concentration yielded minimal microbial growth (~ 0.43%). Again, no measurable cut-off boundaries were included for the electron acceptor or substrate curves because they were short of their measurable levels. The resulting simulations demonstrated that substrate concentration has a significant impact on microbial growth and electron acceptor utilization; however, it also exhibited that the electron acceptor concentration had minimal influence on substrate degradation and microbial growth. If this experiment were conducted in the field, it would be difficult to back-calculate Monod rates since the resulting substrate and electron acceptor BTCs fell far below detectable standards (with the exception of $C_{substrate}$ = 4.0 mg/L). The importance of injecting a large substrate concentration was demonstrated so that, (1) the substrate reaches detectable limits, and (2) the electron acceptor BTCs can be distinguished from one another; this allows for the determination of specific aquifer characteristics. Since it is unlikely that the chosen electron acceptor will ever reach detectable levels, it is acceptable to utilize the CRTM for simulating electron acceptor utilization.

Figure 5.5 shows the electron acceptor and substrate BTCs when the total initial microbial concentration was increased from 0.23 to 2.3 mg/L and then decreased to 0.023 mg/L, which is an acceptable microbial concentration range for a contaminated site (Ghiorse and Wilson, 1988). Figure 5.5(a) illustrates the significant impact that the total initial microbial concentration has on the electron acceptor concentration. Compared to the base case, when the total microbial concentration was increased the resulting BTC displays that the electron acceptor underwent greater utilization since the larger (microbe) population required more electron acceptor mass for

substrate degradation. The larger microbe population also demanded more nourishment, therefore, the substrate also underwent greater degradation (than the base case) (Figure 5.5(b)). As expected, when the total initial microbial concentration was decreased, the resulting BTC demonstrates that the electron acceptor underwent less utilization than the base case (Figure 5.5(a)), which resulted in less substrate degradation (Figure 5.5(b)). The microbial growth demonstrated a proportional relationship to the total initial microbial concentration; microbial growth was more substantial when the total initial microbial concentration increased (~ 5.7%) and was less considerable when the initial microbial concentration was decreased (~ 0.07%). Again, if this experiment were conducted in the field it would be impossible to back-calculate Monod rates since the resulting substrate and electron acceptor BTCs were far below detectable standards. These simulations demonstrate the importance of utilizing a large substrate concentration, and the necessity for preliminary (model) testing to aid in experimental field design.

Figure 5.6 shows the resulting electron acceptor and substrate BTCs when the substrate and electron acceptor injection lengths were increased from 2 to 24 hr and then decreased to 1 hr. The 1 day injection duration was chosen because we wanted to view the resulting BTCs for an extreme injection length. Since the injection lengths of the substrate and electron acceptor were altered at the same time, it was difficult to assess the quantity of electron acceptor utilized and the substrate that was degraded, in comparison to the base case (Figure 5.6(a) and (b)). However, examination of the microbial population growth indicates that when the injection length was increased the population grew by ~ 8.2% and when the injection length was decreased the population only grew by ~ 0.32%. The population growth was greatest for a longer injection

length because there was more substrate mass available for microbial nourishment, resulting in microbial growth. Therefore, it can be assumed that substrate degradation and electron acceptor utilization was greatest with the longer injection length. Again, no measurable cut-off boundary was included on either of the BTCs since all of the BTCs fell below measurable standards; this alludes to the importance of using a large substrate concentration. The resulting simulations demonstrated that a long injection period has a substantial impact on microbial growth, substrate degradation, and electron acceptor utilization.

Figure 5.7 shows the simulated BTCs when the flow rate is increased from $1x10^{-4}$ m^3/s to $5x10^{-4}$ m^3/s and then decreased to $1x10^{-5}$ m^3/s. Intuitively, it was presumed that substrate degradation would be significant for a higher flow rate (in comparison to the base case or lower flow rate) since a higher flow rate is able to supply more nourishment to the microbial population. However, examination of the microbial population growth percentages indicated that the larger flow rate contained the smallest percentage ~ 0.48%, while the smaller flow rate had the largest percentage ~ 0.68%. It is likely that the higher flow rate swept the substrate and electron acceptor quickly through the aquifer material, in effect, not allowing enough contact time for the microbial population to oxidize the substrate; this resulted in poor microbial growth and substrate degradation. Although the lower flow rate did allow a longer contact time, there was not enough substrate mass to nourish the microbial population, resulting in poor microbial growth and substrate degradation. With respect to a field experiment, it is important that the selected flow rate is neither too high nor too low. A low flow rate will increase the experimental length (thus, increasing the cost of the experiment), while a high flow rate will not allow enough contact time between the microbes and the substrate.

The maximum utilization rate for the substrate was increased from $5.7x10^{-6}$ to $5.7x10^{-5}$ sec^{-1} and then decreased to $5.7x10^{-7}$ sec^{-1}. The simulated BTCs for the electron acceptor and substrate are shown in Figure 5.8. When the substrate utilization rate increases, the potential for microbial growth also increases (Bedient *et al.*, 1994). Examination of the microbial population indicated that the increased utilization rate yielded ~ 5.9% growth, while the base case yielded ~ 0.6% growth; therefore, it was not surprising that the electron acceptor utilization (Figure 5.8(a)) and substrate degradation (Figure 5.8(b)) also increased (compared to the base case). Conversely, when the maximum utilization rate was decreased, microbial growth decreased (~0.06%) along with electron acceptor utilization (Figure 5.8(a)) and substrate degradation (Figure 5.8(b)). Measurable cut-off boundaries are absent since all of the BTCs fell below measurable standards. Again, if this experiment were conducted in the field, it would be necessary to utilize a large substrate concentration so that Monod rates can be back-calculated. Difficulties may arise when trying to estimate a small maximum utilization rate since the substrate and electron acceptor BTCs for a maximum utilization rate of $5.7x10^{-7}$ sec^{-1} are similar to the BTCs of the base case ($5.7x10^{-6}$ sec^{-1}); therefore, it is suggested that a sensitivity analysis be performed once the parameter has been estimated.

Figure 5.9 shows the resulting BTCs when the half-utilization constants for the substrate and electron acceptor were altered. Microbial growth is heavily dependent on the half-utilization constant and substrate concentrations. The Monod kinetics equations indicate that if the substrate half-utilization constant is larger than the substrate concentration, microbial growth is dependent on food availability; however if the substrate concentration is greater than the substrate half-

utilization constant, than microbial growth is independent of the food supply. When the substrate half-utilization constant was increased to 6.5 mg/L, microbial growth became dependent on the food supply. Inspection of the microbial population indicated a growth of ~ 0.4% (Table 5.6), which is less than the base case growth (~ 0.6%). Figure 5.9(a) and (b) show that the electron acceptor was not utilized any more than the base case, and substrate degradation was less the base case; this is attributable to the limited food supply and in effect the lack of microbial growth. When the substrate half-utilization constant was decreased to 6.5×10^{-2} mg/L microbial growth became independent of the food supply. Inspection of the microbial population indicated a growth of ~2.6% (Table 5.6). The resulting BTCs showed greater electron acceptor utilization (Figure 5.9(a)) and substrate degradation (Figure 5.9(b)) compared to the base case. This is attributable to the larger microbe population. When the electron acceptor half-utilization constant was altered, there appeared to be no significant changes to the resulting electron acceptor (Figure 5.9(c)) or substrate (Figure 5.9(d)) BTCs. Inspection of the microbe population indicated that ~ 0.4% and ~ 0.7% growth occurred when the electron acceptor half-utilization constant was increased and decreased, respectively. Again, difficulties may arise when trying to estimate the half-utilization constant for the substrate and electron acceptor since the resulting BTCs are very similar. It is suggested that a sensitivity analysis be performed once the parameter has been estimated to ensure that a reasonable value has been selected.

Unfortunately, the chosen base case parametric values for both the experimental design and aquifer properties resulted in undetectable substrate and electron acceptor BTCs. However, there was one particular simulation in which the substrate BTC was almost entirely detectable; this was the $C_{substrate}$ = 4.0 mg/L simulation. Although the long injection period and high flow rate

simulations yielded BTCs that were almost measurable, they could never be used in our field experiment since it would take over 3 days to achieve BTC completion. It is advised that a large substrate concentration be utilized (at least 4.0 mg/L or greater) so that the field experiment will yield a measurable BTC. It is important that the dissolved oxygen concentration also be large so that it is able to provide the microbial population with enough electron acceptors for substrate degradation; however, it is not mandatory that the dissolved oxygen reach measurable standards within the field since the CRTM can be used to simulate electron acceptor utilization. Therefore, based on the results from this investigation, it is recommended that: (i) sampling events occur once every 1 to 2 hours (if possible) so that the changes in effluent concentration can be documented accurately; (ii) dipole parameters from Section 5.1 with a standard 2" well be employed; (iii) a large substrate concentration be utilized (> 4.0 mg/L); (iv) a flow rate of $1x10^{-4}$ m^3/s be used; and (v) an injection duration of 2 hours be applied. It may be argued that performing a sensitivity analysis was a weak design approach. This may be true since the recommended injection duration and flow rate are based on a low substrate concentration (yielding undetectable substrate BTCs); however, it is believed that the resulting conclusions (i.e., the significant impact that the substrate concentration has on obtaining a detectable BTC) would not have changed regardless of the employed approach. As long as the field substrate BTC is measurable, then Monod kinetics can be obtained after a field and CRTM BTC comparison.

Table 5.1: Hydrogeologic conditions of CFB Borden.

Parameter	Value	Source
θ	0.33	Mackay *et al.* (1986)
ρ_b (kg/m^3)	1810	Mackay *et al.* (1986)
K_r (m/s)	1.00E-05	Sudicky (1986)
a^2	1.0	Mackay *et al.* (1986)
α_L (m)	0.1	0.1 x base case dipole length

Table 5.2: Base case parameter values.

Parameter	Value
Tracer	Conservative
Initial Concn. of Tracer (kg/m^3)	1.0
Injection Length (hr)	2.0
Test Period (day)	1.0
Q (m^3/s)	1.00E-04
L (m)	0.8
Δ (m)	0.3
r_w (m)	0.05

Table 5.3: Resulting BTC characteristics.

Parameter	BTC Entry Time (days)	Time to Peak (days)	Arrival Time of Tracer Front (days)	Peak Concentration	Last Detectable BTC Point (days)
Base Case	1.49E-02	1.61E-01	4.50E-02	9.90E-02	2.61E+00
L = 0.4 m	1.01E-03	7.99E-02	2.00E-03	3.85E-01	5.51E-01
L = 1.5 m	2.22E-01	9.41E-01	3.58E-01	1.65E-02	6^+
Δ = 0.15 m	4.01E-02	1.81E-01	6.00E-02	9.50E-02	2.61E+00
Δ = 0.45 m	1.02E-02	1.25E-01	2.60E-02	1.11E-01	2.61E+00

Table 5.4: Experimental design parameters.

Parameter	Base Case Value	Source
Concentration of Toluene (mg/L)	4.00E-01	MacQuarrie *et al.* (1990)
Concentration of Oxygen (mg/L)	6.00E+00	MacQuarrie *et al.* (1990)
Injection Length (hr) - continuous source	2.0	
Q (m^3/s)	1.00E-04	
L (m)	0.8	
Δ (m)	0.3	
r_w (m)	0.05	

Table 5.5: Assumed Monod kinetic parameters for the Borden aquifer.

Parameter	Value	Source
Microbial Concentration (mg/L of Aquifer Material)	2.30E-01	MacQuarrie *et al.* (1990)
Retardation Factor of Oxygen	1.0	MacQuarrie *et al.* (1990)
Retardation Factor of Toluene	1.4	MacQuarrie *et al.* (1990)
Half-Utilization Constant of Toluene (mg/L)	6.54E-01	MacQuarrie *et al.* (1990)
Half-Utilization Constant of Oxygen (mg/L)	1.00E-01	MacQuarrie *et al.* (1990)
Microbial Yield	4.26E-01	MacQuarrie *et al.* (1990)
Oxygen to Toluene Mass Ratio	3.13	MacQuarrie *et al.* (1990)
Maximum Utilization Rate of Toluene (sec^{-1})	5.70E-06	MacQuarrie *et al.* (1990)
First-Order Microbial Decay Coefficient (sec^{-1})	0.0	MacQuarrie *et al.* (1990)

Table 5.6: BTC characteristics for an electron acceptor and substrate after alterations were made to Monod parameters and variables.

Curve	Parameter Altered	BTC Entry Time (days)	Time to Peak (days)	Arrival Time of Tracer Front (days)	Peak Concentration	Microbial Growth %
Substrate	Base Case	2.11E-02	1.85E-01	7.51E-02	2.81E-05	6.55E-01
	$C_{substrate} = 4.0x10^{-3}$ kg/m^3	2.11E-02	1.85E-01	5.55E-02	2.88E-04	3.04E+00
	$C_{substrate} = 4.0x10^{-5}$ kg/m^3	2.11E-02	1.65E-01	5.21E-02	4.21E-05	9.87E-02
	$C_{electron\ acceptor} = 6x10^{-4}$ kg/m^3	2.11E-02	1.85E-01	7.51E-02	2.81E-05	4.33E-01
	$M_t = 2.3x10^{-3}$ kg/m^3	2.11E-02	1.71E-01	5.11E-02	2.55E-05	5.72E+00
	$M_t = 2.3x10^{-5}$ kg/m^3	2.11E-02	1.85E-01	7.51E-02	2.91E-05	6.65E-02
	Injection Length = 24 hr	2.11E-02	1.21E+00	9.91E-02	1.51E-04	8.20E+00
	Injection Length = 1 hr	2.11E-02	1.55E-01	5.55E-02	1.47E-05	3.25E-01
	$k_{max} = 5.7x10^{-5}$ sec^{-1}	2.11E-02	1.85E-01	5.51E-02	2.51E-05	5.89E+00
	$k_{max} = 5.7x10^{-7}$ sec^{-1}	2.11E-02	1.85E-01	7.51E-02	2.91E-05	6.63E-02
	$K_{sb} = 6.5x10^{-3}$ kg/m^3	2.11E-02	1.85E-01	7.51E-02	2.89E-05	8.21E-02
	$K_{sb} = 6.5x10^{-5}$ kg/m^3	2.11E-02	1.85E-01	5.51E-02	2.75E-05	2.63E+00
	$K_A = 1x10^{-3}$ kg/m^3	2.11E-02	1.85E-01	7.51E-02	2.81E-05	4.37E-01
	$K_A = 1x10^{-5}$ kg/m^3	2.11E-02	1.85E-01	7.51E-02	2.81E-05	7.24E-01
	$Q = 5x10^{-4}$ m^3/s	2.11E-02	8.91E-02	2.12E-02	2.35E-03	4.88E-01
	$Q = 1x10^{-5}$ m^3/s	2.11E-01	1.10E+00	3.11E-01	6.01E-05	6.88E-01
Electron Acceptor	Base Case	2.11E-02	1.52E-01	4.15E-02	5.91E-04	6.55E-01
	$C_{substrate} = 4.0x10^{-3}$ kg/m^3	2.11E-02	1.53E-01	4.15E-02	5.85E-04	3.04E+00
	$C_{substrate} = 4.0x10^{-5}$ kg/m^3	2.11E-02	1.51E-01	4.71E-02	2.31E-04	9.87E-02
	$C_{electron\ acceptor} = 6x10^{-4}$ kg/m^3	2.11E-02	1.55E-01	4.56E-02	6.23E-05	4.33E-01
	$M_t = 2.3x10^{-3}$ kg/m^3	2.11E-02	1.55E-01	4.15E-02	5.78E-04	5.72E+00
	$M_t = 2.3x10^{-5}$ kg/m^3	2.11E-02	1.52E-01	4.15E-02	5.91E-04	6.65E-02
	Injection Length = 24 hr	2.11E-02	1.03E+00	5.51E-01	2.58E-03	8.20E+00
	Injection Length = 1 hr	2.11E-02	1.25E-01	2.21E-01	3.21E-04	3.25E-01
	$k_{max} = 5.7x10^{-5}$ sec^{-1}	2.11E-02	1.51E-01	4.15E-02	5.78E-04	5.89E+00
	$k_{max} = 5.7x10^{-7}$ sec^{-1}	2.11E-02	1.52E-01	4.15E-02	5.91E-04	6.63E-02
	$K_{sb} = 6.5x10^{-3}$ kg/m^3	2.11E-02	1.52E-01	4.15E-02	5.91E-04	8.21E-02
	$K_{sb} = 6.5x10^{-5}$ kg/m^3	2.11E-02	1.52E-01	4.15E-02	5.91E-04	2.63E+00
	$K_A = 1x10^{-3}$ kg/m^3	2.11E-02	1.52E-01	4.15E-02	5.91E-04	4.37E-01
	$K_A = 1x10^{-5}$ kg/m^3	2.11E-02	1.52E-01	4.15E-02	5.91E-04	7.24E-01
	$Q = 5x10^{-4}$ m^3/s	2.11E-02	7.51E-02	2.12E-02	1.44E-04	4.88E-01
	$Q = 1x10^{-5}$ m^3/s	2.11E-01	1.57E+00	3.11E-01	3.11E-06	6.88E-01

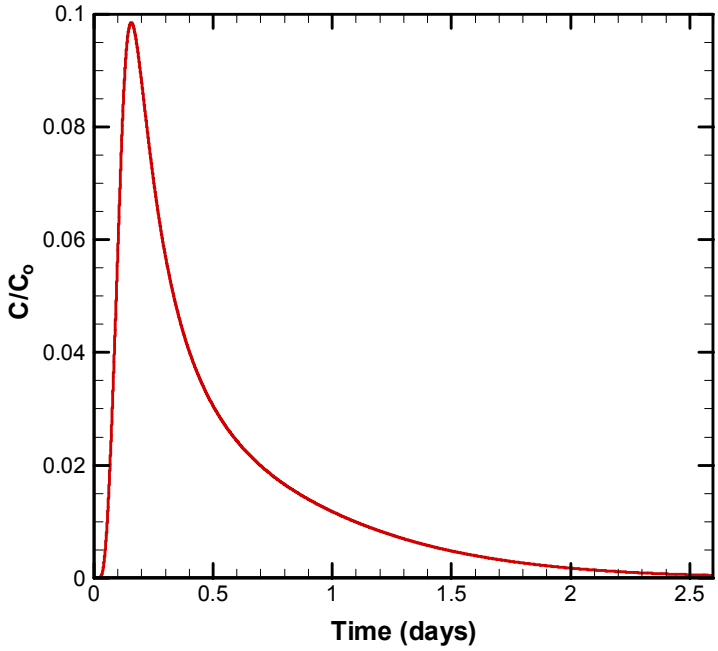

Figure 5.1: BTC from base case simulation.

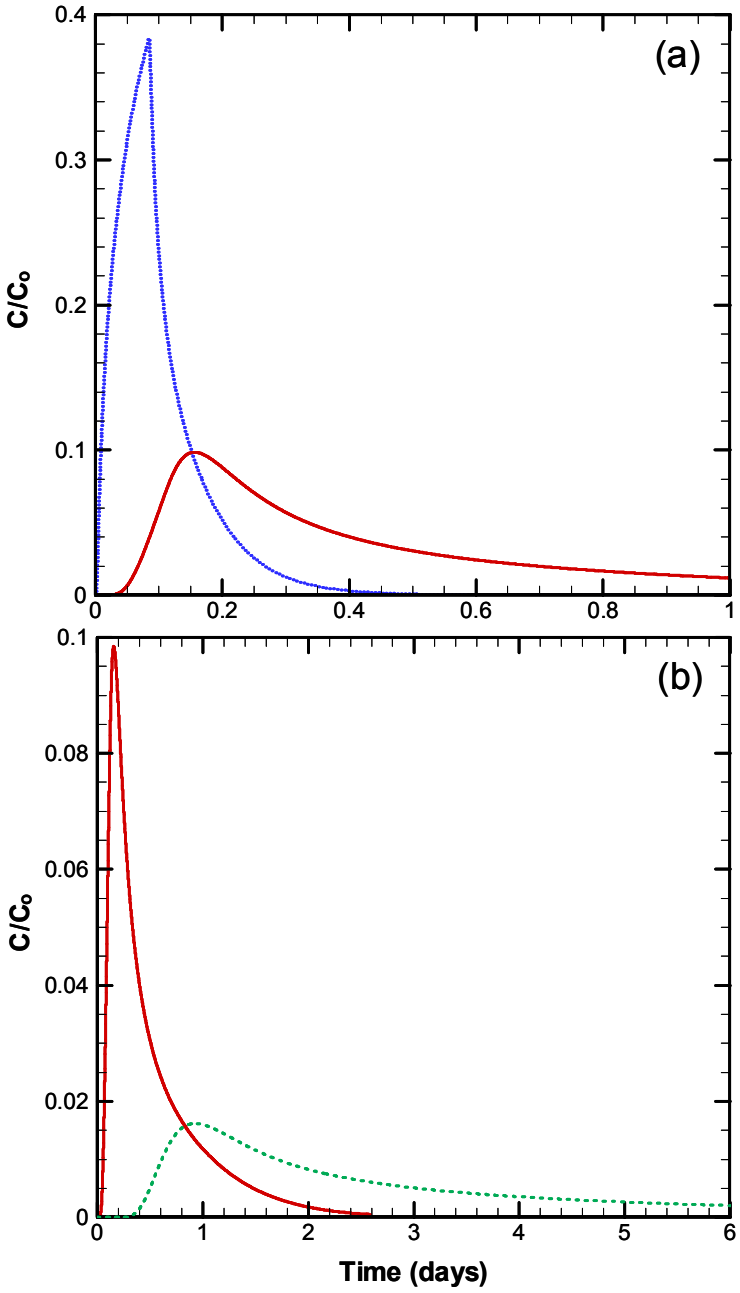

Figure 5.2: Simulated BTCs from (a) L = 0.8 m (solid), and L = 0.4 m (dotted), and (b) L = 0.8 m (solid), and L = 1.5 (dashed).

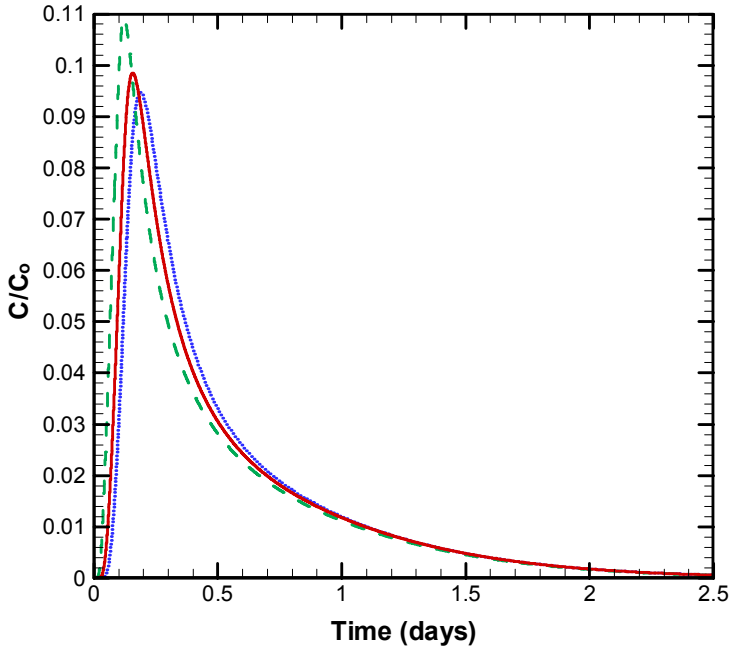

Figure 5.3: Simulated BTCs using a half-chamber length of 0.3 m (solid), 0.15 m (dotted), and 0.45 m (dashed).

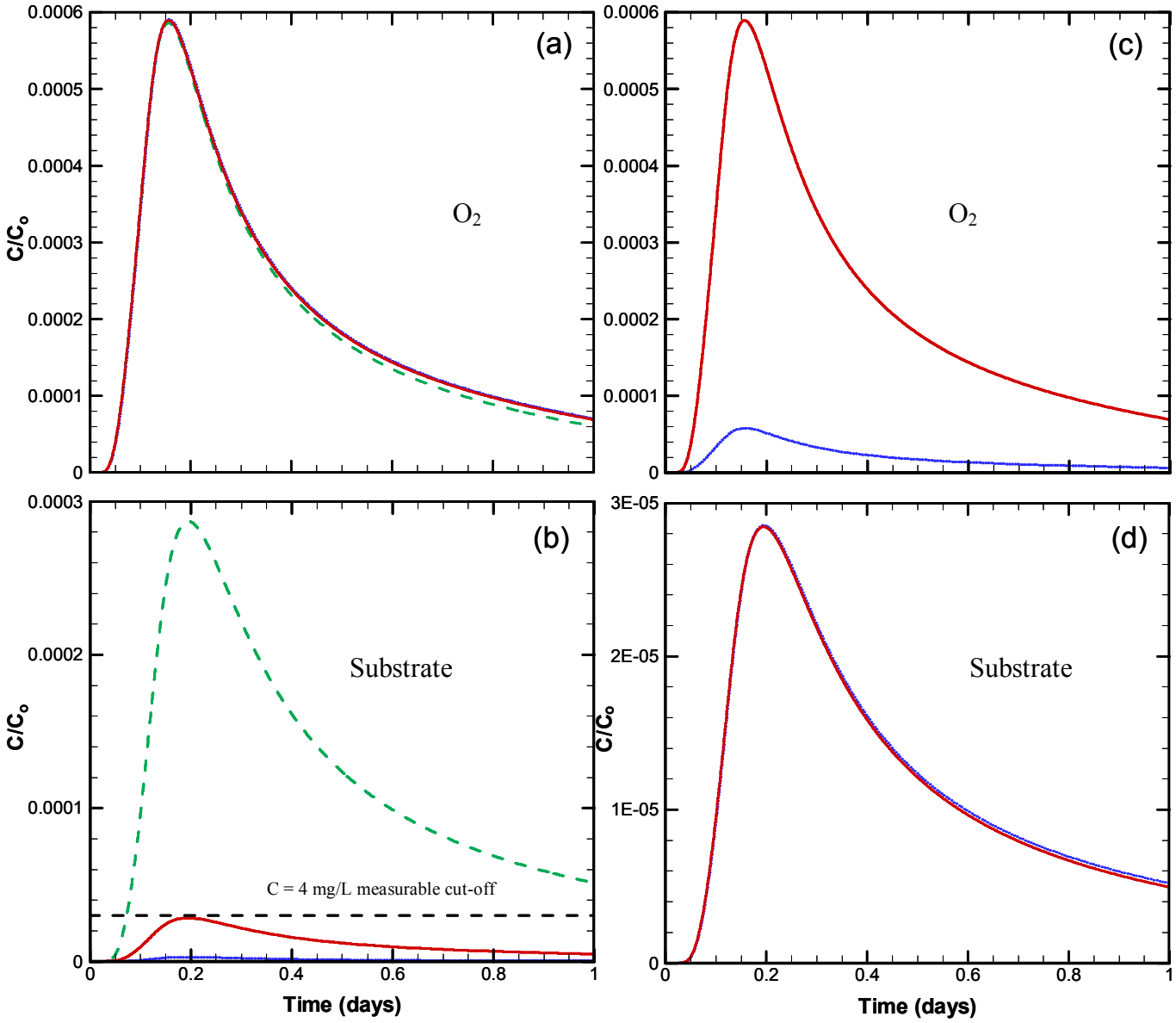

Figure 5.4: Simulated BTCs when $C_{substrate}$ = 4.0 mg/L (dashed), 0.04 mg/L (dotted) and 0.4 mg/L (solid) for the (a) electron acceptor (O_2), and (b) substrate (toluene). Resulting BTCs when $C_{electron\ acceptor}$ = 0.6 mg/L (dotted), and 6.0 mg/L (solid) for the (c) electron acceptor, and (d) substrate.

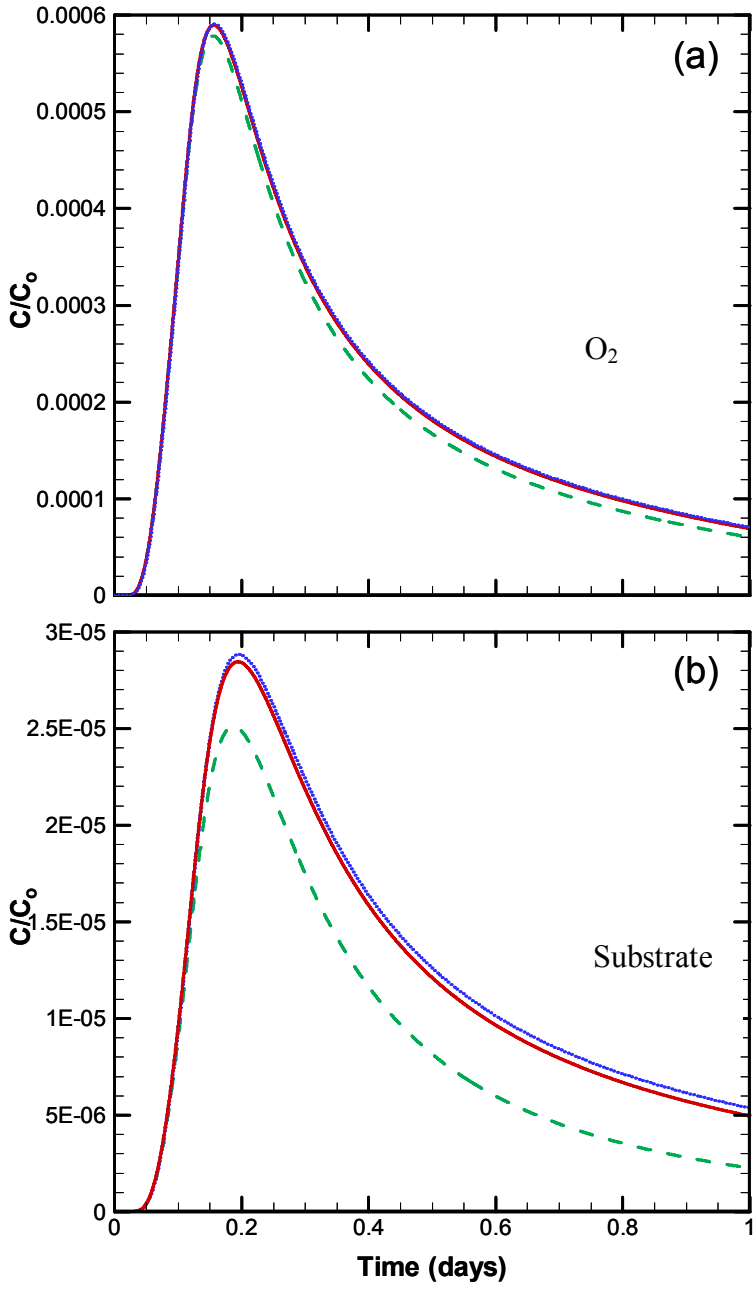

Figure 5.5: Simulated BTCs when M_t = 2.3 mg/L (dashed), M_t = 0.023 mg/L (dotted) and M_t = 0.23 mg/L (solid) for (a) electron acceptor (O_2), and (b) substrate (toluene).

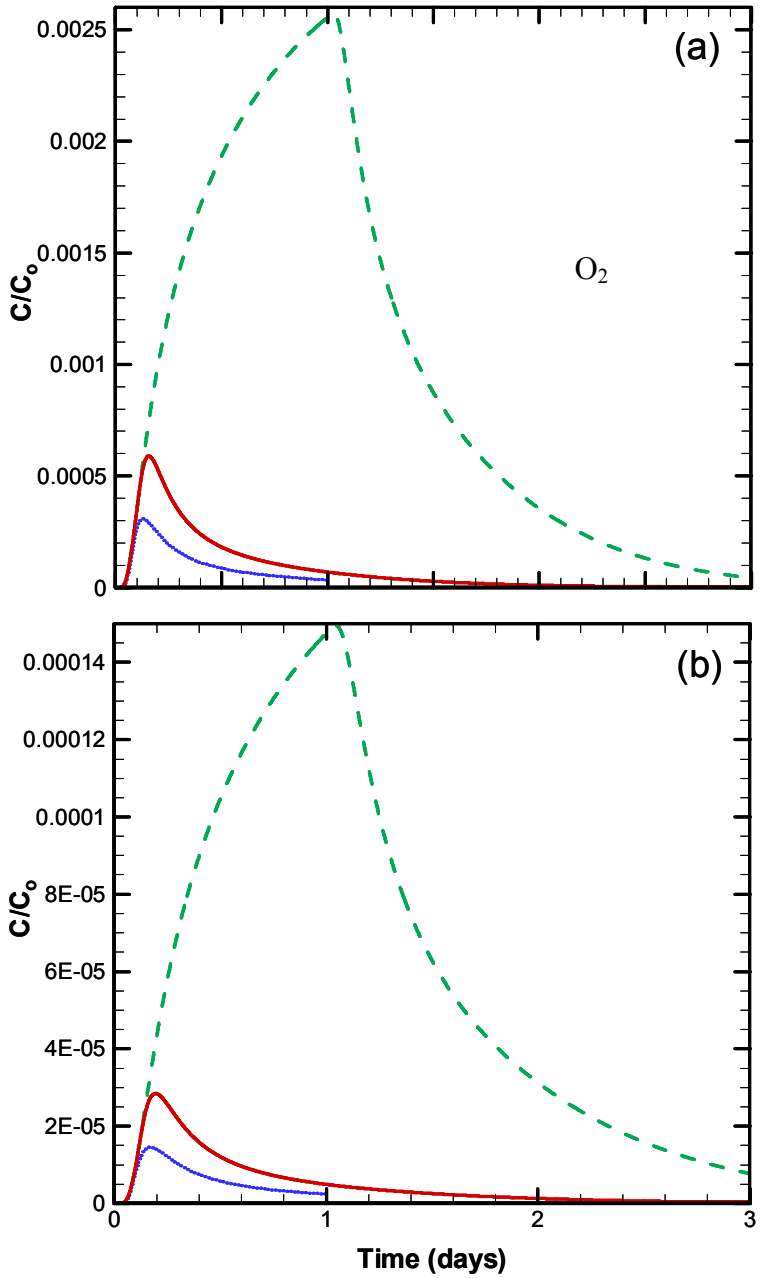

Figure 5.6: Simulated BTCs when the substrate and electron acceptor injection length = 24 hr (dashed), 1 hr (dotted), and 2 hr (solid) for (a) electron acceptor (O_2), and (b) substrate (toluene).

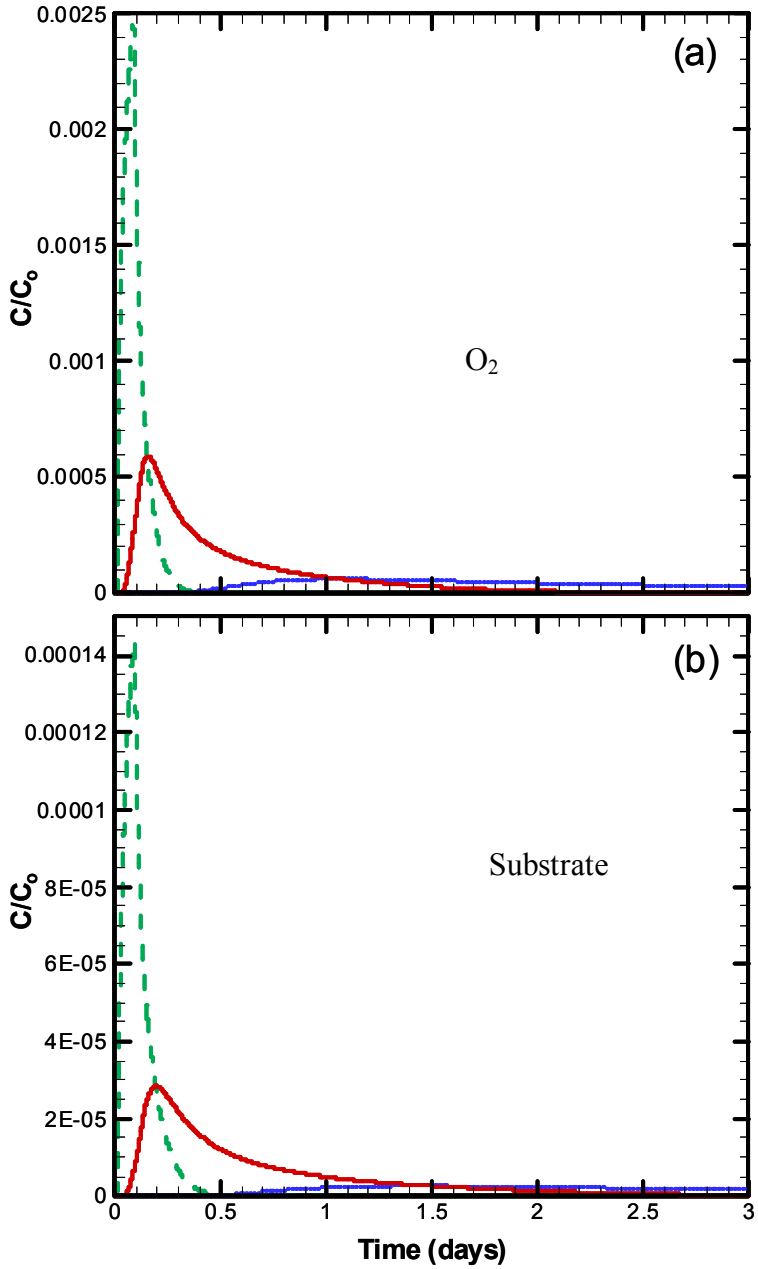

Figure 5.7: Simulated BTCs when Q = $1x10^{-3}$ m^3/s (dashed),$1x10^{-4}$ m^3/s (solid), and $1x10^{-5}$ m^3/s for the (a) electron acceptor (O_2), and (b) substrate (toluene).

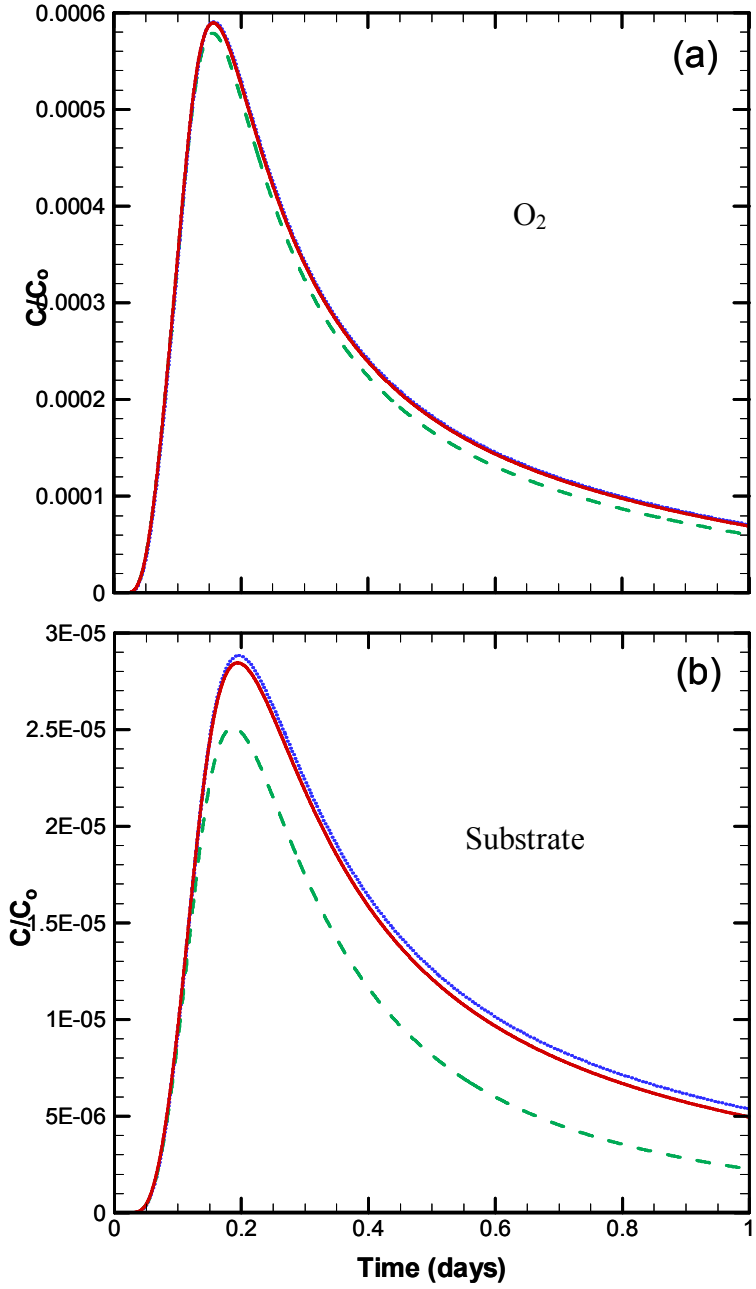

Figure 5.8: Simulated BTCs when the the maximum utilization rate of the substrate = 5.7×10^{-5} sec^{-1} (dashed), 5.7×10^{-7} sec^{-1} (dotted), and 5.7×10^{-6} sec^{-1} (solid) for (a) electron acceptor (O_2), and (b) substrate (toluene).

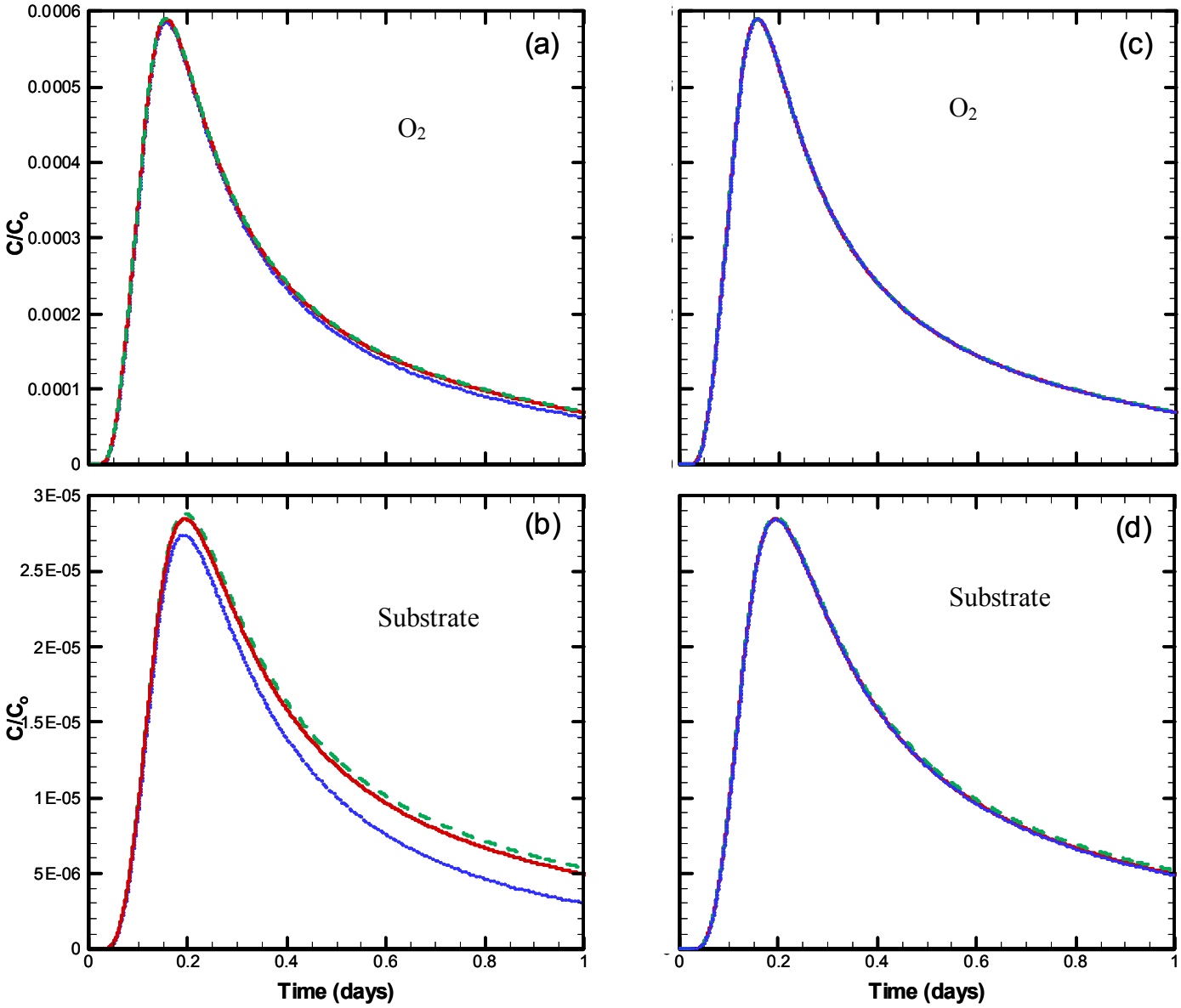

Figure 5.9: Simulated BTCs when the half-utilization constant of the substrate = 6.5 mg/L (dashed), 0.065 mg/L (dotted), and 0.65 mg/L (solid) for (a) electron acceptor (O_2), and (b) substrate (toluene). Simulated BTCs when the half-utilization constant of the electron acceptor = 1.0 mg/L (dashed), 0.01 mg/L (dotted), and 0.1 mg/L (solid) for (c) electron acceptor (O_2), and (d) substrate (toluene).

CHAPTER 6 CONCLUSIONS

6.1 CONCLUSIONS

The DFRTT physical tool has the potential for identifying aquifer characteristics that have been unattainable by *in situ* site characterization techniques preceding the DFRTTs introduction. Some of these characteristics include identifying, vertical hydraulic conductivity, redox capacity, sorption properties, and microbiological identification. In order to determine these characteristics, the DFRTT physical tool must rely upon a DFRTT specific model so that the resulting BTCs can be correlated. The objectives of this thesis were to: (1) develop and validate an efficient numerical framework for the reactive-transport component of a DFRTT interpretation model so that it can be used to accurately simulate a variety of reactive tracers; (2) improve the current aquifer property estimation capabilities so that rates of biodegradation can be determined; and (3) examine the design and operational parameters for initial field testing of the DFRTT at Canadian Forces Base (CFB) Borden. Therefore, the primary focus of this thesis was devoted to modifying the existing numerical comprehensive-reactive transport model (CRTM), originally developed by Thomson (2003), to include conservative and reactive tracer simulations and a Monod kinetics application. The improved CRTM applies operator-splitting (OS) techniques, which enable the transport and reactive components to be solved separately, thus reducing computational effort. A control volume (CV) approach was used for solving the transport component, while a fourth-order Runge-Kutta method was used for the reactive component. The newly implemented iterative OS techniques allowed for an iterative flux corrected transport (FCT) advective scheme to be employed. The improved CRTM was validated through comparisons of conservative and reactive tracers, to the exisiting advective and advective-dispersive streamtube models and to MODFLOW/MT3DMS.

Three advective schemes were implemented and comparisons were conducted to determine the most appropriate method for the given DFRTT conditions. The central differencing scheme (CDS) proved to be the most unreliable because of its non-monotone solutions; the upwind differencing scheme (UDS) was always montone but produced excess numerical dispersion. The FCT method contained the benefits of both CDS and UDS, however, it was computationally slower than the UDS since the FCT scheme required a minimum 3 iterations while UDS required 1.

Examination of the OS techniques indicated that in most cases there were no significant differences between any of the OS methods; however if a sink term became increasingly prominent, the iterative techniques were deemed superior over the non-iterative techniques because of their ability to correct mass depletion. It was also determined that because of FCTs second-order accuracy, the OS techniques employing FCT had better mass balance errors (MBEs) than those which did not.

The CRTM was used to design a DFRTT biodegradation experiment under CFB Borden conditions. Dipole parameters were altered so that a dipole configuration could be recommended for field testing. It was determined that a decent zone of influence aquifer volume (~ 65 m^3) with a detectable BTC tail occuring between 2 and 3 days, required a dipole length = 0.8 m, and a half-chamber length = 0.15 to 0.30 m. The oxidation of toluene by aerobic bacteria present within the Borden aquifer was also simulated. The purpose of these simulations was to obtain a detectable substrate BTC so that experimental parameters could be recommended for conducting a field experiment. To achieve a detectable substrate BTC the following recommendations were

made: (i) sampling events to occur once every 1 to 2 hours (if possible) so that the changes in effluent concentration can be documented accurately; (ii) dipole parameters from Section 5.1 with a standard 2" well be employed; (iii) a large substrate concentration be utilized (> 4.0 mg/L); (iv) a flow rate of $1x10^{-4}$ m^3/s be used; and (v) an injection duration of 2 hours be applied. As long as the field substrate BTC is measurable then Monod kinetics can be obtained after a field and CRTM BTC comparison; this enables us to understand the aquifer's biodegradation potential (for remedial design purposes).

6.2 RECOMMENDATIONS

The DFRTT application in conjunction with the CRTM contains enormous potential within the field of site characterization, however it is important that the two continually evolve. Recommendations for further extensions include:

- Validating the dual-Monod kinetics portion of the CRTM against an "off-the-shelf" model (e.g., MODFLOW/MT3DMS);
- Improving the existing transport component to include a higher-order advective scheme that requires less computational effort than the FCT, but is more accurate than the UDS (e.g., QUICK);
- Adding supplementary reaction terms to the CRTM reactive component (e.g., reaction products);
- Conducting field-scale experiments at CFB Borden to verify the CRTM against field data;
- Utilizing PEST for the field and CRTM BTC matching process; and
- Extending the DFRTT and CRTM to:

- assess the natural oxidant demand (NOD)
- be used as a remedial tool

References

ASTM (1998). Standard Guide D 4043 for Selection of Aquifer Test Methods in Determining Hydraulic Properties by Well Techniques. 04.08 Soil and Rock (1): D420-4914.

American Public Health Association; L.S. Clescerl, A.E. Greenberg, and A.D. Eaton, Ed. (1999). "Standard Methods for the Examination of Water and Wastewater, 20th Edition".

Ball, W. P., and P.V. Roberts (1991). "Long Term Sorption of Halogenated Organic Chemicals in Aquifer Materials." Environmental Science and Technology 25(7): 1223-1237.

Barcelona, M. J., and D.R. Jaglowski (1999). Considerations for Innovative Remediation Technology Evaluation Sampling Plans. Innovative Subsurface Remediation: Field Testing of Physical, Chemical, and Characterization Technologies. M. L. Brusseau, Sabatini, D.A., Gierke, J.S., and M.D. Annable. Washington, D.C., American Chemical Society: 196-207.

Barry, D. A., Miller, C.T., and P.J. Culligan-Hensley (1995). "Temporal Discretization Errors in Non-Iterative Split-Operator Approaches to Solving Chemical Reaction/Groundwater Transport Models." Journal of Contaminant Hydrology(22): 1-17.

Baveye, P., and A.J. Valocchi (1989). "An Evaluation of Mathematical Models of the Transport of Biologically Reacting Solutes in Saturated Soils and Aquifers." Water Resources Research 25(6): 1413-1421.

Bear, J. (1972). Dynamics of Fluids in Porous Media. New York, American Elsevier Publishing Company.

Bedient, P. B., Rifai, H.S., and C.J. Newell (1994). Ground Water Contamination Transport and Remediation. Englewood Cliffs, New Jersey, PTR Prentice Hall.

Benson, R. C. (2006). Remote Sensing and Geophysical Methods for Evaluation of Subsurface Conditions. Practical Handbook of Environmental Site Characterization and Ground-Water Monitoring. D. M. Nielsen. Boca Raton, FL, CRC Press Taylor & Francis Group: 249-296.

Borden, R. C., and P.B. Bedient (1986). "Transport of Dissolved Hydrocarbons Influenced by Oxygen-Limited Biodegradation, 1. Theoretical Development." Water Resources Research 22(13): 1973-1982.

Burns, W. A., Jr. (1969). "New Single-Well Test for Determining Vertical Permeability." Trans. Soc. Pet. Eng. AIME 246: 743-752.

Carrayrou, J., Mosé, R., and P. Behra (2004). "Operator-Splitting Procedures for Reactive Transport and Comparison of Mass Balance Errors." Journal of Contaminant Hydrology(68): 239-268.

Cirpka, O. A., Frind, E.O., and R. Helmig (1999a). "Numerical Methods for Reactive Transport on Rectangular and Streamline-Oriented Grids." Advances in Water Resources 22(7): 711-728.

Clement, T. P., Truex, M.J., and B.S. Hooker (1997). "Two-Well Test Method for Determining Hydraulic Properties of Aquifers." Ground Water 35(4): 698-703.

Crane, M. J., and M.J. Blunt (1999). "Streamline-Based Simulation of Solute Transport." Water Resources Research 35(10): 3061-3078.

Doherty, J. L. (2000). "PEST: Model Independent Parameter Estimation, Preface to the 4th Edition." Watermark Numerical Computing.

Dwarakanath, V., Deeds, N., and G.A. Pope (1999). "Analysis of Partitioning Interwell Tracer Tests." Environmental Science and Technology 33(21): 3829-3836.

Feld, J. (1965). Soil Mechanics and Foundations. Building Construction Handbook. F. S. Merritt, McGraw-Hill.

Ferziger, J. H., and M. Peric (1999). Computational Methods for Fluid Dynamics, Springer Verlag.

Fetter, C. W. (1993). Contaminant Hydrogeology. USA, Macmillan Publishing Company.

Frind, E. O. (1988). "Solution of the Advection-Dispersion Equation with Free Exit Boundary." Numerical Methods for Partial Differential Equations 4(4): 301-314.

Gelhar, L. W., and M.A. Collins (1971). "General Analysis of Longitudinal Dispersion in Nonuniform Flow." Water Resources Research 7(6): 1511-1521.

Ghiorse, W.C., and J.T. Wilson (1988). Microbial Ecology of the Terrestrial Subsurface. Advances in Applied Microbiology vol. 33. San Diego, CA, Academic Press: 107-172.

Gillham, R. W., O'Hannesin, S.F., Ptacek, C.J., and J.F. Barker (1987). Evaluation of Small Scale Retardation Tests for BTEX in Groundwater. Report 87-3. Ottawa, Canada, Petroleum Association for Conservation of the Canadian Environment: 58.

Güven, O., Falta, R.W., Molz, F.J., and J.G. Melville (1986). "A Simplified Analysis of Two-Well Tracer Tests in Stratified Aquifers." Ground Water 24(1): 63-71.

Halihan, T., and V.A. Zlotnik (2002). "Asymmetric Dipole Flow Test in a Fractured Carbonate Aquifer." Ground Water 40(5): 491-499.

Hall, S. H., Luttrell, S.P., AND W.E. Cronin (1991). "A Method for Estimating Effective Porosity and Ground Water Velocity." Ground Water 29(2): 171-174.

Hantush, M. S. (1961). "Drawdown Around a Partially Penetrating Well." Journal of the Hydraulics Division, Proceedings of the American Society of Civil Engineers 87(4): 83-98.

Hempen, G. L., and A.W. Hatheway (1992). Geophysical Methods for Hazardous Waste Site Characterization, Association of Engineering Geologists.

Herrling, B., and J. Stamm; T.F. Russel, R.E. Ewing, C.A. Brebbia, W.G. Gray, and G.F. Pinder, Ed. (1992). Numerical Results of Calculated 3D Vertical Circulation Flows Around Wells with Two Screens Sections for In Situ or On-Site Aquifer Remediation. Computational Methods in Water Resources IX, Numerical Methods in Water Resources. New York, Elsevier Science.

Herrling, B., and W. Buermann (1990). A New Method for In-Situ Remediation of Volatile Contaminants in Groundwater - Numerical Simulation of the Flow Regime. Proceedings of the Eighth International Conference on Computational Methods in Water Resources, Computational Methods in Subsurface Hydrology, Italy, Springer-Verlag.

Herzer, J., and W. Kinzelbach (1989). "Coupling of Transport and Chemical Processes in Numerical Transport Models." Geoderma 44: 115-127.

Huang, W. E., Oswald, S.E., Lerner, D.N., Smith, C.C., and C. Zheng (2003). "Dissolved Oxygen Imaging in a Porous Medium to Investigate Biodegradation in a Plume with Limited Electron Acceptor Supply." Environmental Science and Technology 37(9): 1905-1911.

Hundsdorfer, W., and J.G. Verwer (1995). "A Not on Splitting Errors for Advection-Reaction Equations." Applied Numerical Mathematics 18: 191-199.

Hvilshøj, S., Jensen, K.J., and B. Madsen (2000). "Single-Well Dipole Flow Tests: Parameter Estimation and Field Testing." Ground Water 38(1): 53-62.

Imhoff, P. T., and K. Pirestani (2004). "Influence of Mass Transfer Resistance on Detection of Nonaqueous Phase Liquids with Partitioning Tracer Tests." Advances in Water Resources 27: 429-444.

Istok, J. D. (1989). Groundwater Modeling by the Finite Element Method. Washington, D.C., American Geophysical Union.

Istok, J. D., Humphrey, M.D., Schroth, M.H., Hyman, M.R., and K.T. O'Reilly (1997). "Single-Well, "Push-Pull" Test for In Situ Determination of Microbial Activities." Ground Water 35(4): 619-631.

Istok, J. D., Field, J.A., Schroth, M.H., Sawyer, T.E., and M.D. Humphrey (1999). "Laboratory and Field Investigation of Surfactant Sorption using Single-Well, "Push-Pull" Tests." Ground Water 37(4): 589-598.

Istok, J. D., Field, J.A., Schroth, M.H., Davis, B.M., and V. Dwarakanath (2002). "Single-Well "Push-Pull" Partitioning Tracer Test for NAPL Detection in the Subsurface." Environmental Science and Technology 36(12): 2708-2716.

Jin, M., Delshad, M., Dwarakanath, V., McKinney, D.C., Pope, G.A., Sepehrnoori, K., Tilburg, C.E., and R.E. Jackson (1995). "Partitioning Tracer Test for Detection, Estimation, and Remediation Performance Assessment of Subsurface Non-Aqueous Phase Liquids." Water Resources Research 31(5): 1201-1211.

Kabala, Z. J. (1993). "The Dipole Flow Test: A New Single-Borehole Test for Aquifer Characterization." Water Resources Research 29(1): 99-107.

Kaluarachchi, J. J., and J. Morshed (1995). "Critical Assessment of the Operator-Splitting Technique in Solving the Advection-Dispersion-Reaction Equation: 1. First-Order Reaction." Advances in Water Resources 18(2): 89-100.

Kesavan, P., and V.J. Law (2005). "Practical Identifiability of Parameters in Monod Kinetics and Statistical Analysis of Residuals." Biochemical Engineering 24: 95-104.

Kim, Y., Kim, J.H., Son, B.H., and S.W. Oa (2005). "A Single Well Push-Pull Test Method for In Situ Determination of Denitrification Rates in a Nitrate-Contaminated Groundwater Aquifer." Water Science & Technology 52(8): 77-86.

Kleineidam, S., Rügner, H., and P. Grathwohl (2004). "Desorption Kinetics of Phenanthrene in Aquifer Material Lacks Hysteresis." Environmental Science and Technology 38(15): 4169-4175.

Leonard, B. P. (1979). "A Stable and Accurate Convective Modeling Procedure Based Upon Quadratic Upstream Interpolation." Computer Methods in Applied Mechanics and Engineering 19(1): 59-98.

MacFarlane, D. S., Cherry, J.A., Gillham, R.W., and E.A. Sudicky (1983). "Migration of Contaminants in Groundwater at a Landfill: A Case Study, 1, Groundwater Flow and Plume Delineation." Journal of Hydrology 63: 1-29.

Mackay, D. M., Freyber, D.L., and P.V. Roberts (1986). "A Natural Gradient Experiment on Solute Transport in a Sand Aquifer: Approach and Overview of Plume Movement." Water Resources Research 22(13): 2017-2029.

MacQuarrie, K. T. B., Sudicky, E.A., and E.O. Frind (1989). "Simulation of Biodegradable Organic Contaminants in Groundwater 1. Numerical Formulation in Principal Directions." Water Resources Research 26(2): 207-222.

MacQuarrie, K. T. B., Sudicky, E.A., and E.O. Frind (1990). "Simulation of Biodegradable Organic Contaminants in Groundwater 1. Numerical Formulation in Principal Directions." Water Resources Research 26(2): 207-222.

Martian, P., Sorensor, K.S. Jr., and L.N. Peterson (2003). "A Critique of the Internal Tracer Method for Estimating Contaminant Degradation Rates." Ground Water 41(5): 632-639.

McAllister, P. M., and C.Y. Chiang (1994). "A Practical Approach to Evaluating Natural Attenuation of Contaminants in Ground Water." Ground Water Monitoring and Remediation 14(161-173).

McKnight, D., Smalley, A.L., Banwart, S.A., Lerner, D.N., Thomson, N.R., Thornton, S.F., and R.D. Wilson (2003). A Laboratory-Scale Dipole Flow and Reactive Tracer Test. The Eighth International Conference on Contaminated Soil (CONSOIL), Gent, Belgium.

Miller, G. M., and A.C. Elmore (2005). "Modeling of a Groundwater Circulation Well Removal Action Alternative." Practice Periodical of Hazardous, Toxic, and Radioactive Waste Management 9(2): 122-129.

Molson, J. W. (1988). Three-Dimensional Numerical Simulation of Groundwater Flow and Contaminant Transport at the Borden Landfill. Department of Earth Sciences. Waterloo, ON, University of Waterloo. Ph.D.

Moradi, A., Abbaspour, K.C., and M. Afyuni (2005). "Modelling field-scale cadmium transport below the root zone of a sewage sludge amended soil in an arid region in Central Iran." Journal of Contaminant Hydrology 79(3-4): 187-206.

Mumford, K. G., Lamarche, C.S., and N.R. Thomson (2004). "Natural Oxidant Demand of Aquifer Materials Using the Push-Pull Technique." Journal of Environmental Engineering 130(10): 1139-1146.

Murphy, E.M., and T.R. Ginn (2000). “Modeling Microbial Processes in Porous Media” Hydrogeology Journal 8: 142-158.

Nielsen, D. M., Nielsen, G.L., and L.M. Preslo (2006). Environmental Site Characterization. Practical Handbook of Environmental Site Characterization and Ground-Water Monitoring. D. M. Nielsen. Boca Raton, FL, CRC Press Taylor & Francis Group: 35-206.

Nielsen, D. R., van Genuchten, M.T, and J.W. Biggar (1986). "Water Flow and Solute Transport in the Unsaturated Zone." Water Resources Research 22(9): 89S-108S.

O'Hannesin, S. F. (1981). Spatial Variability of Grain-Size Parameters and Hydraulic Conductivity at a Dispersion Test Site. Environmental Studies. Waterloo, ON, University of Waterloo. Bachelor Honours Report.

Oran, E. S., and J.P. Boris (1987). Numerical Simulation of Reactive Flow. New York, NY., Elsevier.

Pitterle, M. T., Andersen, R.G., Novak, J.T., and M.A. Widdowson (2005). "Push-Pull Tests to Quantify In Situ Degradation Rates at a Phytoremediation Site." Environmental Science and Technology 39(23): 9317-9323.

Pollard, A., and A.L.W. Siu (1982). "The Calculation of Some Laminar Flows Using Various Discretization Techniques." Computer Methods in Applied Mechanics and Engineering 35(3): 293-313.

Ptak, T., and G. Schmid (1996). "Dual-Tracer Transport Experiments in a Physically and Chemically Heterogeneous Porous Aquifer: Effective Transport Parameters and Spatial Variability." Journal of Hydrology 183(1-2): 117-138.

Rügner, H., Kleineidam, and P. Grathwohl (1999). "Long Term Sorption Kinetics of Phenanthrene in Aquifer Materials." Environmental Science and Technology 33: 1645-1651.

Ruud, N.C. and Z.J. Kabala (1997). "Response of a Partially Penetrating Well in a Heterogeneous Aquifer: Integrated Well-Face Flux versus Uniform Well-Face Flux Boundary Conditions." Journal of Hydrology 194(1-4): 76-94.

Sara, M. N. (2003). Site Assessment and Remediation Handbook. USA, Lewis Publisher.

Schirmer, M., Butler, B.J., Roy, J.W., Frind, E.O., and J.F. Barker (1999). "A Relative-Least-Squares Technique to Determine Unique Monod Kinetic Parameters of BTEX Compounds using Batch Experiments." Journal of Contaminant Hydrology 37: 69-86.

Schroth, M. H., and J.D. Isotok (2006). "Models to Determine First-Order Rate Coefficients from Single-Well Push-Pull Tests." Ground Water 44(2): 275-283.

Seth, D., Sarkar, A., Ng, F.T.T., and G.L. Rempel (2005). "Uncertainties in the Simulation of Catalytic Distillation Process: A Systematic Grid Refinement Study." Chemical Engineering Science 60: 5445-5457.

Sevee, J. (2006). Methods and Procedures for Defining Aquifer Parameters. Practical Handbook of Environmental Site Characterization and Ground-Water Monitoring. D. M. Nielsen. Boca Raton, FL, CRC Press Taylor & Francis Group: 913-958.

Steefel, C. I., and K.T.B. MacQuarrie; P.C. Lichtner, C.I. Steefel, and E.H. Oelkers, Ed. (1996). Approaches to Modeling of Reactive Transport in Porous Media. Reviews in Minearology, Reactive Transport in Porous Media, Mineralogical Society of America.

Strang, G. (1968). "On the Construction and Comparison of Difference Schemes." Journal of Numerical Analysis 5(3): 506-517.

Sudicky, E. A. (1983). An Advection-Diffusion Theory of Contaminant Transport for Stratified Porous Media. Department of Earth Sciences, University of Waterloo. Ph.D.

Sudicky, E. A. (1986). "A Natural Gradient Experiment on Solute Transport in a Sand Aquifer: Spatial Variability of Hydraulic Conductivity and Its Role in the Dispersion Process." Water Resources Research 22(13): 2069-2082.

Sudicky, E. A., Unger, A.J.A, and S. Lacombe (1995). "A Non-Iterative Technique for the Direct Implementation of Well Bore Boundary Conditions in Three-Dimensional Heterogeneous Formations." Water Resources Research 31(2): 411-415.

Sutton, D. J., Kabala, Z.J., Schaad, D.E., and N.C. Ruud (2000). "The Dipole-Flow Test With A Tracer: A New Single-Borehole Tracer Test for Aquifer Characterization." Journal of Contaminant Hydrology 44: 77-101.

Thomson, N. R. (2003). Development of a Mathematical Interpretation Model for the Aquifer Assessment Tool; Working Draft., Internal Report. Waterloo, ON, Department of Civil Engineering, University of Waterloo: 43 + appendices.

Thomson, N. R., Reiha, B., McKnight, D., Smalley, A.L., and S.A. Banwart (2005). An Overview of the Dipole Flow In Situ Reactor. CSCE, Toronto, ON.

Tiedeman, C. R., and P.A. Hsieh (2004). "Evaluation of Longitudinal Dispersivity Estimates from Simulated Forced- and Natural-Gradient Tracer Tests in Heterogeneous Aquifers." Water Resources Research 40(W01512).

Tomich, J. F., Dalton, R.L. (Jr), Deabs, H.A., and L.K. Shallenberger (1973). "Single-Well Tracer Method to Measure Residual Oil Saturation." Journal of Petroleum Technology: 211-218.

Trench, W. F. (2000). Elementary Differential Equations, Brooks/Cole.

USEPA (1991). Methods for the Determination of Organic Compounds in Drinking Water (EPA 600/4-88-039).

USEPA (2000). Innovations in Site Characterization: Geophysical Investigations at Hazardous Waste Sites (EPA 542-R-00-003).

Valocchi, A. J., and M. Malmstead (1992). "Accuracy of Operator Splitting for Advection-Dispersion-Reaction Problems." Water Resources Research 28(5): 1471-1476.

Waterloo Hydrogeologic, Inc (2002). Visual MODFLOW Pro Version 2.83. Waterloo, ON.

Welty, C., and L.W. Gelhar (1994). "Evaluation of Longitudinal Dispersivity from Non-uniform Flow Tracer Tests." Journal of Hydrology 153: 71-102.

Yeh, G. T., and V.S. Tripathi (1991). "A Model for Simulating Transport of Reactive Multispecies Components: Model Development and Demonstration." Water Resources Research 27(12): 3075-3094.

Zhang, H., and H.M. Selim (2005). "Kinetics of Arsenate Adsorption-Desorption in Soils." Environmental Science and Technology 39: 6101-6108.

Zheng, C., and P.P. Wang (1998). MT3DMS, A Modular Three-Dimensional Multispecies Transport Model for Simulation of Advection, Dispersion and Chemical Reactions of Contaminants in Groundwater Systems, Departments of Geology and Mathematics. University of Alabama.

Zheng, C., Hill, M.C., and P.A. Hsieh (2001). MODFLOW-2000, The U.S. Geological Survey Modular Ground Water Model – User Guide to the LMT6 Package, the Linkage with MT3DMS for Multi-Species Mass Transport Modeling: US Geological Survey Open-File Report 01-82, Reston Virgina.

Zlotnik, V. A., and G. Ledder (1996). "Theory of Dipole Flow in Uniform Anisotropic Aquifers." Water Resources Research 32(4): 1119-1128.

Zlotnik, V. A., and B.R. Zurbuchen (1998). "Dipole Probe: Design and Field Applications of a Single-Borehole Device for Measurements of Vertical Variations of Hydraulic Conductivity." Ground Water 36(6): 884-893.

Zlotnik, V. A., Zurbuchen, B.R., and T. Ptak (2001). "The Steady-State Dipole Flow Test for Characterization of Hydraulic Conductivity Statistics in a Highly Permeable Aquifer: Horkheimer Insel Site, Germany." Ground Water 39(4): 504-516.

Zysset, A., Stauffer, F., and T. Dracos (1994). "Modeling of Chemically Reative Groundwater Transport." Water Resources Research 30(7): 2217-2228

APPENDIX A

Eq. (3.57) contains one volume integral and two surface integrals, which are approximated for the typical CV shown in Figure 3.2.

A.1 Storage Integral

The storage integral, for the integral form of the mass conservation equation, is represented by the left-hand side of Eq. (3.57) and is numerically approximated by the mean value and the CV volume as given by,

$$\frac{\partial}{\partial t}\int_V \theta C \; dV \approx \frac{\partial}{\partial t}\left(\theta C_p V_p\right) \approx \frac{\left(\theta V_p C_p\right)^{n+1} - \left(\theta V_p C_p\right)^n}{\Delta t} \tag{A.1}$$

where C_P is concentration at node P (M/L^3), V_p is the volume of CV$_p$ (L^3), and θ is porosity.

A.2 Dispersion Integral

The dispersive flux term was obtained from the integral form of the mass conservation equation (Eq. (3.56)) and can be numerically expressed as,

$$\int_S \boldsymbol{D}\nabla C \cdot \hat{\boldsymbol{n}} \; dS \approx \sum_f D_f \frac{\partial C}{\partial n_f} S_f \tag{A.2}$$

where D_f represents the dispersion coefficient at the facial integration point (L^2/T), $\frac{\partial C}{\partial n_f}$ is the concentration gradient normal to the CV face f (M/L^3), and S_f is the surface area of face f (L). The dispersion coefficients are estimated from,

$$\begin{aligned} D_s &= \alpha_l \left|q_s\right| + \theta_s D_m^{eff} \\ D_n &= \alpha_l \left|q_n\right| + \theta_n D_m^{eff} \\ D_e &= \alpha_t \left|\overline{q}\right| + \theta_e D_m^{eff} \\ D_w &= \alpha_t \left|\overline{q}\right| + \theta_w D_m^{eff} \end{aligned} \tag{A.3}$$

where α_l is longitudinal dispersivity (L^2/T), α_t is transverse dispersivity (L^2/T), q_s and q_n is the Darcy flux across the south and north faces of the CV, θ_s, θ_n, θ_e, and θ_w is the average porosity at the CV face, D_m^{eff} is the user defined effective molecular diffusion coefficient, and $\overline{q}$ is the average Darcy flux through the CV and may be represented by,

$$\overline{q} = \sqrt{q_s^2 + q_n^2} \tag{A.4}$$

The normal concentration gradient is approximated as a linear interpolation between the adjacent computational nodes; an example for the south face of a CV is,

$$\frac{\partial C}{\partial n_s} \approx \frac{C_P - C_S}{l_{PS}} \tag{A.5}$$

where C_P, C_S is the nodal concentration for the CV_P and CV_S, respectively and l_{PS} is the distance between the nodal locations passing through the south face integration point.

A.3 Advection Integral

The integral form of the advective flux term was obtained from the mass conservation equation (Eq. (3.57)) and can be numerically approximated as,

$$\int_S C\hat{\boldsymbol{q}} \cdot \hat{\boldsymbol{n}}\ dS \approx \sum_f C_f \dot{m}_f \tag{A.6}$$

where C_f is facial concentration at the integration point (M/L^3), and $\dot{m}_f$ is the mass flux normal to face f. Due to the SOM used, only two advective flux terms per CV are generated (the north and south face). As stated in Section 3.4.2, three schemes were implemented to interpolate the concentration at each facial integration point.

A.3.1 Central Differencing Scheme

In order to estimate a CV facial concentration for the central differencing scheme, a linear profile between the two nodes adjoining to the face-of-interest is assumed (Ferziger and Peric, 1999) as given by,

$$\begin{aligned} C_n &= (1-\lambda_n)C_P + \lambda_n C_N \\ C_s &= (1-\lambda_s)C_P + \lambda_s C_S \end{aligned} \tag{A.7}$$

with,

$$\begin{aligned} \lambda_s &= \frac{l_{Ps}}{l_{PS}} \\ \lambda_n &= \frac{l_{Pn}}{l_{PN}} \end{aligned} \tag{A.8}$$

where C_n and C_s are concentrations at the integration points along the north and south faces, respectively (M/L^3), C_P, C_N, and C_S are nodal concentrations at nodes P, N, and S, respectively (M/L^3), l_{Pn} and l_{Ps} are integration point lengths (L), and l_{PN} and l_{PS} is the distance between respective nodes passing through the integration points (L) (Figure A.1). The advantage to using the central differencing scheme is that it is second-order accurate in space; however, this scheme is known to produce undesirable oscillatory solutions (typically when the Peclet number is ≥ 2). Grid refinement helps reduce instability; however, refining the mesh also increases computational effort (Leonard, 1979; and Versteeg and Malalasekera, 1995).

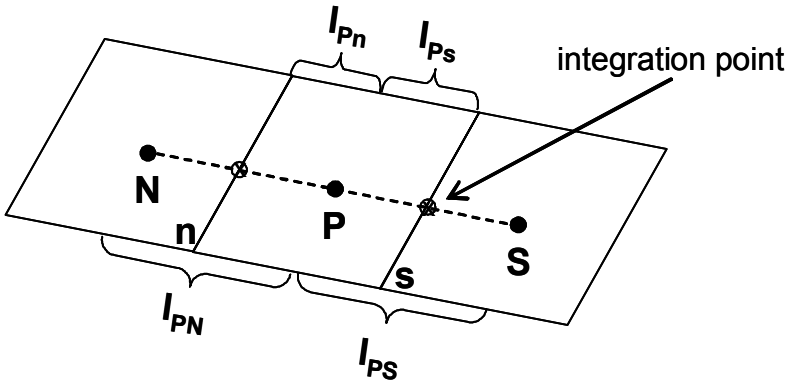

Figure A.1: Schematic diagram of nodal and integration point lengths.

A.3.2 Upwind Differencing Scheme (UDS)

In order to interpolate a CV facial concentration using the upwind differencing scheme, the face-of-interest is equivalent to using a backward or forward differencing approximation depending on the flow direction (Ferziger and Peric, 1999). For example, the concentration at the south face may be interpolated by,

$$C_s = \begin{cases} C_P & if\ \dot{m}_s\ is > 0 \\ C_S & if\ \dot{m}_s\ is < 0 \end{cases} \tag{A.9}$$

This approximation is the only scheme that is unconditionally stable (i.e., it will never yield oscillatory solutions); however, because of its first-order accuracy, it produces unwanted numerical dispersion. Grid refinement helps reduce numerical dispersion but again, this increases computation time (Leonard, 1979; and Versteeg and Malalasekera, 1995).

A.3.3 SOU with LDC

According to Versteeg and Malalasekera (1995), considerable research has been directed towards improving the standard discretization schemes and has resulted in the development of the quadratic-upstream interpolation for convective kinematics scheme (QUICK), the hybrid-differencing scheme and the second-order upwind scheme with linear deferred correction, also

known as flux corrected transport (FCT). The hybrid differencing scheme was first proposed by Spalding (1972) and is based on both the central and upwind differencing schemes. The hybrid scheme is highly stable, unconditionally bounded, and has the benefits of both the central and upwind differencing schemes. However, Han *et al.* (1981) and Pollard and Siu (1982) concluded that current higher-order differencing schemes are more precise since the hybrid is only first-order accurate. The third-order accurate differencing scheme, QUICK, was first introduced by Leonard (1979), which includes a three-point upstream-weighted quadratic interpolation system for determining CV face values. The face value is achieved by passing a quadratic function through the nodes on either side of the face, and one upstream node (Versteeg and Malalasekera, 1995). The concentration at the face is calculated from (Leonard, 1979),

$$C_f = \frac{6}{8}C_{i-1} + \frac{3}{8}C_i - \frac{1}{8}C_{i-2} \tag{A.10}$$

where node i is the furthest downstream node, $i\text{-}1$ is one node upstream from node i, and $i\text{-}2$ is two nodes upstream from node i. Leonard (1979), Versteeg and Malalasekera (1995), Han *et al.* (1981), Pollard and Siu (1982), and Hayase *et al.* (1992) indicate that QUICK is highly accurate and yields results almost indistinguishable from the exact solution; however, instability issues arise when the nodal concentration values on either side of the face-of-interest are negative (Han *et al.*, 1981; Pollard and Siu, 1982).

The second-order upwind (SOU) scheme, originally developed by Warming and Beam (1976), is unconditionally stable and second-order accurate; therefore it contains the benefits of both the CDS and UDS. The concentration at the face is represented by (Warming and Beam, 1976),

$$C_f = \begin{cases} C_i + \dfrac{\partial C_i}{\partial r}\left(r_f - r_i\right) + \dfrac{\partial C_i}{\partial z}\left(z_f - z_i\right) & if\ \dot{m}_f\ is > 0 \\ C_{i-1} + \dfrac{\partial C_S}{\partial r}\left(r_f - r_{i-1}\right) + \dfrac{\partial C_{i-1}}{\partial z}\left(z_f - z_{i-1}\right) & if\ \dot{m}_f\ is < 0 \end{cases} \tag{A.11}$$

where $\frac{\partial C_i}{\partial r}, \frac{\partial C_i}{\partial z}, \frac{\partial C_{i-1}}{\partial r}, \frac{\partial C_{i-1}}{\partial z}$ are linear correction terms (M/L^3/T), C_i and C_{i-1} are nodal concentrations at nodes *i* and *i-1*, respectively (M/L^3), and C_f is the concentration at the integration point on the face (M/L^3). Barth and Jespersen (1989) modified the second-order upwind (SOU) scheme by replacing its correction term with a deferred correction term (i.e., from the previous iteration) and introducing a blending factor, which is used to ensure solution stability. For the typical CV shown in Figure 3.2, the south face concentration is determined from,

$$C_s^{\,m+1} = \begin{cases} C_P^{\,m+1} + \beta\left[\dfrac{\partial C_P}{\partial r}\left(r_s - r_P\right) + \dfrac{\partial C_P}{\partial z}\left(z_s - z_P\right)\right]^m & if\ \dot{m}_s\ is > 0 \\ C_S^{\,m+1} + \beta\left[\dfrac{\partial C_S}{\partial r}\left(r_s - r_S\right) + \dfrac{\partial C_S}{\partial z}\left(z_s - z_S\right)\right]^m & if\ \dot{m}_s\ is < 0 \end{cases} \tag{A.12}$$

where $\frac{\partial C_P}{\partial r}, \frac{\partial C_P}{\partial z}, \frac{\partial C_S}{\partial r}, \frac{\partial C_S}{\partial z}$ are the reconstructed gradients (M/L^3/T), C_P and C_S are nodal concentrations at nodes *P* and *S*, respectively (M/L^3), and C_s is the concentration at the integration point on the south face (M/L^3), *m+1* and *m* represent the current iteration and previous iterations, respectively, and β is a blending factor. During each iteration the facial concentration is inspected for boundedness at each CV face. If the facial concentration is not bounded between the upstream and downstream nodal values than the blending factor is given a value of 0, resulting in a standard first-order UDS; if the solution is bounded than the blending factor is assigned a value between 0.0 and 1.0 resulting in SOU with LDC (Barth and Jespersen,

1989). The gradient at each node can be reconstructed by using least-squares approximation given by,

$$E = \sum_{nb} \left[C_{nb} - \left\{ C_i + \left[\frac{\partial C_i}{\partial r}(r_{nb} - r_i) + \frac{\partial C_i}{\partial z}(z_{nb} - z_i) \right] \right\} \right]^2 \tag{A.13}$$

where *nb* refers to the neighbouring nodal points of node *i*. The residual *E* can be minimized by taking the partial derivative of the least-squares approximation with respect to $\frac{\partial C}{\partial r}$ and $\frac{\partial C}{\partial z}$,

$$\begin{aligned} \frac{\partial E}{\partial \frac{\partial C_i}{\partial r}} &= 0 = \sum -2(r_{nb} - r_i) \left[C_{nb} - \left\{ C_i + \left[\frac{\partial C_i}{\partial r}(r_{nb} - r_i) + \frac{\partial C_i}{\partial z}(z_{nb} - z_i) \right] \right\} \right] \\ \frac{\partial E}{\partial \frac{\partial C_i}{\partial z}} &= 0 = \sum -2(z_{nb} - z_i) \left[C_{nb} - \left\{ C_i + \left[\frac{\partial C_i}{\partial r}(r_{nb} - r_i) + \frac{\partial C_i}{\partial z}(z_{nb} - z_i) \right] \right\} \right] \end{aligned} \tag{A.14}$$

which can be re-arranged into a 2x2 matrix,

$$\begin{bmatrix} -\sum (r_{nb} - r_i)^2 & -\sum (r_{nb} - r_i)(z_{nb} - z_i) \\ -\sum (z_{nb} - z_i)(r_{nb} - r_i) & -\sum (z_{nb} - z_i)^2 \end{bmatrix} \begin{Bmatrix} \frac{\partial C_i}{\partial r} \\ \frac{\partial C_i}{\partial z} \end{Bmatrix} = \begin{Bmatrix} \sum (r_{nb} - r_i)(C_{nb} - C_i) \\ \sum (z_{nb} - z_i)(C_{nb} - C_i) \end{Bmatrix} \tag{A.15}$$

Once the gradients have been determined from (A.15), an approximate value for the face concentration can be estimated by applying Eq. (A.12). Since the linear correction term is lagged by an iteration, this approximation is iterated until the solution converges.

Seth *et al.* (2005) stated that there may be convergence issues if the difference in gradients, from one-iteration-to-the-next, is large. However, this can be rectified by employing a method used to accelerate convergence, such as under-relaxation (Seth et al., 2005). There are very few comparison studies of SOU with LDC to other differencing schemes, and none that include hydrogeologic applications. Seth *et al.* (2005) used SOU with LDC for a catalytic distillation

process, while Biagioli (1998) used it to calculate laminar flows and compared the results to a total variation diminishing (TVD) scheme. The results from these studies showed that SOU with LDC was successful in producing accurate solutions, even for coarse grids.

A.4 Algebraic Equation System

The resulting algebraic equation for the ADE is represented by,

$$
\begin{aligned}
&\left\{\frac{(\theta V_P)}{\Delta t} - w[\dot{m}_{sP} + \dot{m}_{nP} - \Gamma_s - \Gamma_n - \Gamma_e - \Gamma_w]\right\} C_P^{t+\Delta t,m+1} + w[-\dot{m}_{sS} - \Gamma_s] C_S^{t+\Delta t,m+1} + \\
&w[-\dot{m}_{nN} - \Gamma_n] C_N^{t+\Delta t,m+1} + w[-\Gamma_e] C_E^{t+\Delta t,m+1} + w[-\Gamma_w] C_W^{t+\Delta t,m+1} + \\
&\gamma w[-\dot{m}_{sP}]\left[\frac{\partial C_P}{\partial r}(r_s - r_P) + \frac{\partial C_P}{\partial z}(z_s - z_P)\right]^{t+\Delta t,m} \beta_{sP}^{\,t+\Delta t,m} + \\
&\gamma w[-\dot{m}_{sS}]\left[\frac{\partial C_S}{\partial r}(r_s - r_S) + \frac{\partial C_S}{\partial z}(z_s - z_S)\right]^{t+\Delta t,m} \beta_{sS}^{\,t+\Delta t,m} + \\
&\gamma w[-\dot{m}_{nP}]\left[\frac{\partial C_P}{\partial r}(r_n - r_P) + \frac{\partial C_P}{\partial z}(z_n - z_P)\right]^{t+\Delta t,m} \beta_{nP}^{\,t+\Delta t,m} + \\
&\gamma w[-\dot{m}_{nN}]\left[\frac{\partial C_N}{\partial r}(r_n - r_N) + \frac{\partial C_N}{\partial z}(z_n - z_N)\right]^{t+\Delta t,m} \beta_{nN}^{\,t+\Delta t,m} = \\
&\left\{\frac{(\theta V_P)}{\Delta t} - (1-w)[\dot{m}_{sP} + \dot{m}_{nP} - \Gamma_s - \Gamma_n - \Gamma_e - \Gamma_w]\right\} C_P^{t,m} + (1-w)[-\dot{m}_{sS} - \Gamma_s] C_S^{t,m} + \\
&(1-w)[-\dot{m}_{nN} - \Gamma_n] C_N^{t,m} + (1-w)[-\Gamma_e] C_E^{t,m} + (1-w)[-\Gamma_w] C_W^{t,m} + \\
&\gamma(1-w)[-\dot{m}_{sP}]\left[\frac{\partial C_P}{\partial r}(r_s - r_P) + \frac{\partial C_P}{\partial z}(z_s - z_P)\right]^{t,m} \beta_{sP}^{\,t,m} + \\
&\gamma(1-w)[-\dot{m}_{sS}]\left[\frac{\partial C_S}{\partial r}(r_s - r_S) + \frac{\partial C_S}{\partial z}(z_s - z_S)\right]^{t,m} \beta_{sS}^{\,t,m} + \\
&\gamma(1-w)[-\dot{m}_{nP}]\left[\frac{\partial C_P}{\partial r}(r_n - r_P) + \frac{\partial C_P}{\partial z}(z_n - z_P)\right]^{t,m} \beta_{nP}^{\,t,m} + \\
&\gamma(1-w)[-\dot{m}_{nN}]\left[\frac{\partial C_N}{\partial r}(r_n - r_N) + \frac{\partial C_N}{\partial z}(z_n - z_N)\right]^{t,m} \beta_{nN}^{\,t,m}
\end{aligned}
\tag{A.16}
$$

where w is a temporal weighting factor, $\dot{m}_{sP}$,$\dot{m}_{sS}$,$\dot{m}_{nP}$,$\dot{m}_{nN}$ represent the respective advective terms, Γ_s ,Γ_n ,Γ_e ,Γ_w represent the respective dispersive terms, γ is a variable which contains a

value of either 1 when FCT is employed or 0 when CDS and UDS are employed, β_{sS} , β_{sP} , β_{nN} , β_{nP} represent the various blending factors, and *m+1* and *m* represent the current and previous iteration, respectively.

The advective terms are dependant on the employed advective scheme given by,

i) UDS and FCT

$$\begin{aligned}
\dot{m}_{sP} &= -max\left(\overline{q}_s \cdot \hat{n}_s S_s,\ 0\right) \\
\dot{m}_{sS} &= -min\left(\overline{q}_s \cdot \hat{n}_s S_s,\ 0\right) \\
\dot{m}_{nP} &= -max\left(\overline{q}_n \cdot \hat{n}_n S_n,\ 0\right) \\
\dot{m}_{nN} &= -min\left(\overline{q}_n \cdot \hat{n}_n S_n,\ 0\right)
\end{aligned} \tag{A.17}$$

ii) CDS

$$\begin{aligned}
\dot{m}_{sP} &= -\overline{q}_s \cdot \hat{n}_s S_s \left(1-\lambda_s\right) \\
\dot{m}_{sS} &= -\overline{q}_s \cdot \hat{n}_s S_s \left(\lambda_s\right) \\
\dot{m}_{nP} &= -\overline{q}_n \cdot \hat{n}_n S_n \left(1-\lambda_n\right) \\
\dot{m}_{nN} &= -\overline{q}_n \cdot \hat{n}_n S_n \left(\lambda_n\right)
\end{aligned} \tag{A.18}$$

where $\overline{q}_s$ and $\overline{q}_n$ represent the actual flux crossing the respective faces. Eq. (A.16) can be reduced to,

$$a_P C_P^{t+\Delta t,m+1} + a_S C_S^{t+\Delta t,m+1} + a_N C_N^{t+\Delta t,m+1} + a_E C_E^{t+\Delta t,m+1} + a_W C_W^{t+\Delta t,m+1} = b \tag{A.19}$$

where,

$$a_P = \left(\frac{\theta V_P}{\Delta t}\right) - w\left(\dot{m}_{sP} + \dot{m}_{nP} - \Gamma_s - \Gamma_n - \Gamma_w - \Gamma_e\right)$$

$$a_S = w\left(-\dot{m}_{sS} - \Gamma_s\right)$$

$$a_N = w\left(-\dot{m}_{nN} - \Gamma_n\right)$$

$$a_E = w\left(-\Gamma_e\right)$$

$$a_W = w\left(-\Gamma_w\right)$$

$$b = \left\{\left(\frac{\theta V_P}{\Delta t}\right) - (1-w)\left(\dot{m}_{sP} + \dot{m}_{nP} - \Gamma_s - \Gamma_n - \Gamma_w - \Gamma_e\right)\right\} C_P^{t,m} +$$

$$(1-w)\left(-\dot{m}_{sS} - \Gamma_s\right) C_S^{t,m} + (1-w)\left(-\dot{m}_{nN} - \Gamma_n\right) C_N^{t,m} + (1-w)\left(-\Gamma_e\right) C_E^{t,m} +$$

$$(1-w) C_W^{t,m} + \gamma(1-w)\left[-\dot{m}_{sP}\right]\left[\frac{\partial C_P}{\partial r}\left(r_{\bar{s}} - r_P\right) + \frac{\partial C_P}{\partial z}\left(z_{\bar{s}} - z_P\right)\right]^{t,m} \beta_{sP}^{\,t,m} +$$

$$\gamma(1-w)\left[-\dot{m}_{sS}\right]\left[\frac{\partial C_S}{\partial r}\left(r_{\bar{s}} - r_P\right) + \frac{\partial C_S}{\partial z}\left(z_{\bar{s}} - z_P\right)\right]^{t,m} \beta_{sS}^{\,t,m} +$$

$$\gamma(1-w)\left[-\dot{m}_{nP}\right]\left[\frac{\partial C_P}{\partial r}\left(r_{\bar{n}} - r_P\right) + \frac{\partial C_P}{\partial z}\left(z_{\bar{n}} - z_P\right)\right]^{t,m} \beta_{nP}^{\,t,m} +$$

$$\gamma(1-w)\left[-\dot{m}_{nN}\right]\left[\frac{\partial C_N}{\partial r}\left(r_{\bar{n}} - r_P\right) + \frac{\partial C_N}{\partial z}\left(z_{\bar{n}} - z_P\right)\right]^{t,m} \beta_{nN}^{\,t,m} +$$

$$\gamma(w)\left[-\dot{m}_{sP}\right]\left[\frac{\partial C_P}{\partial r}\left(r_{\bar{s}} - r_P\right) + \frac{\partial C_P}{\partial z}\left(z_{\bar{s}} - z_P\right)\right]^{t+\Delta t,m} \beta_{sP}^{\,t+\Delta t,m} +$$

$$\gamma(w)\left[-\dot{m}_{sS}\right]\left[\frac{\partial C_S}{\partial r}\left(r_{\bar{s}} - r_P\right) + \frac{\partial C_S}{\partial z}\left(z_{\bar{s}} - z_P\right)\right]^{t+\Delta t,m} \beta_{sS}^{\,t+\Delta t,m} +$$

$$\gamma(w)\left[-\dot{m}_{nP}\right]\left[\frac{\partial C_P}{\partial r}\left(r_{\bar{n}} - r_P\right) + \frac{\partial C_P}{\partial z}\left(z_{\bar{n}} - z_P\right)\right]^{t+\Delta t,m} \beta_{nP}^{\,t+\Delta t,m} +$$

$$\gamma(w)\left[-\dot{m}_{nN}\right]\left[\frac{\partial C_N}{\partial r}\left(r_{\bar{n}} - r_P\right) + \frac{\partial C_N}{\partial z}\left(z_{\bar{n}} - z_P\right)\right]^{t+\Delta t,m} \beta_{nN}^{\,t+\Delta t,m} \tag{A.20}$$

A.5 Boundary Conditions and Implementation Details

This section contains additional information regarding the boundary conditions discussed in Section 3.3. The boundary condition at the injection chamber can be either a Type 1 or Type 3 given by,

$$C(r,z,t) = \hat{C}(r,z,t), \text{ or} \qquad \text{Dirichlet (Type 1)} \qquad \text{(A.21)}$$

$$\hat{qC} = q_r C - \theta D_{rr} \frac{\partial C}{\partial r} \qquad \text{Robin (Type 3)} \qquad \text{(A.22)}$$

where $\hat{C}$ is a prescribed concentration (M/L^3), and $\hat{qC}$ represents a specified mass flux (M/L/T). Along the extraction chamber a Type 4 boundary condition (Frind, 1988) is assigned and one of two approaches is used depending on the advective scheme. When either a CDS or UDS is specified, linear interpolation between the C_N and C_P nodal values is used to estimate the facial concentration,

$$C_s = C_P\left(1 - \frac{l_{sP}}{l_{PN}}\right) + C_N\left(\frac{l_{sP}}{l_{PN}}\right) \qquad \text{(Type 4)} \qquad \text{(A.23)}$$

When SOU with LDC is specified, the extraction chambers facial concentration is estimated using Eq. (A.12), after the gradients have been reconstructed. Finally, the CVs along the wellbore and the external no-flow boundaries of the distal streamline are assigned a Type 2 bounary condition given by,

$$\frac{\partial C}{\partial \hat{n}} = 0 \qquad \text{Neumann (Type 2)} \qquad \text{(A.24)}$$

A.6 Mass Balance Calculations

The cumulative mass balance error was estimated using,

$$MBE = \frac{\left(Total\ \ Mass_{IN} - Total\ \ Mass_{OUT} - Mass_{AQUEOUS} - Mass_{SOLID} - Mass_{DECAYED}\right)}{Total\ \ Mass_{IN}} x100\%$$

(A.25)

where $Total\ Mass_{IN}$ represents the amount entering the system, $Total\ Mass_{OUT}$ represents the amount exiting the system, $Mass_{AQUEOUS}$ and $Mass_{SOLID}$ is mass in the aqueous and solid phases, respectively, and $Mass_{DECAYED}$ represents the amount of mass which has decayed.

APPENDIX B

File Requirements

To run this model you will require two input files:

1) "*file names.nam*" an input file that handles all the input and output file names
2) a user named file containing all the input data and control options available in the model.

FILE NAME FILE

Sample file structure…

```
#unit 11 - data in
"Sample_Input_1.inp"
# unit 12 - echo data in
"debug.dat"
#unit 14 - streamfunction and flux field from zl
"stfn and flux field zl.dat"
#unit 15 - streamfunction field from numerical solution
"stfn field num.dat"
#unit 16 - streamfunction and flux field from numerical solution
"stfn and flux field num.dat"
#unit 17 - pathlines from Z&L
"pathlines zl.dat"
# unit 18 - numerical pathlines
"pathlines num.dat"
# unit 19 - arrival time data
"arrival_time.dat"
# unit 20 - btc profiles
"advbtc.dat"
# unit 21 - streamline oriented mesh
"som.dat"
# unit 22 - som volume data
"som volume.dat"
# unit 23 - mass balance from transport code for conservative
tracer
"mass balance_cons.dat"
# unit 24 - btc profiles from transport code for conservative
tracer
"btc_trans_cons.dat"
# unit 25 - spatial concentrations fields for tecplot input for
conservative tracer
"conc_rz_cons.dat"
# unit 26 - injection chamber flow/streamfunction profiles
"inj_chamber flow.dat"
# unit 27 - extraction chamber flow/streamfunction profiles
"ext_chamber flow.dat"
# unit 28 - decay mass
"decay mass.dat"
# unit 29 - mass balance from transport code for sorbing tracer
```

```
"mass balance_sorb.dat"
# unit 30 - btc profiles from transport code for sorbing tracer
"btc_trans_sorb.dat"
# unit 31 - spatial concentrations fields for tecplot input for
sorbing tracer
"conc_rz_sorb.dat"
# unit 32 - mass balance from transport code for decaying tracer
"mass balance_dec.dat"
# unit 33 - btc profiles from transport code for decaying tracer
"btc_trans_dec.dat"
# unit 34 - spatial concentrations fields for tecplot input for
decaying tracer
"conc_rz_dec.dat"
# unit 35 - mass balance from transport code for electron
acceptor
"mass balance_ea.dat"
# unit 36 - btc profiles from transport code for electron
acceptor
"btc_trans_ea.dat"
# unit 37 - spatial concentrations fields for tecplot input for
electron acceptor
"conc_rz_ea.dat"
# unit 38 - mass balance from transport code for substrate
"mass balance_sub.dat"
# unit 39 - btc profiles from transport code for substrate
"btc_trans_sub.dat"
# unit 40 - spatial concentrations fields for tecplot input for
substrate
"conc_rz_sub.dat"
# unit 41 - btc profiles from transport code for the first
aqueous species of the input file
"btc_trans_aq.dat"
# unit 42 - spatial concentrations fields for tecplot input for
the first aqueous species of the input file
"conc_rz_aq.dat"
# unit 43 - mass balance from transport code for the first
aqueous species of the input file
"mass balance_aq.dat"
# unit 44 - mass balance % for conservative tracer
"m_b_cons.dat"
# unit 45 - mass balance % for sorbing tracer
"m_b_sorb.dat"
# unit 46 - mass balance % for decaying tracer
"m_b_dec.dat"
# unit 47 - mass balance % for electron acceptor
"m_b_ea.dat"
# unit 48 - mass balance % for substrate
"m_b_su.dat"
# unit 49 - Concn Bndry Exceedance
"CBE.dat"
```

```
# unit 50 - SOM Data
"som data.dat"
# unit 51 - Microbial Concn @ Last time step
"concn_rz_mic.dat"
```

INPUT DATA FILE

LINE 1: - Control Flags

imeth – Method for solving the problem (=1 z&l; =2 numerical; =3 z&l and numerical)

istfn – Do you wish to calculate the streamfuction field or read it from the output from a previous run? (=1 calculate; =-1 read from "output" file)

ihead – Do you wish to calculated the hydraulic head field? (=1 calculate; =2 use well bore model to calculate; =3 use well bore model to calculate and use results to calculate the streamfunction field)

iflux – Do you wish to calculate the flux field? (=1 calculate flux field)

ipath – Do you wish to calculate the pathlines? (=1 calculate pathlines)

ibtc – Do you wish to calculate the advective breakthrough curves? (=1 calculate advective btc's)

isom – Do you wish to build the stream oriented mesh? (=1 build streamline oriented mesh)

itrans – Would you like to solve the transport equation? (=1 solve reactive solute transport equations). The following files are outputted if itrans=1:

for imode=1: "*mass balance_cons.dat*", "*conc_rz_cons.dat*", "*btc_trans_cons.dat*", "*som data.dat*", "*conc_err.dat*", and "*CBE.dat*"

for imode=2: "*mass balance_cons.dat*", "*conc_rz_cons.dat*", "*btc_trans_cons.dat*", "*mass balance_sorb.dat*", "*conc_rz_sorb.dat*","*btc_trans_sorb.dat*", "*mass balance_dec.dat*", "*conc_rz_dec.dat*", "*btc_trans_dec.dat"* , "*som data.dat*", and "*CBE.dat*"

for imode=3: "*mass balance_cons.dat*", "*conc_rz_cons.dat*", "*btc_trans_cons.dat*", "*mass balance_sorb.dat*", "*conc_rz_sorb.dat*","*btc_trans_sorb.dat*", "*mass balance_dec.dat*", "*conc_rz_dec.dat*", "*btc_trans_dec.dat*", "*mass balance_aq.dat*", "*conc_rz_aq.dat*", "*btc_trans_aq.dat*", "*som data.dat*", and "*CBE.dat*"

for imode=4: "*mass balance_cons.dat*", *"m_b_ea.dat", "m_b_su.dat", "m_b_micro.dat"*, "*conc_rz_cons.dat*", "*btc_trans_cons.dat*", "*mass balance_ea.dat*", "*conc_rz_ea.dat*","*btc_trans_ea.dat*", "*mass balance_sub.dat*", "*conc_rz_sub.dat*", "*btc_trans_sub.dat*", "*som data.dat*", and "*CBE.dat*"

Note: "*..._cons.dat*" is for a conservative tracer, "*..._sorb.dat*" is for a sorbing tracer, "*..._dec.dat*" is for a decaying tracer, "*..._aq.dat*" is for an aqueous species, "*..._ea.dat*" is for an electron acceptor and "*..._sub.dat*" is for an injected substrate.

OS – operative-splitting scheme (=0 no source/sink; =1 SI; =2 SNI; =3 SYMM_SI; =4 STRANG_SPLIT)
(SI = standard sequential iterative)
(SNI = sequential non-iterative)
(SYMM_SI = symmetric sequential iterative)
(STRANG_SPLIT = strang-splitting)

imode – mode for tracer injection
(=1 conservative tracer)
(=2 conservative, sorbing and decaying tracer)
(=3 conservative, sorbing, decaying tracer and aqueous/solid species interaction)
(=4 conservative tracer and biodegrading tracers controlled by monod kinetics)

LINE 2: - Output Control Flags

istfno - (=1 write streamfunction field to disk) If z&L is chosen in imeth then the output file is "*stfn field_zl.dat*". If numerical is chosen in imeth then the output file is "*stfn num.dat*". If both are chosen in imeth then "*stfn field zl.dat*" and "*stfn field num.dat*" are output.

ifluxo - (=1 write flux field to disk) If z&L is chosen in imeth, and iflux = 1 then the output file is "*stfn and flux field zl.dat*". If numerical is chosen in imeth, and iflux = 1 then the output file is "*stfn and flux field num.dat*". If both are chosen in imeth, and iflux = 1 then "*stfn and flux field zl.dat*" and "*stfn and flux field num.dat*" are output.

ipatho - (=1 write pathlines to disk) If z&L is chosen in imeth, and ipath = 1 then the output file is "*pathlines_zl.dat*". If numerical is chosen in imeth, and ipath = 1 then the output file is "*pathlines num.dat*". If both are chosen in imeth then "*pathlines_zl.dat*" and "*pathlines num.dat*" are outputted.

itimeo – Length of time between leaving injection chamber and arriving at the extraction chamber (=1 write arrival time to disk). If ipath = 1 and imeth ≠1, the output file is "*arrival_time.dat*"

ibtco - (=1 write btc profiles to disk) If ibtc=1, the output file is "*advbtc.dat*".

isomo - (=1 write streamline oriented mesh to disk) If isom=1, the output file is "*som.dat*".

iodetail - (=1 write iterative solution details to screen) Writes iterative metrics to the screen.

LINE 3: - Dipole Properties for a Symmetric Dipole

Note: *a consistent set of units must be used except where noted. We have adopted – length in meters, time in seconds, and mass in kg.*

rw – well radius (m)

length - distance between chambers centres (m)

delta - half chamber length (m)

flow - injection/extraction flow rate (m^3/s) (full system)

LINE 4: - Dipole Properties for Asymmetric Dipole

If you wish to choose an asymmetric dipole then **imeth=2**.

isymm – Would you like to make the dipole symmetric or asymmetric? (=1 symm; =2 asymmetric)

len_up - length from center of middle packer to center of upper chamber

delta_up - half chamber length of upper packer

len_low - length from center of middle packer to center of lower chamber

delta_low - half chamber length of lower packer

LINE 5: - Bulk Aquifer Properties

krr - radial hydraulic conductivity (m/s)

kzz - vertical hydarulic conductivity (m/s)

por – porosity (-)

nkzone - number of k field zones

LINE 6: - Layer or "Zone" Properties – if you wish to add properties for multiple layers, just include values and variables here (nkzone lines).

lk_top - distance to top of horizontal feature from $z = 0$ (m)

lk_bot - distance to bottom of horizontal feature from $z=0$ (-ve if below $z=0$) (m)

krr_zone - radial hydraulic conductivity of zone (m/s)

kzz_zone - vertical hydarulic conductivity of zone (m/s)

por_zone - porosity of zone

LINE 7: - Skin Properties

iskin - Account for well bore skin? (=0 no; =1 yes)

skin_thick - multiple of well radius

kr_skin - radial hydraulic conductivity of skin (m/s)

kz_skin - vertical hydraulic conductivity of skin (m/s)

por_skin - porosity of skin

LINE 8: - Grid Dimensions for z&l field

rmax - maximum radial dimension

nr_zl - number of mesh points in the r direction

zmax - maximum vertical dimension (actually use [-*zmax*,+*zmax*])

nz_zl - number of mesh points on the z direction

LINE 9: - CV Properties for the Numerical Field

nr – number of CV's in the r-direction

rfact – a factor used to increase delri

delri – size of 1st CV in r-direction

nz – number of CV's in the z-direction

zmesh – attributes of the mesh (=1 no horizontal boundary; =2 top horizontal boundary; =3 bottom horizontal boundary; =4 top and bottom horizontal boundary)

delzi – size of 1st CV in z-direction

zfact – a factor used to increase delzi

lentop – length to top boundary (used if zmesh = 2 or 4)

lenbot – length to bottom boundary (used if zmesh = 3 or 4)

LINE 10: - Fluid Properties

rhow - water (fluid) density (kg/m^3)

mnw - fluid viscosity (Pa-s)

grav - acceleration due to gravity (m/s^2)

LINE 11:

initial psi value - initial streamfunction value for numerical solution

isolve - numerical solution method (=1 point SOR; =2 LSOR; =3 GMRES; =4 CGSTAB)

ih_bdy – (=0 no-flow bdy along rhs; = 1 hydrostatic head bdy on rhs)

hvalue - datum head value if ih_bdy=0; or hydrostatic head value if ih_bdy=1

LINE 12: - Numerical Solution Control Parameters for SOR or LSOR

maxiter - maximum number of iterations for SOR or LSOR

w - sor weighting factor

itype +1 LSOR on r-lines only per sweep
+2 LSOR on z-lines only per sweep
-2 LSOR on z-lines only per sweep with r-line sweeps every 100 iterations
+3 LSOR on r-lines followed by z-lines per sweep

tol(1) - L1-norm convergence tolerance

tol(2) - maximum residual convergence tolerance

tol(3) - maximum difference convergance tolerance

LINE 13: - Numerical Solution Control Parameters for GMRES or CGSTAB

nitmax - maximum number of iterations for GMRES or CGSTAB

smaxtol - absolute maximum solution update

rmaxtol - L2-norm of residual vector

rtwotol - L2-norm of residual vector relative to initial residual vector

LINE 14: - Pathline Calculation Parameters

nstrm_tubes - number of streamtubes

frac_flow - % of injection chamber where streamtubes are distributed

deltmin - base timestep increment for particle tracking

tmax - used as a check to terminate particle tracking program

tol1 - used to check exiting streamlines

nskip_path - number of points to skip on streamlines for pathline plotting (note: travel time uses all points)

LINE 15: - Advective BTC

delt_btc - nominal time step to construct advective BTC (secs)

tsource - length of time source is on (hrs) (**Note:** This is converted to secs in the read file.)

tfinish - length of time to monitor extraction well effluent (days) (**Note:** This is converted to secs in the read file.)

nskip_btc - number of points to skip on streamlines for BTC construction (**Note:** this only skips data points stored)

LINE 16: - SOM Parameters

im_type – (= 1 for uniform distribution of stream lines; = 2 for exponential growth of pathline spacing)

psi_start - starting location

psi_end - finish location

num_psi_intervals - number of streamline intervals (for im_type=1)

psi_beta - streamline growth factor (for im_type=2)

nskip_mesh - number of points on the streamline to skip

mfactor - controls grid spacing

LINE 17: - Reactive Transport Solution Parameters

iadv_type – (=1 for mid-point weighting; = 2 for upstream weighting; =3 N/A, =4 N/A)

ic_bdy – (=1 for type 1 at injection chamber; =3 for type 3 at injection chamber)

iface_flux – (=0 use interpolated flux from streamfunction mesh; =1 force flux based on SOM)

itime_w – (=0 fully explicit; =1 fully implicit)

delto - initial time step size (sec)

deltmax - maximum time step size (sec)

tfact - time step multiplication factor

tmaxc - maximum simulation time for transport calculations (days)

icplot_out - frequency of spatial r-z concentration data for plotting (=-1 no plots except at t=0 and t=tmaxc)

LINE 18: - Solver Details for Transport

itsolve - solver for transport (=3 use GMRES; =4 use CGSTAB)

nitmax_c - maximum number of iterations for GMRES or CGSTAB for transport routine

smaxtol_c - absolute maximum solution update for transport routine

rmaxtol_c - L2-norm of residual vector for transport routine

rtwotol_c - L2-norm of residual vector relative to initial residual vector for transport routine

LINE 19: - Global Transport Parameters

rhob - bulk density (kg/m^3)

alpha_l - longitudinal dispersivity (m)

alpha_t - transverse dispersivity (m)

LINE 20:

add – number of aqueous species to be injected for aqueous/solid species interaction (only for imode=3)

iter_num - number of iterations for iterative OS schemes (OS=1 or OS=3)

LINE 21: - Conservative Tracer Properties

This is used for imodes=1, 2, 3, 4

aq_conc - concentration of the injected conservative tracer (kg/m^3)

diff_eff - effective diffusion coefficient (m^2/s)

ts_num - length of time conservative tracer source is on (sec)

kp - linear distribution coefficient (m^3/kg)

LINE 22: - Sorbing Tracer Properties

aq_conc – concentration of the injected sorbing tracer (kg/m^3)

diff_eff – see above

ts_num – length of time sorbing tracer source is on (sec)

kp – linear distribution coefficient (units are dependant on rev)

power_s – power for the equilibrium sorption equation

rev – kinematic model flag.
(=0 for a linear sorption isotherm, $Cs = kpCw$)
(=1 for a Freundlich sorption isotherm, $Cs = kpCw^{power\_s}$)
(=2 for a non-equilibrium sorption model, $\frac{\partial Cs}{\partial t} = \gamma(kpCw - Cs)$)

cs – amount of sorbed mass (kg/kg) - for rev=2

gam - first order constant (1/sec) - for rev=2

LINE 23: - First Order Decay Tracer Properties

aq_conc – concentration of the injected first order decay tracer (kg/m^3)

diff_eff – see above

ts_num – length of time decay tracer source is on (sec)

kp – linear distribution coefficient (m^3/kg)

xk - first-order decay rate constant (units dependant on reaction order)

power_d – reaction order

$$\left(\frac{\partial Cw}{\partial t} = xk * Cw^{power\_d}\right)$$

LINE 24: - Monod Electron Acceptor

This is used for imode=4.

aq_conc – concentration of the injected electron acceptor (kg/m^3)

diff_eff – see above

ts_num – length of time electron acceptor source is on (sec)

kp – see above

xb - mass ratio of oxygen to substrate consumed

ka - electron acceptor 1/2 utilization constant (kg/m^3)

kmax - max utilization rate for substrate (1/sec)

LINE 25: - Monod Substrate

aq_conc – concentration of the injected substrate (kg/m^3)

diff_eff – see above

ts_num – length of time monod substrate source is on (sec)

kp – see above

ksb - half-utilization constant of subtstrate (kg/m^3)

rsb – retardation factor of substrate

LINE 26: - Monod Microbes

mi_cell – total microbial concentration (kg/m^3)

rm – retardation factor of microbes (kg/m^3)

kb - 1st order decay rate of micobial population (1/sec)

yb - microbial yield per unit substrate consumed

cell_m – mass per cell (kg)

LINE 27: - Aqueous Species #1

aq_conc – concentration of injected aqueous species (kg/m^3)

diff_eff – see above

ts_num – length of time aqueous species source is on (sec)

kp – see above

LINE 28: - Aqueous/Solid Parameters for Species #1

xk_a - decay rate constant for aqueous species (units are dependent on reaction order)

alph - power for aqueous species for reaction order

bet - power for solid species for reaction order

xk_sol - decay rate constant for solid species (units are dependent on reaction order)

sol_conc – initial concentration of solid species (kg/kg)

****Notes regarding the addition of aqueous/solid species.**

1. If you wish to add another aqueous and solid species, then line 27 and line 28 must be repeated in the input file (i.e. you would have 2 lines of line 27 and 2 lines of line 28).

   In the code you would need to include:

a) Additional lines of code in the OS=1/OS=3 iterative loop for calculating the difference between concentration at the current iteration and concentration at the previous iteration. This will be used for checking convergence and is noted in the code.
b) Additional lines of code at the exit of the OS=1/OS=3 iterative loop to check convergence. This is noted in the code.

2. If you wish to include additional properties to the aqueous and solid species:
    a) You need to include these properties in the "**read_data.f90**" file and if necessary, in the "**stfn.f90**" file, which is the module.

3. If you wish to make changes to the aqueous/solid interaction equations, you must:
    a) alter the functions (found after the *runge_kutta* subroutine),
    b) alter the arrays **k1**, **k2**, **k3** and **k4** in the *runge_kutta* subroutine to correspond with your new function,
    c) alter the array **mass_sum_decay** in the *mass_balance* subroutine, to correspond with your new function.

APPENDIX C

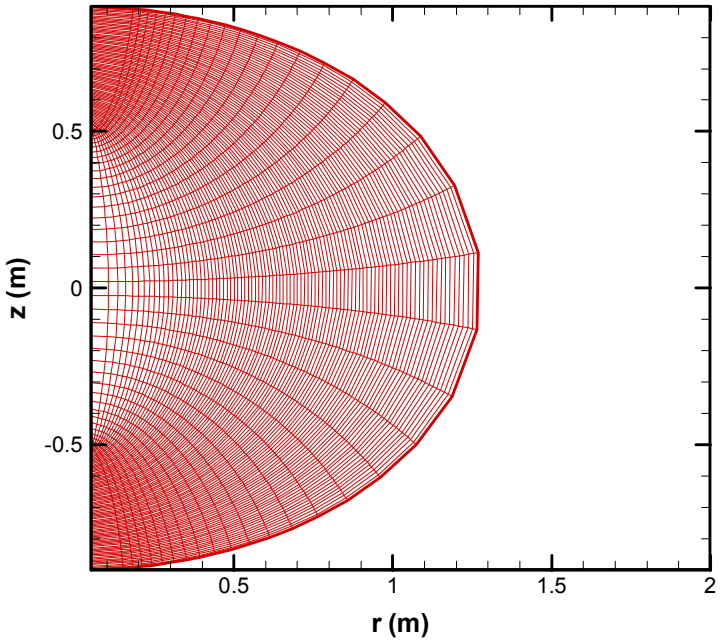

Figure C.1: SOM used for the CRTM vs. MODFLOW/MT3DMS.

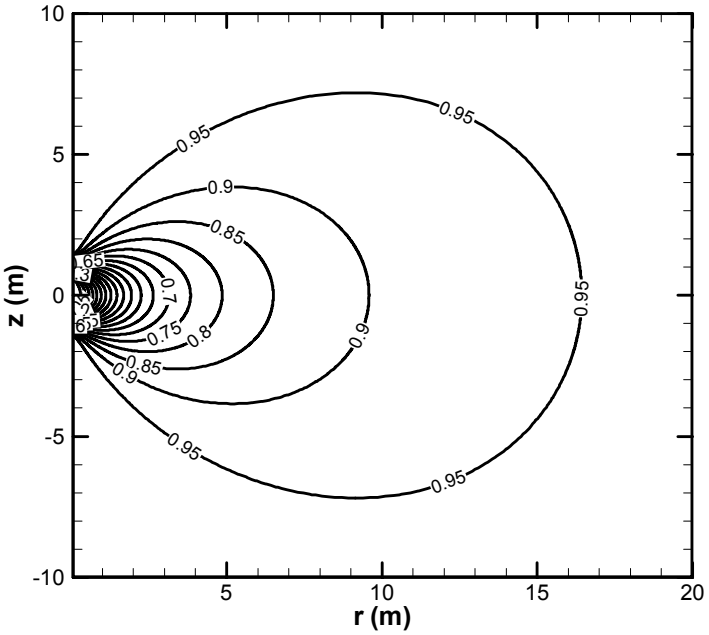

Figure C.2: Streamfunction field for CRTM.

APPENDIX D

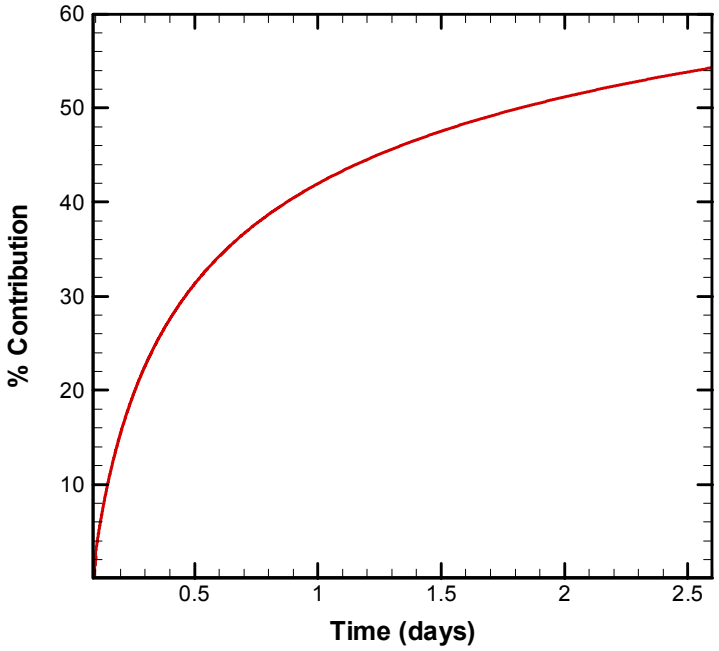

Figure D.1: Arrival time distribution for base case simulation.

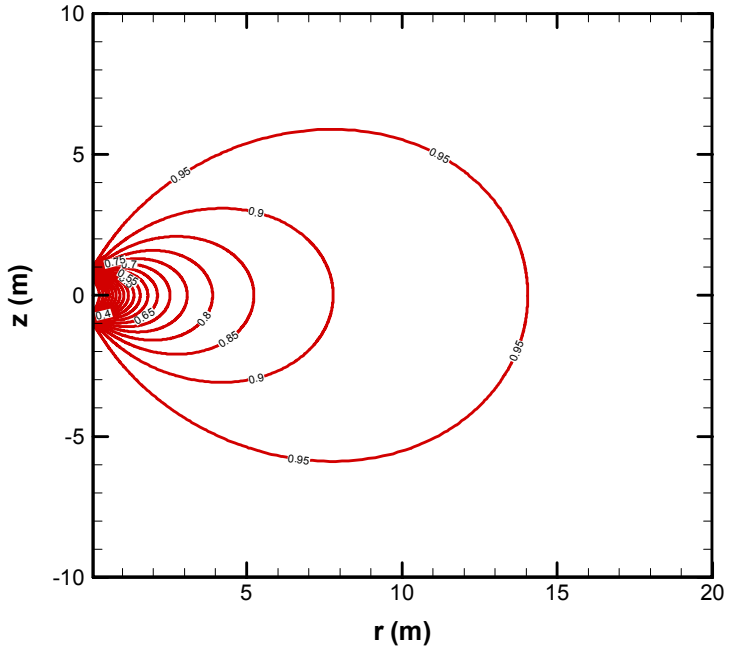

Figure D.2: Streamfunction fields for base case simulation.

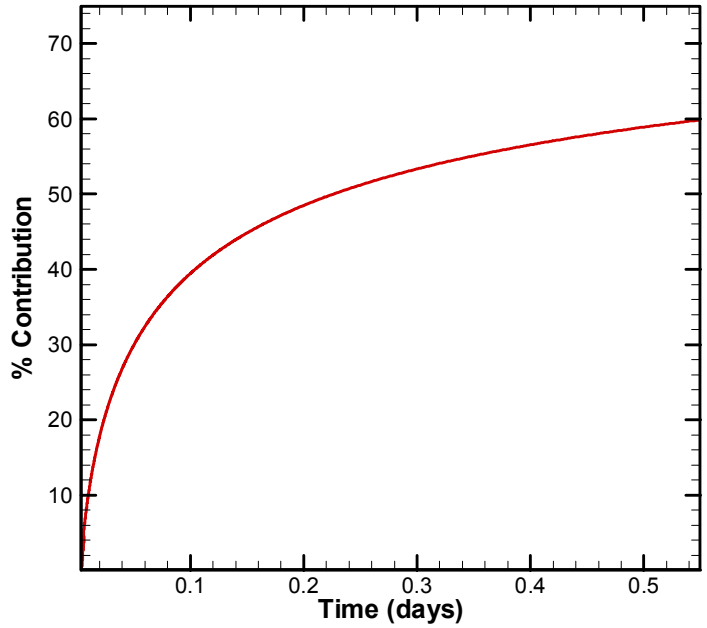

Figure D.3: Arrival time distribution for L = 0.4 m.

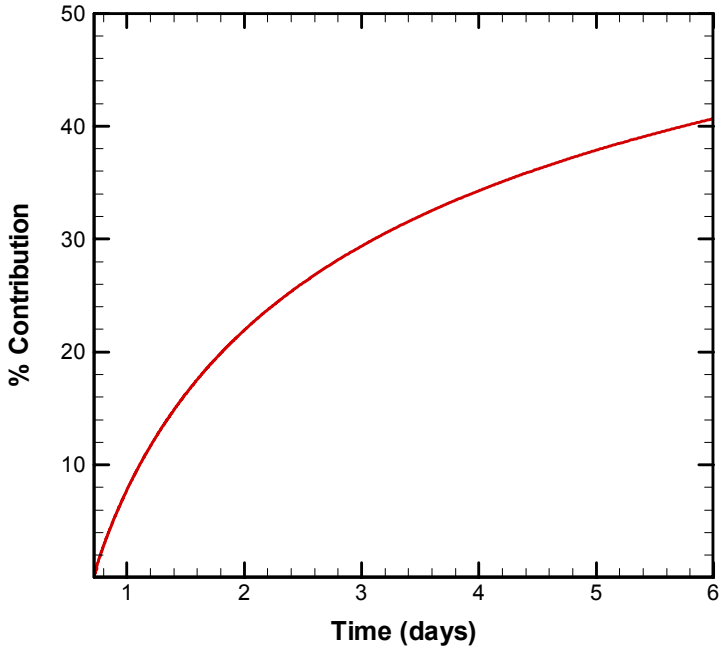

Figure D.4: Arrival time distribution for L = 1.5 m.

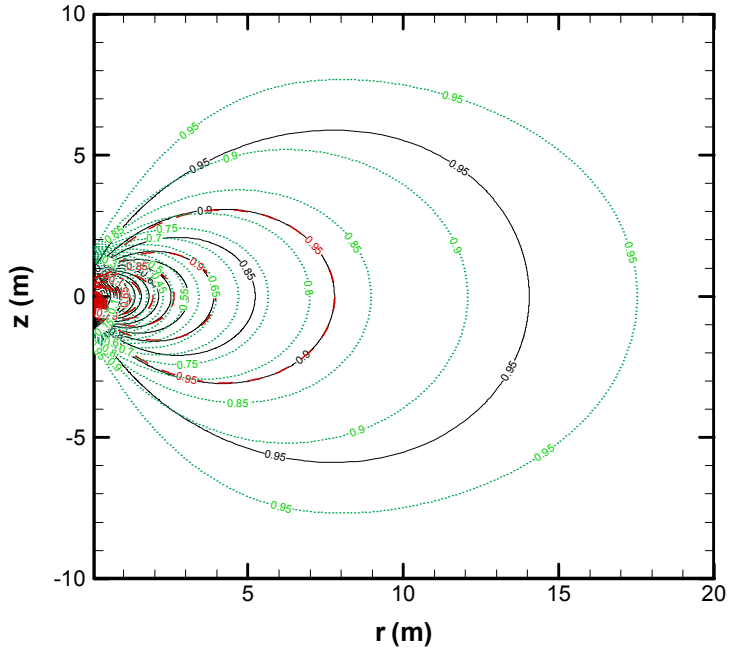

Figure D.5: Streamfunction fields for (a) L = 0.8 m (solid), (b) L = 1.5 m (dotted), and (c) L = 0.4 m (dashed).

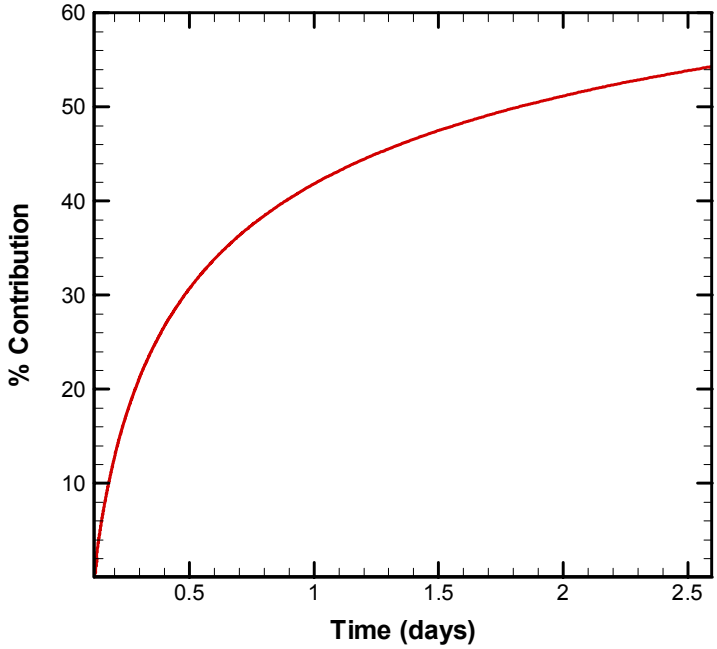

Figure D.6: Arrival time distribution for Δ = 0.15 m.

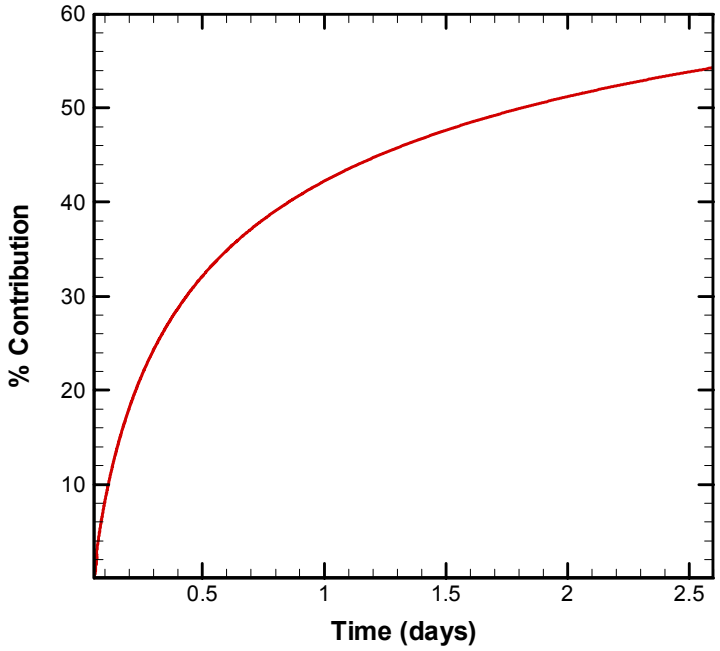

Figure D.7: Arrival time distribution for Δ = 0.45 m.

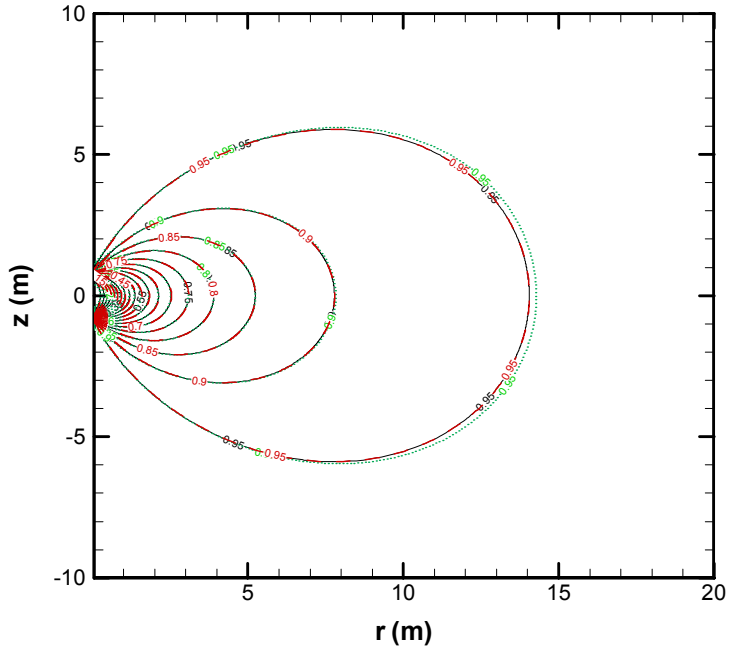

Figure D.8: Streamfunction fields for (a) Δ = 0.3 m (solid), (b) Δ = 0.15 m (dotted), and (c) Δ = 0.45 m (dashed).

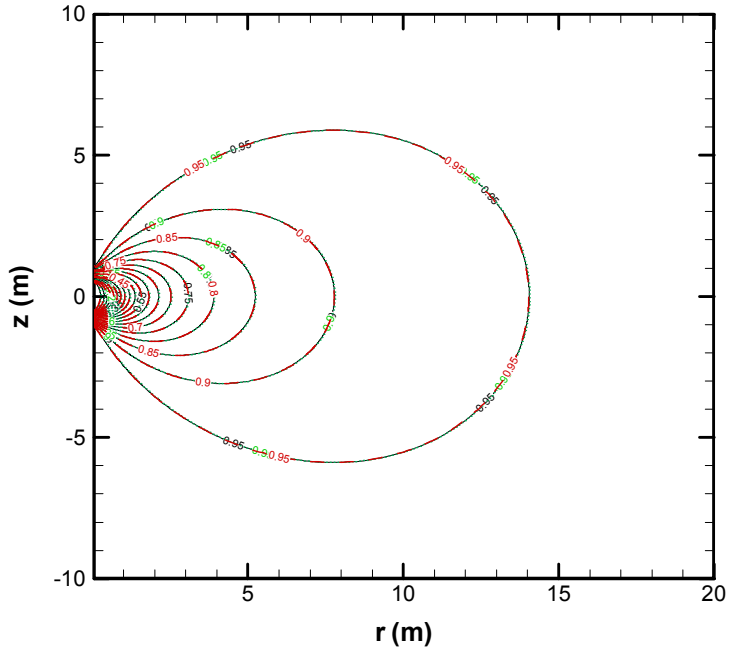

Figure D.9: Streamfunction fields for (a) r_w = 0.05 m (solid), (b) r_w = 0.025 m (dotted), and (c) r_w = 0.075 m (dashed).

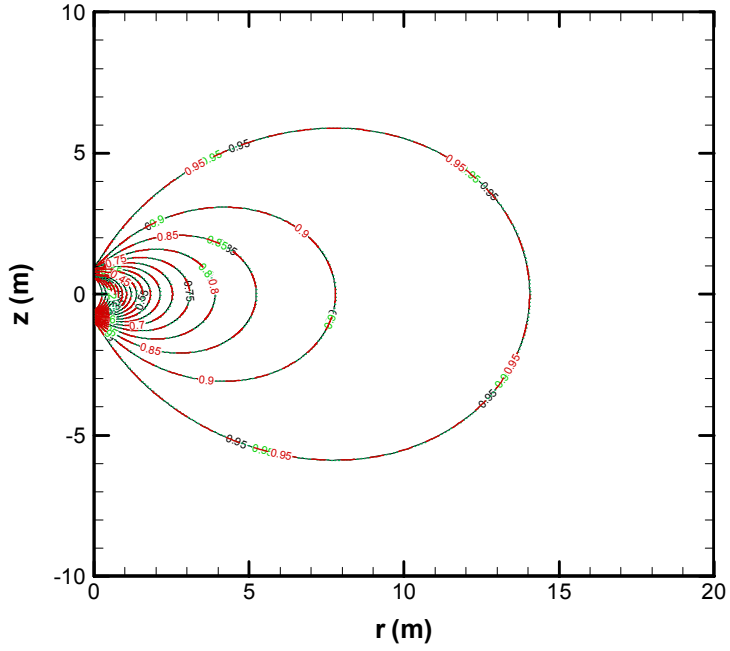

Figure D.10: Streamfunction fields for (a) Q = 1x10^{-3} m^3/s (solid), (b) Q = 1x10^{-5} m^3/s (dotted), and (c) Q = 1x10^{-4} m^3/s (dashed).

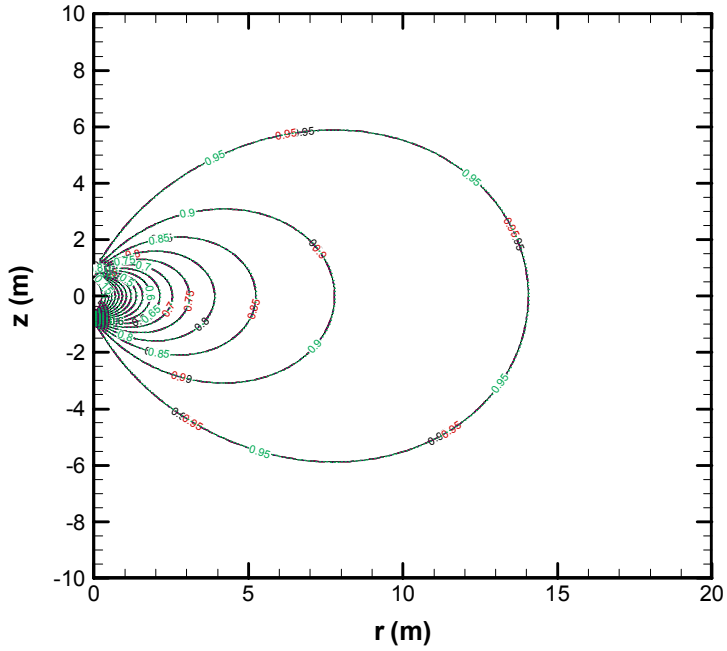

Figure D.11: Streamfunction fields for (a) injection length = 2 hr (solid), (b) injection length = 1 hr (dotted), (c) injection length = 6 hr (dashed-dot), and (d) injection length = 24 hr.